

**MODELLING AND COMPUTER SIMULATION
STUDIES OF SUGAR BASED AMPHIPHILIC SYSTEMS**

SARA AHMADI

**THESIS SUBMITTED IN FULFILMENT OF
THE REQUIREMENTS FOR THE DEGREE
OF DOCTOR OF PHILOSOPHY**

**DEPARTMENT OF CHEMISTRY
FACULTY OF SCIENCE
UNIVERSITY OF MALAYA
KUALA LUMPUR**

2014

UNIVERSITI MALAYA

ORIGINAL LITERARY WORK DECLARATION

Nama of Candidate: **SARA AHMADI** (I.C /Passport No: **P95425693**)

Registration/Matrik No: **SHC090053**

Nama Ijazah: **DOCTOR OF PHILOSOPHY**

Title of Project Paper/Research Report/Dissertation/Thesis (“this Work”):

Modelling and Computer Simulation studies of Sugar Based Amphiphilic Systems

Field of Study:

I do solemnly and sincerely declare that:

1. I am the sole author/writer of this Work;
2. This Work is original;
3. Any use of any work in which copyright exists was done by way of fair dealing and for permitted purposes and any excerpt or extract from, or reference to or reproduction of any copyright work has been disclosed expressly and sufficiently and the title of the Work and its authorship have been acknowledged in this Work;
4. I do not have any actual knowledge nor do I ought reasonably to know that the making of this work constitutes an infringement of any copyright work;
5. I hereby assign all and every rights in the copyright to this Work to the University of Malaya (UM), who henceforth shall be owner of the copyright in this Work and that any reproduction or use in any form or by any means whatsoever is prohibited without the written consent of UM having been first had and obtained;
6. I am fully aware that if in the course of making this Work I have infringed any copyright whether intentionally or otherwise, I may be subject to legal action or any other action as may be determined by UM.

Candidate’s Signature

Date

Subscribed and solemnly declared before,

Witness’s Signature

Date

Name: **RAUZAH HASHIM**

Designation: **PROFESSOR**

ABSTRACT

Nowadays, sugar-based amphiphiles are among the most attractive class of compounds to be studied both fundamentally and application-wise. They are one of the main components in cell membranes and play important role in many biological functions. Therefore, understanding the nature of the different liquid crystal phases of these materials is important and conceivable using different experimental techniques, theory and simulation. This thesis focuses on the last two methods to investigate the properties of these highly interesting soft materials.

We begin by examining a set of novel glycolipids which has been modified to include crown ethers attached to the sugar ring which increases the size of the hydrophilic area and causes to have higher packing parameters. Higher packing parameters induced formation of nonlamellar phases and prevent formation of lamellar phases. A theoretical study of a series of five glucose based glycolipid crown ethers and their complexes with Na^+ and K^+ was performed using the density functional theory with B3LYP/6-31G*. Optimized geometrical structures of the glycolipid crown ethers with cations were obtained and their corresponding electronic properties were calculated. In general, it was found that the oxygen atoms pairs O2 and O3 (or O4 and O6) on the sugar ring are constrained from moving toward the cation, which results in a weaker O-cation coordination strength for the oxygen pair compared to the other oxygen atoms in the crown ether ring. The thermodynamic properties of the binding of the complexes and the exchange

reaction in gas phase were evaluated. The cation selectivity pattern among the five molecules was in good agreement with the experiment.

Fully atomistic molecular dynamics simulation studies of thermotropic bilayers were performed using a set of glycosides namely n-octyl- β -D-glucopyranoside (β -C8Glc), n-octyl- α -D-glucopyranoside (α -C8Glc), n-octyl- β -D-galactopyranoside (β -C8Gal) and n-octyl- α -D-galactopyranoside (α -C8Gal) to investigate the stereochemical relationships of the epimeric/anomeric quartet linear glycolipids with the same octyl chain group. The results showed that, the anomeric stereochemistry or the axial/equatorial orientation of C1-O1 (α/β) is an important factor controlling the area and *d*-spacing of glycolipid bilayer systems in the thermotropic phase. The C4-epimeric (axial/equatorial) stereochemistry becomes dominant together with the anomeric one for the inter-molecular hydrogen bond. Thus, the trend in hydrogen bonding goes as β -C8Gal > α -C8Glc > β -C8Glc > α -C8Gal. The four bilayer systems showed anomalous diffusion behaviour with an observed trend for the diffusion coefficient exponent (α -C8Gal > β -C8Glc > α -C8Glc > β -C8Gal), and was in the reverse order to the hydrogen bonding interaction strength, but in compliance to the cis-trans effect of the C4-epimer and anomer.

We have also studied the lyotropic reverse hexagonal phase H_{II} from a glycolipid, namely using the Guerbet branched-chain (2'-n-octyl-n-dodecyl)- β -D-glucopyranoside (C₈C₁₂ β -D-Glc), at 14% and 22% water concentrations. In this simulation, it is necessary for us to use the united atom force field for carbohydrate from GROMOS because this approach will overcome the ambiguity of two optical

stereoisomers arising from the chiral center at the Guerbet branched chain. Moreover, this force field will enable us to run a longer simulation. Our simulations showed that at low water concentration (14%) the sugar head group overlapped extensively and protruded into the water channel. In contrast, in the 22% concentration system, a water column free from the sugar head group was formed, as expected for the system close to the limit of maximum hydration. In both concentrations, we found anomalous water diffusion in the xy -plane, i.e. the two-dimensional space confined by the surface of the cylinder. On the other hand, in the z -axis, the water diffusion obeyed the Einstein relation for 22% system, while for the 14% system it was slightly anomalous. Generally, a higher probability of hydrogen bonding but a shorter lifetime was found for the system of 22% water compared to the system of 14% water.

ABSTRAK

Kini, amfifilik molekul yang berasaskan karbohidrat merupakan kumpulan sebatian yang paling menarik untuk dikaji secara asas dan aplikasi. Kumpulan ini merupakan komponen utama membran sel dan memainkan peranan yang penting dalam pelbagai fungsi biologi. Oleh itu, pemahaman tabii pelbagai fasa cecair hablur sangat penting dan boleh difahami menerusi pelbagai teknik eksperimen, teori dan simulasi. Tesis ini fokus kepada penggunaan kaedah teori dan simulasi bagi mengkaji bahan lembut yang amat menarik ini.

Kami bermula dengan mengkaji satu set glikolipid baru yang telah diubahsuai dengan memasukkan mahkota eter yang terikat kepada cincin gula, yang eningkatkan saiz kawasan hidrifilik dan menyebabkan parameter pembungkusan yang lebih tinggi. Parameter pembungkusan yang tinggi telah menyebabkan pembentukan fasa bukan lamellar dan menghalang pembentukan fasalamelar. Kajian teori untuk lima siri glukosa bersandarkan glikolipid eter mahkota dan kompleksnya dengan Na^+ dan K^+ telah dilakukan menggunakan teori ketumpatan fungsi dengan B3LYP/6-31G*. Struktur geometri optimum glikolipid eter mahkota dengan kation telah diperoleh dan sifat elektroniknya dihitung. Secara umum, didapati pasangan atom oksigen O2 dan O3 (atau O4 dan O6) pada gelang gula dikekang daripada bergerak ke arah kation mengakibatkan koordinasi O-kation lemah untuk pasangan tersebut berbanding dengan atom lain dalam gelang eter mahkota. Sifat termodinamik untuk ikatan kompleks dan pertukaran tindak-balas dalam fasa gas telah dinilai. Corak

pemilihan kation dikalangan lima molekul menyokong keputusan eksperimen dengan baik.

Dalam bahagian seterusnya, simulasi dinamik molekul atom sepenuhnya ke atas dwilapisan termotropik telah dilakukan menggunakan satu set sistem glikosida iaitu n-oktil- β -D-glukopiranosida (β -C8Glc), n-oktil- α -D-glukopiranosida (α -C8Glc), n-oktil- β -D-galakto-piranosida (β -C8Gal) dan n-oktil- α -D-galaktopiranosida (α -C8Gal) bagi mengkaji hubungan stereokimia empat epimerik/anomerik glikolipid dengan kumpulan rantai oktil yang sama. Keputusan menunjukkan stereokimia anomerik atau secara paksi / khatulistiwa pada C1-O1 (α/β) adalah faktor utama yang mengawal luas dan jarak-d sistem dwilapisan glikolipid dalam fasa termotropik. Sudut kecondongan kumpulan kepala dan sifat susunan rantaian juga dipengaruhi oleh kesan anomerik di mana darjah kecondongan adalah lebih kurang 25% lebih kecil untuk β -anomer (β -C8Glc/Gal) berbanding α -anomer (α -C8Glc/Gal) dan α -anomer didapati lebih kurang tersusun berbanding β -anomer. Justeru itu, susunan ikatan hidrogen adalah β -C8Gal> α -C8Glc> β -C8Glc> α -C8Gal. Keempat-empat sistem dwilapisan menunjukkan keganjilan sifat penyebaran dengan pekali eksponen penyebaran (α -C8Gal> β -C8Glc> α -C8Glc> β -C8Gal), adalah bertentangan dengan kekuatan interaksi ikatan hidrogen tetapi mematuhi kesan cis-trans epimer dan anomer C4.

Dengan menggunakan GROMOS medan daya dalam simulasi dinamik molekul atomistik untuk karbohidrat, kajian tentang fasa liotropik heksagonal songsang, H_{II} dari sistem glikolipid dilaksanakan. Sistem tersebut merupakan

rantainya cabang Guerbet β -D-glukosida pada 14% dan 22% kepekatan air. Simulasi kami menunjukkan bahawa pada kepekatan air yang rendah (14%), kumpulan kepala gula bertindih secara berlebihan dan menembusi ke dalam saluran air. Manakala, di dalam sistem berkepekatan 22%, satu kolom air bebas dari kumpulan kepala terbentuk seperti dijangkakan untuk sistem yang menghampiri takat maksima hidrasi. Pada kedua-dua kepekatan, kami mendapati keganjilan dalam satah xy untuk penyebaran air, contohnya ruang dua dimensi yang terhad kepada permukaan silinder. Selain daripada itu, di dalam paksi- z , penyebaran air mematuhi hubungan Einstein untuk sistem 22%, manakala untuk sistem 14% sedikit keganjilan berlaku. Secara umumnya, kebarangkalian ikatan hidrogen adalah tinggi tetapi jangka hayat yang rendah didapati bagi sistem 22% air berbanding 14% sistem air.

AKNOWLEDGMENTS

In the name of Him who taught the soul to think,
And kindled the heart's lamp with the light of soul

My first and foremost thankfulness goes to Almighty God who had helped me through the journey of ending this collection of work successfully. I lift up my request to Him dearest God to grant success and happiness to all people who are in the same path as me in seeking infinite knowledge. I humbly seek the mercy and goodness of My Lord to help me and guide me in such a manner that I do not use the knowledge which I had acquired in a haughty, captivity circle nor as a tool for business or obtaining wealth with greed but rather use it all as a step to praise God and exalt my life and others known and unknown to me. I am contented that all my attempts to complete this work have ended in good results. My appreciation and gratitude goes to each and everyone who have contributed to the realization of the research.

My first and warmest thanks go to my supervisor, **Professor Dr. Raubah Hashim**, (the head of the fundamental science in self-assembly group), for introducing me to a very interesting research field, giving me the opportunity of working in her group. I really appreciate her support and ready availability on all matters. Her kindness has encouraged me to overcome the difficulties not only in scientific work but also in social life.

I would like to thank the financial supports provided by the University of Malaya, Faculty of Science and the Department of Chemistry. I also appreciate the research assistantship under the High Impact Research (HIR) from the University of Malaya and the Ministry of the Higher education (MOHE), UM.C/625 /HIR/MOHE/05.

I am also grateful to all my lab mates, especially Mr. Vijayan Manickam Achari and Mr. Hock Seng Nguan for sharing knowledge, ideas and helpful discussions and Miss Noor Idayu Zahid, Nuraini Ahmad, Zahra Moosapour and Seyed Mohammad Mirzadeh Hosseini for providing a friendly environment in which to work and study.

This thesis I want to dedicate to my dearest mother **Zahra**. It is through her kindness, hope and prayer together with the immense energy of her presence in my life all throughout that had been the pillar of support and strength for me to face all challenges in a very challenging world. All knowledge I had acquired came about with ease because of her overflowing love, care and concern. It all does not end here. I will be forever dependant on her and the key to paradise can only be obtained with her satisfaction. Thank you mother.

To my brothers **Mostafa, Peyman** and **Saber**, thank you. We grew, played, ate and learned together. We taught each other and shared all the knowledge and looked forward to greater knowledge which will lead us to be successful. Love all

of you very much and your love has filled my heart. Wishing all of you best wishes and happiness.

TABLE OF CONTENTS

ABSTRACT	iii
ABSTRAK	vi
ACKNOWLEDGMENT	ix
TABLE OF CONTANTS	xii
LIST OF FIGURES	xvi
LIST OF TABLES	xx
LIST OF SYMBOLS AND ABBREVIATIONS	xxii
1 INTRODUCTION	1
1.1 Introduction	2
1.2 Liquid crystals	4
1.3 Amphiphilic molecules and membrane systems	10
1.4 Crown ether compounds	14
1.5 Molecular Dynamics Simulation	16
1.5.1 Force field development for carbohydrates	20
1.5.2 System size and periodic boundary condition	22
1.5.3 Ensembles and time averages from the MD simulations	23
1.5.4 Long-range interactions	25
1.6 Schrodinger equation	26
1.6.1 Born-Oppenheimer approximation	28
1.6.2 Hartree-Fock approximation	29
1.6.3 Density functional theory	31
	xii

1.6.4	Molecular orbital theory	32
1.6.5	The basis set approximation	33
1.7	Objectives and outline of the chapters in this thesis	37
2:	LITERATUR REVIEW ON CROWN ETHER, BILAYER AND REVERSE HEXAGONAL SYSTEMS	40
2.1	Literature review of quantum study on crown ether system	41
2.2	Literature review of simulation studies on micellar, bilayer and hexagonal systems	43
3	RESEARCH METHODOLOGY	50
3.1	System description and quantum calculations of sugar-based glycolipids with the crown ether	51
3.2	Calculated parameters	55
3.2.1	Electronic chemical potential and electronegativity: Bridging computational and conceptual DFT	55
3.2.2	HOMO and LUMO	57
3.2.3	Fukui Function	58
3.3	System description and molecular dynamics simulation details of thermotropic bilayer phase	61
3.4	System description and molecular dynamics simulation details of the reverse hexagonal phase	65
3.5	Calculated parameters	68
3.5.1	Lipid tail and order parameter	68
3.5.2	Area at the interface per sugar head	68
3.5.3	Lipid tail and order parameter	69

3.5.4	Hydrogen bonding interaction	70
3.5.5	Tilt angle and head group orientation	71
3.5.6	Lipid Dynamics in Anhydrous Bilayer	73
4	RESULT AND DISCUSSION: DFT STUDY OF GLUCOSE BASED GLYCOLIPID CROWN ETHERS AND THEIR COMPLEXES WITH ALKALI METAL CATIONS Na⁺ AND K⁺	74
4.1	Structure of glycolipid crown ethers and their nucleophilicity	75
4.2	Geometrical structure of the complexes	78
4.3	Binding and exchange enthalpies and Gibbs free energies	85
5	RESULT AND DISCUSSION: ATOMISTIC SIMULATION STUDIES OF THE GLUCOSIDE AND GALACTOSIDE IN ANHYDROUS BILAYERS: EFFECT OF THE ANOMERIC AND EPIMERIC CONFIGURATIONS	89
5.1	Local density profiles (LDPs)	90
5.2	Area at the interface per sugar head	92
5.3	Hydrogen bonds analysis	92
5.4	Head group orientation	98
5.5	Order parameter	99
5.6	Lipid Dynamics in Anhydrous Bilayer	101
6	RESULT AND DISCUSSION: MOLECULAR DYNAMICS SIMULATIONS OF THE LYOTROPIC REVERSE HEXAGONAL H_{II} OF GUERBET BRANCHED-CHAIN β-D-GLUCOSIDE	105
6.1	Structure of the reverse hexagonal H _{II}	106
6.2	Diffusion of water molecules in the water channel of H _{II}	108

6.3	Interaction between water and sugar head group at different water concentrations	115
6.4	The packing of the alkyl chains	119
7	CONCLUSION	121
	REFERENCES	128
	APPENDICES	140
	LIST OF SCIENTIFIC CONTRIBUTIONS	150

Figure	LIST OF FIGURES	page
Figure 1-1:	Chemical structure of cholesteryl benzoate (the first liquid crystal) (Cr 145 °C SA 178.5 °C Iso)	4
Figure 1-2:	Schematic model of smectic A (left) and nematic (right)	5
Figure 1-3:	Schematic model of micelle, bilayer, cubic and hexagonal phase respectively from left to right respectively, (adopted from: http://www.pnas.org/content/106/24/9815/F1.prl.aps.org/files/cover_image/lg89-20.jpg and, http://today.slac.stanford.edu/images/2006/ROW-101906.jpg) (Access to the internet page on 14/08/2013)	5
Figure 1-4:	The <i>p</i> value and the aggregate shape of lipids (addopted from: http://ars.els-cdn.com/content/image/1-s2.0-0079670009001026-gr15.jpg)	7
Figure 1-5:	Theoretical Phase diagram of the lyotropic liquid and liquid crystalline phases (addopted from: http://www.particlesciences.com/images/tb/lyotropic-liquid-crystalline-phases.jpg) (Access to the internet page on 14/08/2013)	7
Figure 1-6:	Chemical structure of a glycolipid	8
Figure 1-7:	Chemical structure of n-octyl β -D-glycoside (OG)	8
Figure 1-8:	Typical cell membrane (adopted from: http://upload.wikimedia.org.wikipedia/commons/e/ee/CellMembraneDrawing.jpg) (Access to the internet page on 14/08/2013)	9
Figure 1-9:	Tendency for spontaneous curvature of a lipid monolayer, due to an imbalance in the distribution of the lateral forces across the layer (Redrawn from [30])	11
Figure 1-10:	Topology of reverse H_{II} (left) and normal H_I (right) hexagonal phase(Adoppted from: http://www.biomedcentral.com/content/figures/1757-5036-2-3-3-1.jpg) (Access to the internet page on 14/08/2013)	12
Figure 1-11:	Swelling of normal H_I (up) and reverse H_{II} (down) hexagonal lattice with increasing water content [Redrawn from [13]]	12

LIST OF FIGURES

Figure 1-12:	Lattice parameter and <i>d</i> -spacing (redrawn from http://ars.els-cdn.com/content/image/1-s2.0-S0009308497000935-gr2.gif)	13
Figure 1-13:	Schematic drawing of the molecular structures of glycolipids	16
Figure 1-14:	Schematic representation of bond stretching, angle bending, torsional terms and non-bonded interactions (adapted from[55])	22
Figure 1-15:	Two dimensional periodic boundary conditions (addopted from: http://matdl.org/repository/eserv/matdl:857/web_wiki2fez2465.j)	23
Figure 3-1:	The optimized structures of the series of glycolipid crown ethers with the level of theory B3LYP/6-31G*	52
Figure 3-2:	The optimized structures of complexes M ⁺ /G15C5, M ⁺ / G18C5 and M ⁺ /G21C5 at the level of theory B3LYP/6-31 G* where M ⁺ represent the cations Na ⁺ and K ⁺	53
Figure 3-3:	The optimized structures of complexes M ⁺ /G16C5 and M ⁺ /G18C5 at the level of theory B3LYP/6-31G* when M ⁺ represents the cations Na ⁺ and K ⁺	54
Figure 3-4:	Schematic structure of n-octyl- β -D-glucoopyranoside (β -C ₈ Glc) in HyperChem	63
Figure 3-5	Schematic structure of bilayer system in thermotropic phase in packmole	63
Figure 3-6	Chemical structures for glycolipids, a) n-octyl- β -D galactopyranosid (β -C ₈ Gal), b) n-octyl- α -D-glucoopyranoside (α -C ₈ Glc), c) n-octyl- β -D-glucoopyranoside (β -C ₈ Glc) and d) n-octyl- α -D-galactopyranoside (α -C ₈ Gal)	64
Figure 3-7:	Full atomistic model of (2'n-octyl-n-dodecyl)- β -D- glucopyronoside (C ₈ C ₁₂ β -D-Glc), (b) United atom model of C ₈ C ₁₂ β -D-Glc	65

LIST OF FIGURES

Figure 3-8:	(a) Six columnar of $C_8C_{12}\beta$ -D-Glc arrange in a hexagonal lattice.(b) The initial configuration for MD simulation, where the yellow lines indicate the periodic boundary.	6
Figure 3-9:	Typical hydrogen bonding in water molecule	71
Figure 4-1:	The optimized structures of the series of glycolipids crown ethers with the level of theory B3LYP/6-31G*. The oxygen atoms on the crown ethers are labelled	76
Figure 4-2:	The optimized structures of complexes $M^+/G15C5$, $M^+/G18C5$ and $M^+/G21C5$ at the level of theory B3LYP/6-31 G* where M^+ represent the cations Na^+ and K^+	79
Figure 4-3:	The optimized structures of complexes $M^+/G16C5$ and $M^+/G18C5$ at the level of theory B3LYP/6-31G* when M^+ represents the cations Na^+ and K^+	80
Figure 5-1:	(A) Local density profiles: averages over block of 20 ns from 40 ns to 200 ns for (a) α - C_8 Gal, (b) β - C_8 Glc, (c) α - C_8 Glc and (d) β - C_8 Gal. The solid lines are for head group and the dotted lines are for alkyl chain. Each colored line in the legend shows the ldp of different 20 ns block averages spread over the 160 ns production stage	91
Figure 5-2:	Intra-molecular hydrogen bond distribution over different oxygen locations	98
Figure 5-3:	Distribution of angles between C9-O4 vector and bilayer normal in α - C_8 Gal (- -), β - C_8 Gal (5- ----), β - C_8 Glc(---) and α - C_8 Glc (■■■■) bilayers	99
Figure 5-4:	The average bond order parameters of C-H along the chain, $-\langle S_{CD} \rangle$, for β - C_8 Gal (*), β - C_8 Glc (\square), α - C_8 Gal (+), and α - C_8 Glc (\times), Connecting lines drawn only as a guide. The error in these values is less than 4%.	101

LIST OF FIGURES

Figure 5-5:	Logarithmic scale of diffusion in xy direction for 160 ns for α/β - C_8Gal and α/β - C_8Glc .	103
Figure 5-6:	Packing density and hydrogen bonding for α/β -anomeric pairs	104
Figure 6-1:	The Configurations of the H_{II} phase after 50 ns for $C_8C_{12}\beta$ -D-Glc system with (a) 14% water and (b) 22% water	106
Figure 6-2	The radial density profiles of water, sugar head group and alkyl chains for $C_8C_{12}\beta$ -D-Glc system of H_{II} with (a) 14% water and (b) 22% water.	107
Figure 6-3:	The mean square displacements of water versus time (a) in the xy plane and (b) in the z direction	110
Figure 6-4:	Designation of oxygen atoms on the sugar head for $C_8C_{12}\beta$ -D-Glc	115
Figure 6-5:	The radial distribution function (RDF) of water-oxygen around the six oxygen atoms for two systems (a) 14% and (b) 22% water concentrations	117
Figure 6-6:	The distribution of the average radial distance of the CH_3 over angles around the cylinder, where the straight vertical lines are at the angles 30° , 90° , 120° , 180° , 240° and 270°	120

Table	LIST OF TABLES	Page
Table 1-1:	Synonyms terminology in thermotropic and lyotropic mesophases	7
Table 1-2:	Terminology in thermotropic mesophases and Synonyms in lyotropic mesophases	24
Table 3-1:	Comparison between HOMO and LUMO orbitals	58
Table 4-1:	Fukui function values for a nucleophilic for the different crown ethers	77
Table 4-2	HOMO and LUMO energies ϵ_{HOMO} and ϵ_{LUMO} , energy gap $\Delta\epsilon_{\text{LUMO-HOMO}}$, ionization potential I , electron affinity A and nucleophilicity index N for the glycolipids crown ethers	78
Table 4-3:	Geometry parameters (GP) of different glycolipid crown ethers complexes with Na^+ or K^+	82
Table 4-4:	Dihedral angle O2-C-C-O3 for optimized structures of molecules G15C5, G18C6 and G21C7 and their complexes with cations Na^+ and K^+	84
Table 4-5:	Dihedral angle O4-C-C-C for optimized structures of molecules G16C5 and G19C6 and their complexes with cations Na^+ and K^+	84
Table 4-6:	The binding energies ΔE^{b} , binding enthalpies ΔH^{b} , and Gibbs free energies ΔG^{b} , in the gas phase for the complexes at 298K	86
Table 4-7:	Exchange enthalpies ΔH and Gibbs free energies ΔG for the cation exchange in the gas phase at 298	87
Table 5-1:	d -spacing for β -C8Gal in L_C phase, α -C8Gal and α/β -C8Glc in L_α phase and their average surface areas at the interface per lipid from 160 ns simulations and the corresponding X-ray experimental data	91

LIST OF TABLES

Table 5-2:	Total number of hydrogen bonds per sugar for α -C ₈ Glc, β -C ₈ Glc, α -C ₈ Gal and β -C ₈ Gal comprised of inter-molecular and intra-molecular hydrogen bonds	96
Table 5-3:	calculated clearing temperatures, using different compounds as a reference	97
Table 6-1:	The average lattice parameters and surface area per molecule obtained from the MD simulations and compared with those of experimental measurements and estimations.	106
Table 6-2:	The exponents α for the diffusion of water in the xy -plane and the z direction and the diffusion coefficient D in the z direction for the C ₈ C ₁₂ β -D-Glc system at 14% and 22% water	111
Table 6-3:	Average number of hydrogen bonds on different oxygen sites of the sugar head and their respective lifetime	116
Table 6-4:	The peak positions in the oxygen to oxygen RDF of water for the four oxygen atoms from the hydroxyl groups, namely O2, O3, O4 and O6. These are compared with those from the experimental measurements for RDF of oxygen to oxygen in the bulk water	119

LIST OF SYMBOLS AND ABBREVIATIONS

1-D	One-dimensional
2-D	Two-dimensional
3-D	Three-dimensional
A	Electron affinity
AG	Alkyl glycoside
APG	Alkyl polyglycoside
AMBER	Assisted model building and energy refinement
CHARMM	Chemistry at Harvard macromolecular mechanics
Col	Columnar
COM	Center of mass
Cr	Crystalline
C_v	Heat capacity
DFT	Density functional theory
e.g.	exempli gratia; for example
et al.	et alii (and others)
etc.	et cetera; and the others
f	Fukui function
G	Gibbs free energy
Gal	Galactoside
GL	Glycolipid

Glc	Glucose
GTO	Gaussian type orbital
HF	Hartree-Fock
H _I	Normal hexagonal phase
H _{II}	Reverse hexagonal phase
HOMO	Highest occupied molecular orbital
I	Isotropic phase
<i>I</i>	First ionization energy
I _I	Normal discontinuous cubic phase
I _{II}	Inverse discontinuous cubic phase
IR	Infrared
L ₁	Normal micellar solution
L ₂	Inverse micellar solution
L _C	Lamellar crystal
LC	Liquid crystal
LCAO	Linear combination of atomic orbital
LDP	Local density profile
LUMO	Lowest unoccupied molecular orbital
L _α	Fluid lamellar liquid crystal phase
L _β	Gel phase
L _{β'}	Tilted gel phase
MC	Monte Carlo
MD	Molecular dynamics

MM	Molecular mechanics
MO	Molecular orbital
MPn	Moller-Plesset perturbation
N	Nucleophilicity index
NMR	Nuclear magnetic resonance
OH	Hydroxyl group
PBC	Periodic boundary condition
PDB	Protein data bank
PME	Particle Mesh Ewald
ps	Picosecond
Q	Canonical ensemble
Q _I	Normal bicontinuous cubic phase
Q _{II}	Inverse bicontinuous cubic phase
S	Order parameter
S	Entropy
SANS	Small-Angle Neutron-ray Scattering
SAXS	Small-Angle X-ray Scattering
SmA	Smectic A phase
SmC	Smectic C phase
STO	Slater type orbital
T _c	Clearing temperature
T _m	Melting temperature
α	Alpha

β	Beta
λ	Wavelength
τ	Lifetime
ψ	Wave function
\hat{H}	Hamiltonian operator
∇^2	Laplacian operator
χ	Electronegativity
Ω	Microcanonical ensemble
Ξ	Grand canonical ensemble
Δ	Isothermal-isobaric ensemble
μ	Chemical potential

LIST OF APPENDICES

Appendix A.1	Prepin file for n-octyl- α -D-galactoside	140
Appendix A.2	Prepin file for n-octyl- α -D-glycoside	141
Appendix A.3	Prepin file for n-octyl- β -D- glycoside	142
Appendix A.4	Prepin file for n-octyl- β -D- galactoside	143
Appendix B	Sample coordinate file for n-octyl- β -D-galactoside	144
Appendix C	Sample topology file for n-octyl- β -D-galactoside	145

CHAPTER 1

INTRODUCTION

1.1 Introduction

Exhaustive description of the phases of soft matter is conceivable through the studies of molecular motion of liquid crystals using theory and simulation. In addition, the interest in the simulation of liquid crystal system such as the lyotropic phases is to investigate those physical properties of the self-assembly structure that are of prime importance to the macroscopic function such as for those of biological systems. For example, the idea of considering lipid membrane as a two dimensional fluid where the proteins diffuse around was suggested by S. Jonathan Singer and Garth Nicolson in 1972, to be that of a fluid-mosaic model of biological membrane. Nevertheless, this model has been used for a long time to illustrate a simple view of biological membrane. It has been clarified that, the lipid molecules not only play the role as solvent for protein, but also they have a remarkable significance for the function of living systems[1]. Thus, different experimental and computational methods have been used to investigate the self-assembly systems comprise of various lipid molecules in order to understand the changes from structure to properties[2]. Nuclear magnetic resonance (NMR), infrared (IR), fluorescence spectroscopy together with neutron scattering and X-ray are some of the experimental methods that enable one to investigate the biological macromolecules at the molecular level. However, sometimes models are required in order to explain the experimental results; in this sense, the computer modelling and simulation is a very useful and powerful tool. Computer modelling is one of the dominant and impressive techniques for comprehensive understanding of the dynamics and structure of the biological systems[3, 4]. Intrinsic rules like hydrogen bond controlling these systems can be interpreted by the simple computational methods. These methods treat as a bridge between theory and experiment and provide intricate structural information of the studied system. The reliability of the simulation depends on the accuracy of the input parameters such as force field; besides that, the validity of

the simulation results have to be checked and compared with the experimental results directly or indirectly-

Glycolipids (GLs) normally found at the exterior of a cell wall and they are responsible for cell recognition process[5-7]. From the chemical point of view GLs are regarded as amphiphiles because they have two parts: hydrophilic (sugar moiety with single or multiple monosaccharide units) and hydrophobic (tail contains single or branched hydrocarbon chains). The two parts of molecule with different affinity for interaction with polar molecules tend to self-assemble into different mesophases, especially in polar water, such as micelles, lamellar and vesicles depending on degree of concentration and temperature[8-10]. Additionally these molecules self-assemble into lamellar crystal L_c and lamellar liquid crystal L_α at higher temperatures in the non-hydrated environment[11]. Natural GLs are difficult to extract in large quantity and purity that makes the synthetic GLs to be highly sought after. These glycolipids have intriguing structural diversity that gives rise to complex behaviour. Even in the simplest monosaccharide i.e. a single sugar unit, the diverse possible stereochemical arrangements of the hydroxyl groups give rise to different types of sugars, like glucose, mannose and galactose. The last two are glucose epimers, where the hydroxyl group at the 2 and 4 carbon positions within the sugar ring is axially oriented for mannose and galactose respectively instead of equatorial as for the case of glucose. The precise effect of sugar stereochemistry is very much guesswork, but how this affect the macroscopic behaviour is very profound.

This chapter describes the elementary concept of liquid crystals, their classification into both thermotropic and lyotropic phases, and a special class of liquid crystal material involving glycolipids and their applications. Following, we introduce

the crown ether system and the underlying principles of quantum mechanics and also the concept of molecular dynamics simulation.

1.2 Liquid crystals

In 1850, Willhelm Heintz reported the strange optical behaviour of melting stearin from a solid to a cloudy liquid, first forming an opaque and then a clear liquid. Likewise, between 1854-1860, Rudolf Virchow, Ch. Freiherr von. Mettanheimer and Gabriel Gustave Valentin, reported the same optical behaviour of a solution of nerve fiber under polarized light. These unusual melting behaviours went largely unnoticed and were insignificant. However, in 1888, an Austrian botanist by the name Friedrich Reinitzer found the unusual behaviour in the melting point of cholesteryl benzoate, and consulted a German physicist, Otto Lehmann, who was able to explain the unique crystalline properties of this material under a polarizing microscope. Lehmann called these materials by various names such as “fliessender Kristalle” (flowing crystal) or “flussige Kristalle” (fluid or liquid crystal, LC), a state of matter existing between isotropic liquid and crystalline solid caused by thermal perturbation or composition. These phases have orientational order but no or reduced positional order, and are therefore highly viscose and fluid-like [12].

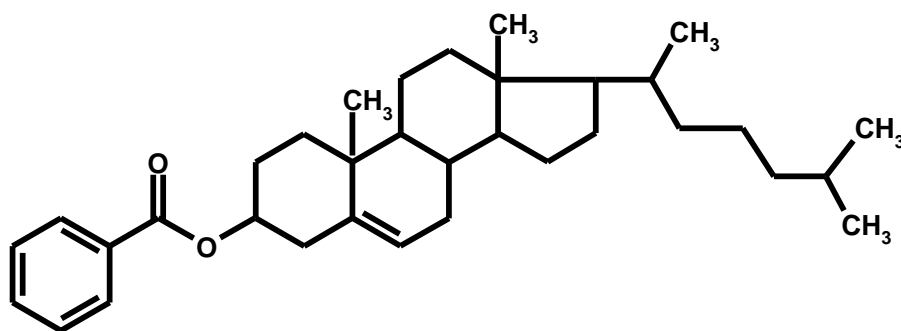


Figure1-1:Chemical structure of cholesteryl benzoate (the first liquid crystal) (Cr 145 °C S_A 178.5 °C Iso)

Mesogen refers to the molecule that forms a mesophase or liquid crystal. Strong anisotropy in the shape of the substance is a minimum requirement to form a mesophase. Most mesogens are calamitic (rod shape) or discotic (disc-like). Liquid crystals can be subdivided into two major categories according to the factor controlling the formation, namely temperature, which gives the thermotropic phases including the simple ones like nematic or smectic A. Another factor is composition, which gives the lyotropic phases such as micelles, bilayers, cubic and hexagonal phases. The ability of a liquid crystal compound to form both thermotropic and lyotropic mesophases is termed amphitropic[12] although some researchers use the term “amphotropic” [13]. Therefore, both thermal perturbation and composition of the compounds may become the driving forces for the formation of these liquid crystal phases.

Melting point, T_m and clearing point, T_c are two temperature markers, which define the range, within which the thermotropic liquid crystalline mesophase exists.

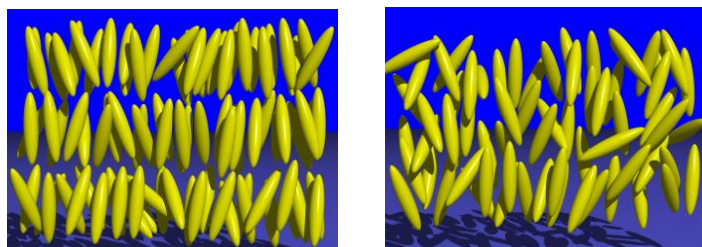


Figure 1-2: Schematic model of smectic A (left) and nematic (right)

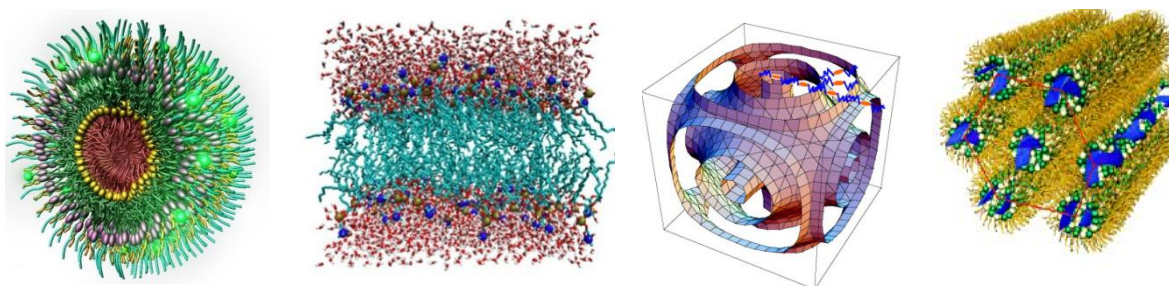


Figure 1-3: Schematic model of micelle, bilayer, cubic and hexagonal phase respectively from left to right respectively, (adopted from: http://www.pnas.org/content/106/24/9815/F1.prl.aps.org/files/cover_image/lg89-20.jpg and, <http://today.slac.stanford.edu/images/2006/ROW-101906.jpg>) (Access to the internet page on 14/08/2013)

T_m shows the lower temperature boundary, while T_c intends for the upper temperature limit of the liquid crystal phases. Within these two boundaries, there may be other phase transition temperatures, which imply polymorphism, or the ability to transform into different types of liquid crystal phases such as nematic and smectic.

Lyotropic liquid crystals are controlled by some factors such as concentration, temperature and polarity of the solvent. The term ‘lyo’ means solvent. Therefore, the solvent type and the concentration have a strong effect on a lyotropic liquid crystal. The type of mesophase formed is highly affected by the polarity of the solvent. For instance, a thermotropic cubic phase can change into a lamellar phase after the addition of a polar solvent at room temperature, but a hexagonal phase appears when a non-polar solvent is added at the same temperature[14]. Additionally, Sakya and Seddon[15] stated that the formation of the mesophases is remarkably controlled by the concentration of the solvent. For example, at room temperature a smectic A gives lamellar phase at 10% solvent, but at 30% solvent this transforms into a hexagonal phase. Shape is another controlling factor forming the type of liquid crystal phase. The packing theory, [16] expressed through a simple mathematical expression, can explain the shape factor. Equation (1.1) gives the dimensionless packing parameters, p :

$$p = \frac{v}{a_0 l_c} \quad (1.1)$$

where a_0 is the surface area of the head group at the interface, v is the hydrocarbon tail excluded volume, and l_c is the hydrocarbon tail chain length. Figure 1-4 shows the p value and the corresponding predicted aggregate shape [16], and Figure 1-5 shows the order of the lyotropic phases for the different compositions [17].

Table 1-1: Synonyms terminology in thermotropic and lyotropic mesophases

Terminology in thermotropic mesophases [18]	Synonyms in lyotropic mesophases [19, 20]
Smectic A,	Neat phase or lamellar phase, $L\alpha$
Col_{hd} , columnar phase	Hexagonal phase, middle phase, H_I , H_{II}
Bicontinuous cubic phase	Bicontinuous cubic phase, Q_I , Q_{II}
Discontinuous cubic phase	Discontinuous cubic phase, micellar cubic

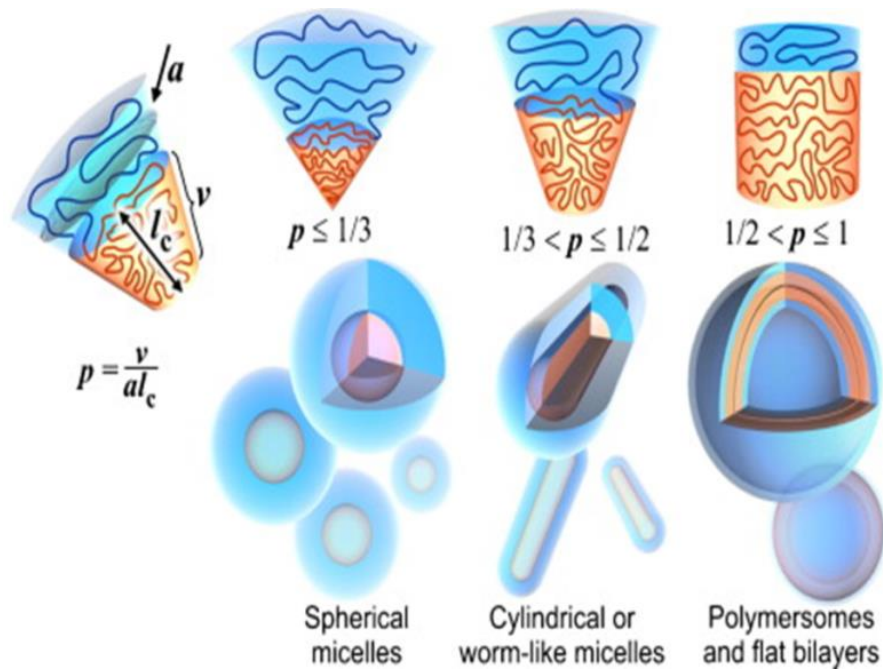


Figure 1-4: The p value and the aggregate shape of lipids (adopted from: <http://ars.els-cdn.com/content/image/1-s2.0-S0079670009001026-gr15.jpg>) (Access to the internet page on 14/08/2013)

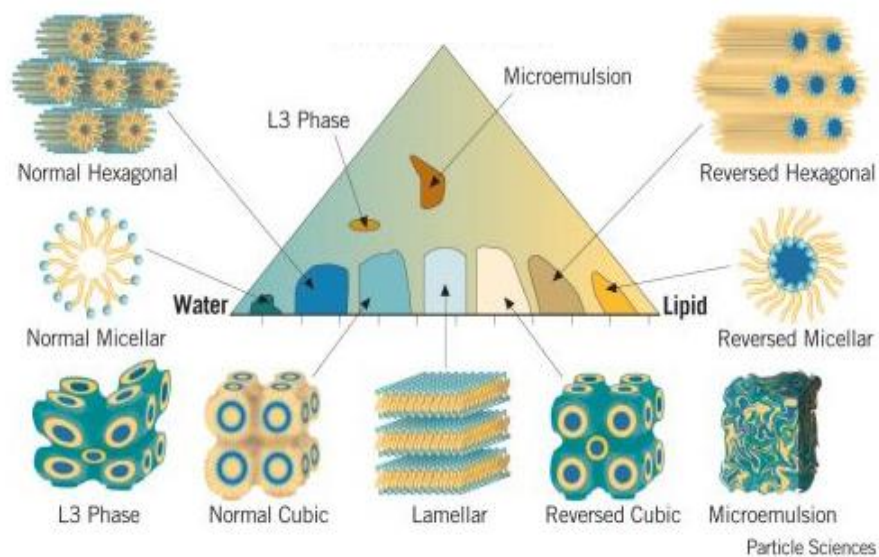


Figure 1-5: Theoretical Phase diagram of the lyotropic liquid and liquid crystalline phases (adopted from: <http://www.particleciences.com/images/tb/lyotropic-liquid-crystalline-phases.jpg>) (Access to the internet page on 14/08/2013)

Monophilic, amphiphilic and amphitropic molecules are three types of materials, which have the ability to form liquid crystals[2]. In this project we have chosen glycolipid molecules, which belong to the amphiphilic group.

Glycolipids such as glycoacylglycerolipids are nonionic organic compounds similar in structure to fats, but in which a short carbohydrate chain rather than a fatty acid is attached to the third carbon of the glycerol molecule (Figure 1-6) [30]; as a result, the molecule has hydrophilic "head" and a hydrophobic "tail."

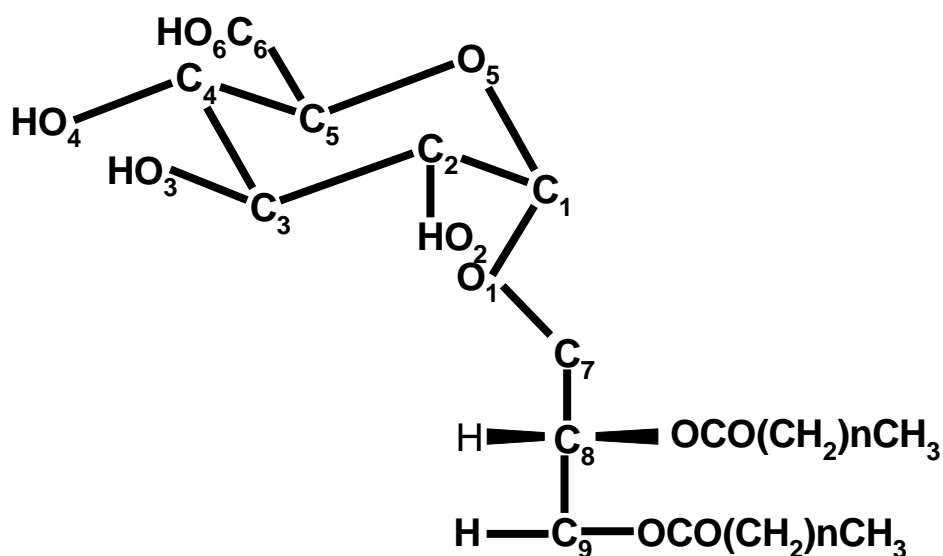


Figure 1-6: Chemical structure of a glycoacylglycerolipid[21]

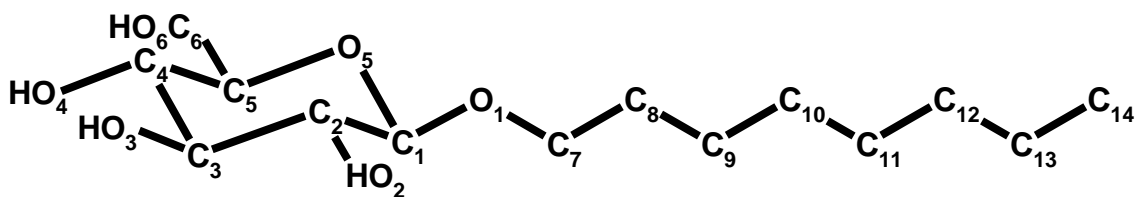


Figure 1-7: Chemical structure of n-octyl β -D-glycoside (OG)

Glycolipids are important constituents of the plasma membrane [21] and therefore, are attractive as vectors for liposomal drug delivery systems [22]. They can be extracted directly from natural sources such as palm oil and also synthesized from renewable resources such as fatty alcohols and oligosaccharides[22]. They play a major role in the isolation of membrane proteins without denaturation for physical

characterization[23] and are widespread over the surface membranes. Figure 1-8 shows a typical cell membrane and the presence of glycolipids within. Natural glycolipids are classified into three categories: glycosphingolipids (GSLs), glycoacylglycerolipids and glycosyl phosphopolyrenols. Monogalactosyl diacylglycerol (MGDG) and digalactosyl diacylglycerol (DGDG) are two examples of glycoacylglycerolipids[24].

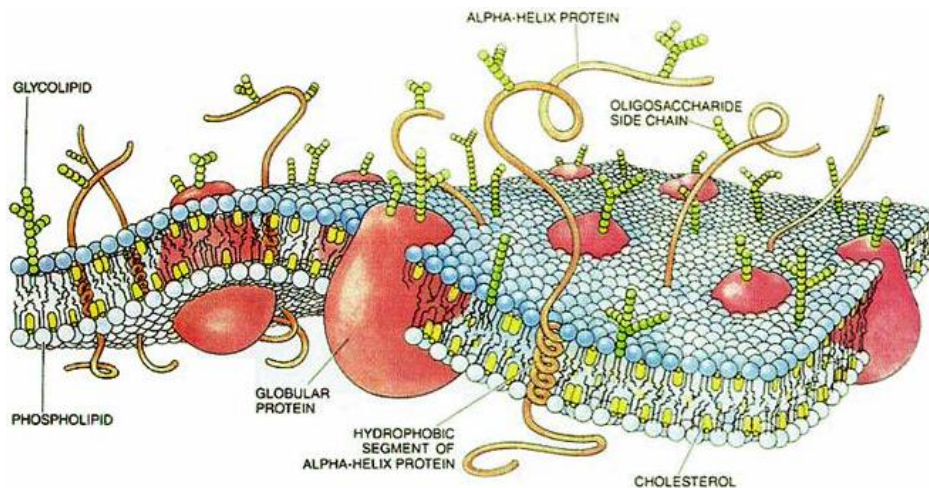


Figure 1-8: Typical cell membrane (adopted from:<http://upload.wikimedia.org/wikipedia/commons/e/ee/CellMembraneDrawing.jpg>) (Access to the internet page on 14/08/2013)

Glycosphingolipids (GSLs) are a class of sphingolipids that are the most common glycolipids in the cell membrane of mammals. Most of the glycosphingolipids are transported between the membranes as small vesicles maintaining a bilayer structure[25]. They also work as the modulator of signal transduction[26]. There are many references for the function of glycolipids in cell membrane[27-29].

In addition, during the last 10-15 years, there have been several investigations into the function of sugar-based surfactants to stabilize foam films. *n*-octyl- β -glucoside for instance can stabilize the equilibrium thickness of foam films. The long-range interactions in foam films stabilized by this nonionic surfactant are due to repulsive electrostatic double-layer forces [30].

1.3 Amphiphilic molecules and membrane systems

An amphiphilic molecule can exhibit liquid crystalline phase due to the separation of the two opposing parts (e.g. hydrophilic and hydrophobic) or 'microphase separation' [11]. Glycolipids are examples of these amphiphilic molecules. They have an intrinsic tendency to assemble in the water (and other solvent) environment. The assembly results from the tendency of the water molecules to avoid the hydrophobic parts of the molecules. In glycolipids, hydrophilic headgroups tend to interact with water molecules and the hydrophobic acyl and alkyl chains prefer each other together with other hydrophobic moieties in general. Usually, the specific form of glycolipid assembly is determined by their physicochemical properties.

The temperature-dependent phase behavior of glycolipids affects the properties of membranes. At low temperatures, a pure glycolipid bilayer is in a gel (L_{β}) phase, which is characterized by a high chain order, i.e. the chains tend to orient parallel to each other. Consequently, the lipids are closely packed, which results in a small surface area at the interface per lipid. As the temperature rises, phase transition to a lamellar (L_{α}) phase occurs. The L_{α} phase is characterized by decreased chain order and increased surface area per lipid. As the temperature increases, the volume requirements of the chain region further increase and a transition to the inverted hexagonal phase takes place. Commonly, the inclination for one or both monolayer (halves of the bilayer) to curl away from a planar arrangement is the main factor driving these transitions. This arises from an unbalanced expansion in the lateral stresses such as, pressure and tension from the head group region, the polar/non-polar interface, and the hydrocarbon chain region of the bilayer [44]. In the case of single monolayer to stay flat, the lateral interactions must be in equivalence across the monolayer. Higher lateral pressure in the head group domain than that in the chain domain of the layer causes a

trend for the layer to curl towards the chain region, this is called positive curvature. On the other hand, if the pressure in the chain domain becomes dominant, we have a negative curvature and the layer bends towards the aqueous region [45]. These different contributions to the lateral stress in a monolayer are illustrated schematically in Figure 1-9.

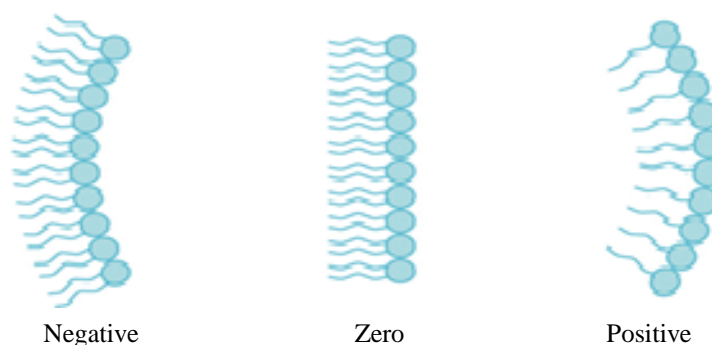


Figure 1-9: Tendency for spontaneous curvature of a lipid monolayer, due to an imbalance in the distribution of the lateral forces across the layer (Redrawn from [31])

When one monolayer tends to adopt a positive curvature and the other forms a negative curvature, the bilayer can reduce its internal stress easily by bending to form a cylindrical geometry. When these cylindrical structures assemble into a close pack arrangement, they form a hexagonal structure. It is important to understand that most lyotropic mesophases, which exist as symmetric pairs (type I) are considered as a ‘normal’ phase, such as oil-in-water, and a topologically ‘inverted’ phase (type II) water-in-oil version. The first one, i.e. the normal phase, comprises lipid aggregates in a continuous water matrix. In the second one, i.e. the reverse phase, water hydrated head group aggregates are ordered within a continuous non-polar matrix consisting of fluid hydrocarbon chains. The hexagonal phases H_I and H_{II} are examples of these pairs. We assume that the normal hexagonal phase has a positive curvature, $+\frac{1}{2}R$. In this sense, the interface bends towards the oil, or the non-polar region. On the other hand, the

inverse hexagonal phase has a negative curvature, $-\frac{1}{2}R$; therefore the interface bends towards the water region. R is the value of the cylinder radius. A basic dysymmetry between H_I and H_{II} will appear as an effect of changing the water content of these phases[14]. In swelling the H_I phase, there are no main changes in the interfacial area per molecule, whilst in H_{II} the interfacial area per lipid unavoidably increases with swelling the H_{II} phase lattice. It is obvious that by the addition of the non-polar solvent, this situation will be reversed [14].

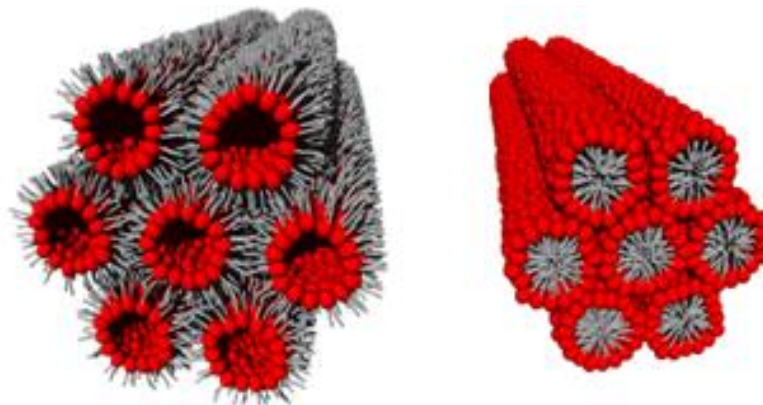


Figure 1-10: Topology of reverse H_{II} (left) and normal H_I (right) hexagonal phase (Adopted from: <http://www.biomedcentral.com/content/figures/1757-5036-2-3-3-1.jpg>) (Access to the internet page on 14/08/2013)

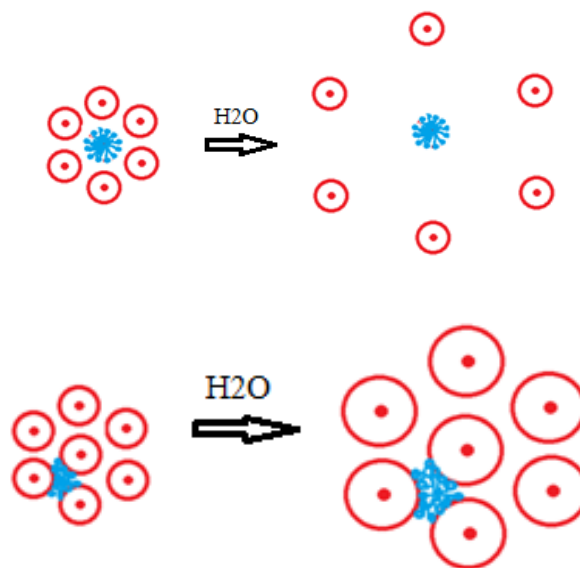


Figure 1-11: Swelling of normal H_I (up) and reverse H_{II} (down) hexagonal lattice with increasing water content [Redrawn from [14]]

If specified assumptions are made about the shape of the hydrated lipid aggregates and the densities of the components within the phase, substantive beneficial structural information can be easily obtained from the position of the diffraction lines, in relation with the chemical parameters such as the lipid molecular weight M_L , the water and lipid partial specific volumes \bar{v}_w and \bar{v}_l respectively, and the lipid weight concentration c_L (lipid / (head + water)) [44]. The volume fraction of lipid is then:

$$\phi_L = \left[1 + \left(\bar{v}_w / \bar{v}_L \right) \left((1 - c_L) / c_L \right) \right]^{-1}, \quad (1.2)$$

and the volume concentration of water is $\phi_w = 1 - \phi_L$. For the H_{II} phase, the lattice spacing (Figure 1-12) is related to the d -spacing [32] by $a = (2 / \sqrt{3})d$, and the diameter of the water cylinders is given as:

$$d_w = \left[\left(2\sqrt{3} / \pi \right) (1 - \phi_L) a^2 \right]^{\frac{1}{2}}. \quad (1.3)$$

The lipid layer thickness along the line connecting the cylinder axes is then $d_L = a - d_w$.

The minimum length of the lipid molecule l_{min} is calculated from the half thickness $d_L / 2$ in the H_{II} phase. Likewise, the distance from the interface to the center of the hydrophobic region corresponds to the maximum length l_{min} , and this is given by $a / \sqrt{3} - d_w / 2$ [33].

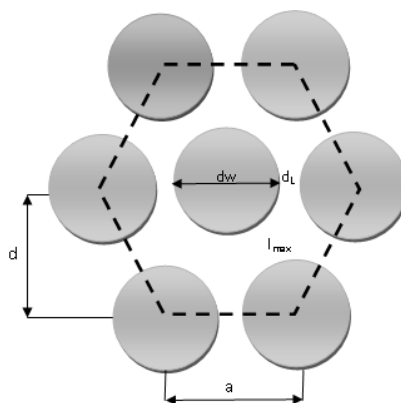


Figure 1-12: Lattice parameter and d-spacing (redrawn from <http://ars.els-cdn.com/content/image/1-s2.0-S0009308497000935-gr2.gif>)

1.4 Crown ether compounds

Crown ethers are cyclic chemical compounds that consist of a ring containing several ether groups. The term "crown" refers to the resemblance between the structure of crown ether bound to a cation, and a crown sitting on a person's head. They were first discovered by Pederson in 1967 and have long been well known for their ion selectivity[34, 35]. Crown ethers $((\text{CH}_2\text{CH}_2\text{O})_n, \text{cyclic})$, with the ether groups acting as hosts to trap the ionic species as a guest can form cationic complexes. The oxygen atoms are well situated to coordinate with a cation located at the interior of the ring, whereas the exterior of the ring is hydrophobic. The resulting cations often form salts that are soluble in nonpolar solvents, and for this reason crown ethers are useful in phase transfer catalysis. The denticity of the polyether influences the affinity of crown ethers for different cations. For example, 18-crown-6 has high affinity for potassium cation, 15-crown-5 for sodium cation, and 12-crown-4 for lithium cation. Beside this, the cavity size of the crown ether is another factor, which makes it possible for a specific entrapment of a guest particle, especially a metal cation. One can also find this kind of host-guest chemistry in Nature such as in cyclodextrins and macrocyclic polyether antibiotics[36]. Therefore, it is of special interest for researchers to understand the host-guest complex interaction, especially in view of many possible applications,

such as molecular recognition, ion sensing, heterogeneous catalysis or molecular switching [37-40].

The combination of the self-assembly behavior with a special functionality of some supramolecules has provided a way to design specific function from molecular level to the nanoscale, offering new functionality to the self-assembly system [41]. For example, incorporating cation selectivity of crown ether attached to the system of self-organization, create a cation channel, which mimics the natural protein ion-channel for bio-membranes[42-44].

Recently, a series of new compounds was prepared by Sabah *et al.*[45] which combined the self-organizing property of sugar-based glycolipids with the crown ethers (Figure 1-13). These compounds are a combination of glycolipid dodecyl- β -D-glucoside with crown ethers. The compounds 15-crown-5, 18-crown-6 and 21-crown-7 have their crown ethers attached to hydroxyl groups at O2 and O3 positions on the sugar ring of the dodecyl- β -D-glucoside to give G15C5, G18C6 and G21C7, (Figure 1-13, a-c) respectively. Meanwhile different positions of the hydroxyl groups (O4 and O6) of the dodecyl- β -D-glucoside are chosen to attach the crown ethers of the 16-crown-5 and 19-crown-6 for G16C5 and G19C6 (Figure 1-13, d-e). These new functionalized glycolipids have significantly increased size of hydrophilic heads due to the crown ethers. In terms of self-assembly packing, increase in the size of head group would result in higher packing parameters,[16] which could prevent the formation of lamellar phase and induce the formation of non-lamellar curve phases such as micellar, hexagonal and even cubic phases. In this work, we studied the properties of these compounds from a theoretical point of view. The electronic structure, molecular conformation and the thermodynamic properties of these compounds and their

complexes with cations Na^+ and K^+ were obtained from the quantum chemistry calculation using Gaussian 09W program. Through this study we can understand the possible effect of molecules on their self-assembly structure.

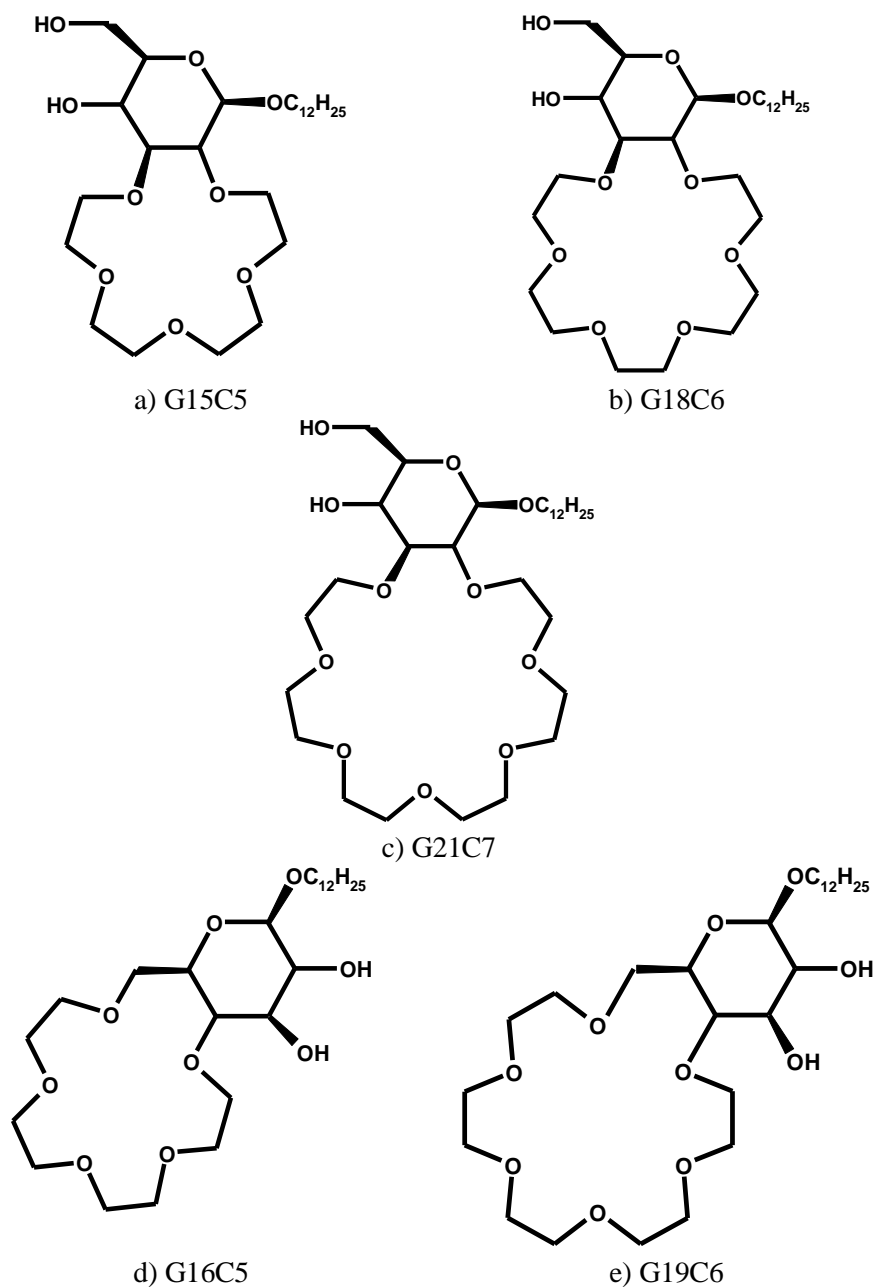


Figure 1-13: Schematic drawing of the molecular structures of glycolipids crown ethers

1.5 Molecular Dynamics Simulation

Traditionally, chemistry is an experimental science, no molecule could be investigated without prior being synthesized or found in Nature. In contrast, nowadays

with the advent of modern computers and advances in simulation technique, the dynamics and structure of molecular systems can be studied theoretically without them being synthesized nor have to be naturally occurring [46-48]. Thus, the real beauty of this technique lies in its capability to predict the properties of a well-defined model of a chemical system based on a set of rules governing them. Compatibility between the simulation results and the experimental data has encouraged scientists to apply this method widely. In modern chemistry, there are two types of modelling approaches widely used, namely molecular mechanics and quantum mechanics. Monte-Carlo (MC) [49] and molecular dynamics [50] (MD) are two simulation techniques that are commonly applied for the force field obtained from molecular mechanics [51, 52]. The Metropolis MC uses a random number to evaluate the multi-dimension integration needed to evaluate statistical averages, which define the properties of a system. In contrast to the random MC method, molecular dynamics simulation follows step wisely real time dynamics of the particles using the Newton's equations of motion. The first MD was carried out for a system of hard spheres by Alder and Wainwright [4]. Compared to MC, the implementation of MD simulation codes is more complicated, but the underlying physics is relatively simple and involves setting the equation of motion for N-particle system and solving these numerically. Of course, MD has added advantage since dynamical properties such as diffusion coefficients and viscosities may be calculated in addition to the usual thermodynamic behaviour. Here, we outline only two simple numerical solutions to these equations of motion to illustrate the technique.

Consider, $\mathbf{F}_i = m_i \mathbf{a}_i$, where \mathbf{F}_i is the resultant force exerted on particle i , m_i and \mathbf{a}_i are its mass and acceleration respectively. Expressing the force as the gradient of the potential energy, $\mathbf{F}_i = -\nabla_i U_N$ modifies the equation of motion and relates this to the derivative of the potential energy with respect to position, \mathbf{r}_i , as a function of time;

$$-\frac{dU_N}{d\mathbf{r}_i} = m_i \frac{d^2\mathbf{r}_i}{dt^2} . \quad (1.4)$$

By assuming that the acceleration is constant for linear velocity in one dimension, classical mechanics gives the following relationships:

$$\begin{aligned} \mathbf{F} = m\mathbf{a} &= m \frac{d^2x}{dt^2} , \\ a &= \frac{dv}{dt} , \quad \mathbf{v} = \mathbf{a}t + \mathbf{v}_0 , \quad x = \mathbf{v}t + x_0 . \end{aligned} \quad (1.5)$$

A combination of these equations then gives the position, x as a function of t , at a given acceleration (\mathbf{a}), the initial position (x_0) and velocity (\mathbf{v}_0). Thus,

$$x = \frac{1}{2}\mathbf{a}t^2 + \mathbf{v}_0t + x_0. \quad (1.6)$$

Although the solution to this equation for x is deterministic, a few issues remain to be addressed due to the microscopic nature of the problem. First, the method must ensure the conservation of energy and momentum which means the initial distribution of velocities, selected randomly must have magnitudes which conform to the required temperature and ensures the overall momentum, P sums to zero or $\mathbf{P} = \sum_{i=1}^N m_i \mathbf{v}_i = 0$.

Secondly, from these selected velocities, the probability P_i that a particle i has a velocity v_{ix} in the x direction may be calculated and consequently, the temperature determined, hence,

$$p_i(v_{ix}) = \left(\frac{m_i}{2\pi kT}\right)^{1/2} \exp\left(-\frac{1}{2} \frac{m_i v_{ix}^2}{kT}\right) \quad \text{and} \quad T = \frac{1}{3N} \sum_{i=1}^N \frac{|p_i|^2}{2m} . \quad (1.7)$$

Applying these to a set of N-particle system of defined interaction, U_N ,

$$U_N = \frac{1}{2} \sum_{i \neq j} U(X_i, X_j), \quad i, j = 1, \dots, N. \quad (1.8)$$

would similarly give the trajectories of N-particles if the initial particles' positions, velocities and accelerations are known. These become a system of coupled ordinary differential equations with no analytical solution, but several algorithms have been proposed to solve them numerically. Choosing an appropriate one, depends on some criteria, such as the algorithm must conserve energy and momentum, be computationally efficient and should allow for a long time-step for integration. Usually these algorithms use Taylor series expansion, equation(1.9), to express the positions, velocities (v) and accelerations (a);

$$\begin{aligned} \mathbf{r}(t + \delta t) &= \mathbf{r}(t) + \mathbf{v}(t)\delta t + \frac{1}{2}\mathbf{a}(t)\delta t^2 + \dots \\ \mathbf{v}(t + \delta t) &= \mathbf{v}(t) + \mathbf{a}(t)\delta t + \frac{1}{2}\mathbf{b}(t)\delta t^2 + \dots \\ \mathbf{a}(t + \delta t) &= \mathbf{a}(t) + \mathbf{b}(t)\delta t + \dots \end{aligned} \quad (1.9)$$

One of the earliest and easiest to implement but not necessarily the optimum is the Verlet algorithm [53], which initially calculates the position and acceleration at time t and $(t - \delta t)$ and uses these to calculate $\mathbf{r}(t + \delta t)$ as follows;

$$\begin{aligned} \mathbf{r}(t + \delta t) &= \mathbf{r}(t) + \mathbf{v}(t)\delta t + \frac{1}{2}\mathbf{a}(t)\delta t^2, \\ \mathbf{r}(t - \delta t) &= \mathbf{r}(t) - \mathbf{v}(t)\delta t + \frac{1}{2}\mathbf{a}(t)\delta t^2. \end{aligned} \quad (1.10)$$

Summing these two equations therefore gives the new position,

$$\mathbf{r}(t + \delta t) = 2\mathbf{r}(t) - \mathbf{r}(t - \delta t) + \mathbf{a}(t)\delta t^2 . \quad (1.11)$$

Since the Verlet algorithm uses no explicit velocities, it is straightforward and requires low storage, but against this, the algorithm is of a moderate precision.

Another common approach used in MD is the leap-frog algorithm [54], where both the position and velocity are evaluated from;

$$\begin{aligned} \mathbf{r}(t + \delta t) &= \mathbf{r}(t) + \mathbf{v}\left(t + \frac{1}{2}\delta t\right)\delta t, \\ \mathbf{v}\left(t + \frac{1}{2}\delta t\right) &= \mathbf{v}\left(t - \frac{1}{2}\delta t\right) + \mathbf{a}(t)\delta t. \end{aligned} \quad (1.12)$$

The velocities are first calculated at a half advanced time step, $t + 1/2\delta t$ and these are used to calculate the positions, r , at a time $t + \delta t$. In this way, the velocities leap over or are calculated first before the new positions, then the positions leap over the velocities and so on. Although the velocities are calculated explicitly, the positions are not obtained at the same time. The velocities at time t may be approximated by:

$$\mathbf{v}(t) = \frac{1}{2}\left[\mathbf{v}\left(t - \frac{1}{2}\delta t\right) + \mathbf{v}\left(t + \frac{1}{2}\delta t\right)\right] . \quad (1.13)$$

1.5.1 Force field development for carbohydrates

Atomistic simulations have different aims and challenges and one of these must be to obtain the exact properties of a real molecular system since it uses the most exact ‘realistic’ (*an initio*) model. One major problem in atomistic based molecular modeling is unfortunately, the system for realistic simulation is too large to be considered by quantum mechanical methods. Under such circumstances, molecular mechanics is

capable of performing calculations on a very large system containing thousands of atoms [55] by using some approximations such as united atom approach. A simple molecular mechanics force field contains terms of a relatively simple five component representations of the intra- and inter-molecular forces within the system such as bonds, angles, rotation (dihedral) and non-bonded interactions which contain both electrostatic and van der Waals. More sophisticated force field may have additional terms, for example polarization but invariably contain these five components. In general, the total potential energy for a molecule or assemblies of atoms and/or molecules is given as:

$$U_{total} = U_{bond}(d) + U_{angle}(\theta) + U_{dihedral}(\varphi) + U_{vdw}(r_{ij}) + U_{elec}(r_{ij}) \quad (1.14)$$

This equation can be illustrated by the schematic model for the five key contributions to a molecular mechanics force field as shown in

Figure 1-14. To simulate carbohydrate related compounds, the Assisted Model Building and Energy Refinement (AMBER) *ff99* force field augmented with the more specific force field called Glycoprotein and Carbohydrate Parameters for AMBER (GLYCAM)[56] were used. GLYCAM was developed to determine the structures of oligosaccharides and also to study oligosaccharide-protein interactions. It is so important to parameterize the correct force field because the ultimate aim in molecular modeling is to explain experimental observations and to act in a predictive capacity, e.g. drug design.

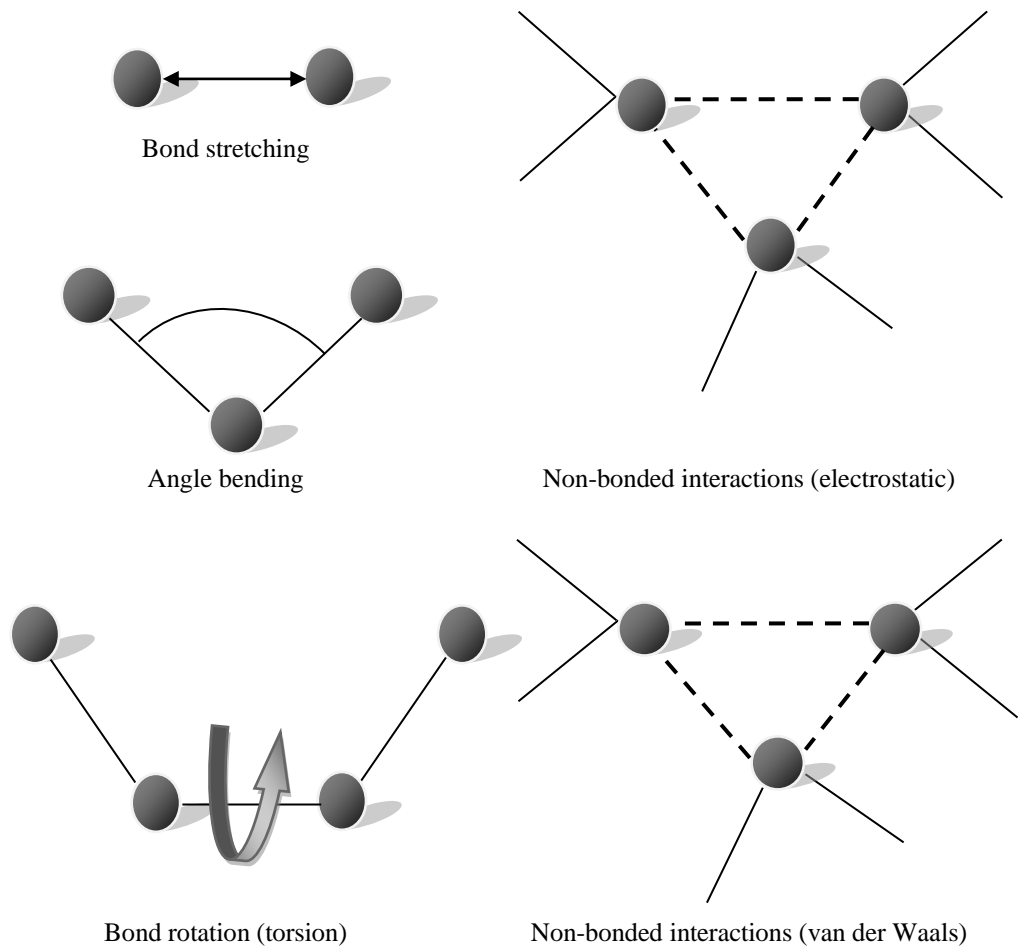


Figure 1-14: Schematic representation of bond stretching, angle bending, torsional terms and non-bonded interactions (adapted from[55])

1.5.2 System size and periodic boundary condition

Computer simulation method is a useful tool for investigating the properties of a model system. Limited by computational resources, only a small number of particles are used in simulation. In a small size system, the contribution of surface molecules to the property of the system becomes significant. However, in a real system, the number of surface molecules is very insignificant, and the contribution to the properties of the system is negligible, which means the property of the system is largely determined by the bulk molecules. Therefore, in many simulation studies, surface molecules are ignored completely and only focus on the bulk molecules by introducing the periodic

boundary condition (PBC) [57]. In periodic boundary conditions, the cubical simulation box is replicated throughout space to form an infinite lattice. During the simulation, when a molecule moves in the central box, its periodic image in each of the other boxes moves in exactly the same orientation and exactly the same way. Thus, as a molecule leaves the central box, one of its images will enter through the opposite face. Though there are no walls at the boundary of the central box, and the system has no surface, the momentum and position of the particles in the imaginary boxes are always relevant to the atoms in the original cell. Long-range electrostatic energy of each cell in a macroscopic lattice of repeating images will be calculated with the Particle Mesh Ewald (PME) summation method. Figure 1-15 shows a two-dimensional example of such a periodic system [58].

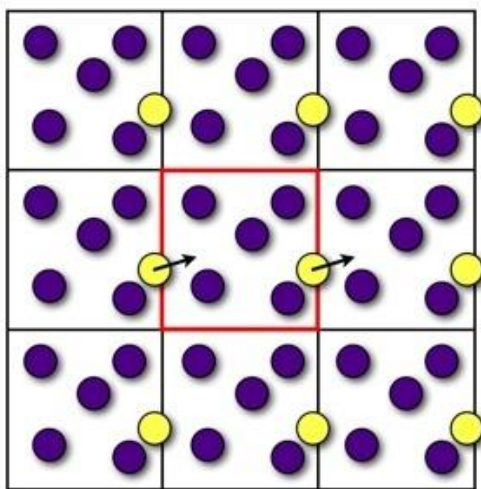


Figure 1-15: Two dimensional periodic boundary conditions (addopted from: http://matdl.org/repository/eserv/matdl:857/web_wiki2fez2465.jpg)

1.5.3 Ensembles and time averages from the MD simulations

Molecular dynamics simulations can describe the thermodynamic states of a system which contains a constant number of atoms (N), temperature (T), pressure (P), energy (E), and volume (V) [59]. Besides these, atomic positions r (in 3 dimensions),

and momenta \mathbf{p} , are two parameters used for defining the macroscopic state of a system. These are considered as coordinates in a multidimensional space called phase space. Therefore there are $6N$ coordinates for a system with N atoms [60]. Every individual point in the phase space determines the microscopic state of the system and a collection of these points is called the ensemble, which refers a specific macroscopic state. During a molecular dynamics simulation a sequence of points as a function of time will be generated in the phase space. Each point represents one configuration of the system, but all of them belong to the same ensemble. Table (1.3) shows different types of ensemble which are used in the molecular dynamics simulation. Each ensemble has an equilibrium state as follows:

Canonical ensemble (Q): minimum Helmholtz free energy (A), $A = -k_B T \ln Q$

Microcanonical ensemble (Ω) : maximum entropy (S), $S = k_B \ln \Omega$

Grand canonical ensemble (Ξ): maximum pressure and volume (PV), $PV = k_B T \ln \Xi$

Isothermal-isobaric ensemble (Δ): minimum Gibbs function (G), $G = -k_B T \ln \Delta$

Table 1-2: Terminology in thermotropic mesophases and Synonyms in lyotropic mesophases

Ensemble type	Constant parameters
Microcanonical (Ω)	N, V, E
Canonical (Q)	N, V, T
Isobaric-Isothermal (Δ)	N, p, T
Grand canonical (Ξ)	μ , V, T

For a macroscopic sample the statistical average is calculated by equation(1.15)

$$\langle A \rangle_{ens} = \iint d\mathbf{p}^N d\mathbf{r}^N A(\mathbf{p}^N, \mathbf{r}^N) \rho(\mathbf{p}^N, \mathbf{r}^N), \quad (1.15)$$

where $A(\mathbf{p}^N, \mathbf{r}^N)$ is a function of coordinates and momenta and $\rho(\mathbf{p}^N, \mathbf{r}^N)$ is the probability density function. The probability density function is defined as:

$$\rho(\mathbf{p}^N, \mathbf{r}^N) = \frac{1}{Q} \exp\left[-H(\mathbf{p}^N, \mathbf{r}^N) / k_B T\right], \quad (1.16)$$

where H is Hamiltonian, k_B is the Boltzmann's constant, T is the temperature and Q is the partition function of the system,

$$Q = \int \dots d\mathbf{r}^N \int \dots d\mathbf{p}^N \left[-H(\mathbf{p}^N, \mathbf{r}^N) / k_B T\right]. \quad (1.17)$$

Calculating thermodynamic properties such as energy (E), entropy (S) and heat capacity (C_v) according to the partition function is difficult because of multi-integrations, which calculate for all accessible states of the system. Thus a molecular dynamics simulation is a good substitute for calculating the time average properties of the system from the thermodynamics ensemble [60].

1.5.4 Long-range interactions

In a molecular dynamics simulation the most time-consuming step is the calculation of the pair-wise non-bonded interaction since this changes quadratically with the number of atoms in the system. During the last 20 years several attempts have been made and different approximations have been used to decrease the computation effort needed [61]. One of these approximations is to use the cut-off that specifies the maximum distance between pairs of atoms before computing their energy of interaction. In this case, the forces between the atoms can be omitted when they are sufficiently far

from one another. Such a cut-off distance is suitable to model the contribution of the short-range force within the Lenard-Jones potential [62]. In the last few years, long-range interaction behaviour has been investigated [63, 64] and the most useful method for truncation is the Particle Mesh Ewald summation [65]. The method of Ewald summation can be implemented on a grid. Essentially, the charges on the nuclei are mapped onto grid points, and the electrostatic problem is solved in two parts. The difference is that outside the “cut-off” the potential is not set to zero, but is solved using an approximate method. Inside the cut-off the potential energy is calculated using the Poisson equation. The grid method made the Particle Mesh Ewald (PME) approach tractable. This method is particularly important for nucleic acids, since they have polyanionic backbones. In this project the typical cut-off distance used is 9.

1.6 Schrodinger equation

A quantum mechanical model predicts the behaviour of electrons [66]. There are some properties (reactivity, electronic, magnetic and optical) that can only be calculated using a QM model because these are determined from the electronic states that cannot be approximated well using other models including the atomistic force field models [67]. The Schrödinger equation is the fundamental equation of quantum mechanics. In order to use this equation to describe the interaction of electromagnetic radiation with matter the wavefunctions of the system must first be specified. Each wavefunction describes a particular quantum state of the molecule. In order to simplify the solution of the Schrödinger equation the states of the molecule are treated as time-independent stationary states in the "zero-order approximation". The Schrodinger equation is a partial differential equation (PDE) that can be written as:

$$\hat{H}\psi = E\psi, \tag{1.18}$$

where \hat{H} is the Hamiltonian operator, ψ is the wave function and E is the total energy of the system. The wave function contains all the information about the system which is of interest to chemists and physicists. The probability density of finding a particle in a given space at a given time is $|\psi|^2$. The Hamiltonian in Schrodinger's equation is:

$$\hat{H} = \hat{T} + \hat{V} \quad (1.19)$$

where \hat{T} and \hat{V} are kinetic and potential energy operators respectively. For a single electron system such as hydrogen atom these operators are:

$$\hat{T} = -\frac{h^2}{8\pi^2 m} \nabla^2, \quad (1.20)$$

and

$$\hat{V} = -\frac{Ze^2}{r}. \quad (1.21)$$

where, m is the mass of electron, r is the distance between electron and nucleus, Z is the atomic number, e is the unit of the electronic charge and ∇^2 is the Laplacian operator, $\nabla^2 = \left(\frac{\partial^2}{\partial x^2} + \frac{\partial^2}{\partial y^2} + \frac{\partial^2}{\partial z^2} \right)$, in the Cartesian coordinate system. Solving the Schrodinger equation for any system with more than one electron is difficult. Fortunately, there are different approximations that help to solve this equation for complex systems, even though they need a long computing time. In the generalized Schrödinger equation for a multinuclear, multielectron system, ψ is a many-electron wave function and H is the Hamiltonian operator which is equal to [68]:

$$\hat{H} = -\frac{1}{2} \sum_i^{\text{electrons}} \nabla_i^2 - \frac{1}{2} \sum_A^{\text{nuclei}} \frac{1}{M_A} \nabla_A^2 - \sum_i^{\text{electrons}} \sum_A^{\text{nuclei}} \frac{Z_A}{r_{iA}} + \sum_i^{\text{electrons}} \sum_{j>i}^{\text{nuclei}} \frac{1}{r_{ij}} + \sum_A^{\text{nuclei}} \sum_{A<B}^{\text{nuclei}} \frac{Z_A Z_B}{R_{AB}}. \quad (1.22)$$

Z is the nuclear charge, M_A is the ratio of mass of nucleus A to the mass of an electron, R_{AB} is the distance between nuclei A and B , r_{ij} is the distance between electrons i and j , and r_{iA} is the distance between electron i and nucleus A . Some coupling terms appear in this Hamiltonian that makes it difficult to solve this equation without applying certain approximations.

1.6.1 Born-Oppenheimer approximation

Max Born and J. Robert Oppenheimer suggested that to simplify the Schrodinger equation, one could consider the nuclear positions as fixed and the electrons as moving around the nucleus, because of the enormous difference in mass between electrons and nuclei. Accordingly, under the Born-Oppenheimer approximation the electronic wave function depends explicitly on the electron coordinates and parametrically on the nuclear coordinates. The Born-Oppenheimer approximation gives the electronic Schrodinger equation as follows[68]:

$$\hat{H}^{el} \psi^{el} = E^{el} \psi^{el}, \quad (1.23)$$

where,

$$\hat{H}^{el} = -\frac{1}{2} \sum_i^{\text{electrons}} \nabla_i^2 - \sum_i^{\text{electrons}} \sum_A^{\text{nuclei}} \frac{Z_A}{r_{iA}} + \sum_i^{\text{electrons}} \sum_{i<j}^{\text{electron}} \frac{1}{r_{ij}}. \quad (1.24)$$

In this equation the term describing the nuclear kinetic energy is zero, and the nuclear-nuclear Coulomb term is constant. The latter needs to be added to the electronic energy, E_{el} , to yield the total energy, E , for the system.

$$E = E^{el} + \sum_A \sum_{A < B}^{nuclei} \frac{Z_A Z_B}{R_{AB}}. \quad (1.25)$$

1.6.2 Hartree-Fock approximation

The electronic Schrödinger equation (1.23) is still unsolvable and further approximations are required. At first glance, the electrons may be considered to move independently of one another. Practically, individual electrons are confined to functions called molecular orbitals, which are defined by assuming that the electron is moving within an average field of all the other electrons. The total wave function ψ , is written in the form of a single determinant (Slater determinant) which is given as:

$$\Psi(x_1, x_2, \dots, x_N) = \det \begin{bmatrix} \Psi_1(x_1) & \Psi_1(x_2) & \dots & \Psi_1(x_n) \\ \Psi_2(x_1) & \Psi_2(x_2) & \dots & \Psi_2(x_n) \\ \cdot & \cdot & \cdot & \cdot \\ \cdot & \cdot & \cdot & \cdot \\ \Psi_n(x_1) & \Psi_n(x_2) & \dots & \Psi_n(x_n) \end{bmatrix}, \quad (1.26)$$

($\Psi_n, n=1,2,\dots,n$) is the wave function of each particle. This approximation reduces a wave function in the $3N$ dimensional space to N wave functions in the 3-dimensional space, which are computationally solvable. The assumption that the electrons in the system interact with one another only through a mean field is equivalent to the approximation of the electronic wave function by a Slater determinant, thus effectively ignoring completely the electron correlation. The Hartree-Fock (HF) method provides

the ground-state energy of the system, which is slightly higher than its real ground-state energy. With regard to this, the Hartree-Fock method has a useful variational structure associated with it. Exploiting this variational structure, the Hartree-Fock method has been extended to obtain a more refined electronic structure, which is described by the multi-configuration method. A multi-configuration method is a natural generalization of the Hartree-Fock method, where a linear combination of a number of Slater determinants is used to approximate the wave function, against a single Slater determinant in the case of Hartree-Fock approximation. It can be shown that as the basis of the single electron wave function is increased to span the complete Hilbert space, the multi-configuration equations reproduce the exact quantum mechanical equations [69, 70]. The Hartree-Fock approach has been used quite extensively, over the course of last few decades. The major drawback of HF method is the exclusion of electron correlation. Moller-Plesset perturbation models start with an HF calculation and then correct for electron repulsion. Moller-Plesset perturbation theory are denoted as MP n ($n=2, \dots, 6$). In practice, MP2 and MP4 are the only methods used, since the other n 's are either too computationally expensive or do not improved the results significantly compared to those obtained from a method with less complexity (i.e. lower level approximation). In another approach to overcome the lack of electron-electron correlation in the HF method, Hohenberg, Kohn, and Sham introduce the density-functional theory (DFT), which uses the electron density to represent the ground-state energy of the system. DFT has become very popular for its accuracy, reliability, and feasibility of electronic structure calculations on a wide range of materials [71]. In this research we used the DFT method to calculate the energy of the new class of glycolipid crown ether and these contain cations such as K^+ and Na^+ .

1.6.3 Density functional theory

The density functional theory(DFT) is based on a variationl formulation, which reduces the problem of solving the Schrodinger equation of an N-electron system to evaluating the wave functions and energies of an effective single-electron system. Although, it is suitable for ground state calculation, the technique may be used to calculate the excited state [72]. DFT is based on the hypothesis that “describing the properties of a material system in its ground state is possible only with the electron density is a “principle variable” [73, 74]. This is a significant and powerful expression, to reduce the problem of solving a quantity (electronic wave-function) in the 3N-dimensional space to solving a quantity (electron-density) in the 3-dimensional space. Accordingly, [74]DFT is based on the fact that the sum of the exchange and correlation energies of a uniform electron gas can be calculated exactly when its density is known. In the Kohn-Sham formalism, the ground state electronic energy, E , is written as a sum of the kinetic energy, E_T , the electron nuclear-interaction energy, E_V , the Coulomb energy, E_J , and the exchange/correlation energy, E_{xc} .

$$E = E_V + E_J + E_T + E_{xc}. \quad (1.27)$$

Except for E_T , all components depend on the total electron density, $\rho(r)$:

$$\rho(r) = 2 \sum_i^{\text{orbitals}} |\psi_i(r)|^2. \quad (1.28)$$

Here, $\psi_i(r)$ are the so-called Kohn-Sham orbitals and the summation is carried out over pairs of electrons. Within a finite basis set (see next section), the energy components may be written as follows:

$$E_T = \sum_{\mu}^{\text{basis functions}} \sum_V \int \phi_{\mu}(r) \left[-\frac{1}{2} \nabla^2 \right] \phi_V(r) dr, \quad (1.29)$$

$$E_V = \sum_{\mu}^{\text{basis functions}} \sum_{E_T} \rho_{\mu V} \sum_A^{\text{nuclei}} \int \phi_{\mu}(r) \left| \frac{Z_A}{|r - R_A|} \right| \phi_V(r) dr, \quad (1.30)$$

$$E_J = \frac{1}{2} \sum_{\mu}^{\text{basis}} \sum_V^{\text{functions}} \sum_{\lambda} \sum_{\sigma} \rho_{\mu V} \rho_{\lambda \sigma} (\mu V / \lambda \sigma), \quad (1.31)$$

$$E_{xc} = \int f(\rho(r), \nabla \rho(r), \dots) dr. \quad (1.32)$$

Z is the nuclear charge, $r - R_A$ is the distance between the nucleus and the electron, ρ is the density matrix, $(\mu V / \lambda \sigma)$ is two-electron integrals, and f is an exchange/correlation function, which depends on the electron density and perhaps as well as on the gradient of the density. Minimizing E with respect to the unknown orbital coefficients yields a set of matrix equations.

1.6.4 Molecular orbital theory

The molecular orbital theory is an alternative approach to studying the electronic structure of molecules[75]. This theory uses the concept of the orbital to understand the electronic structure of atoms and molecules. The advantage of using an orbital is that it reduces a many-body problem to the same number of one-body problems in the study of electrons in atoms or molecules. Generally, an orbital is the quantum mechanical description (wave function) of the motion of a single electron moving in the average potential field of the nuclei and of the other electrons present in the system[75]. The difficulty in determining the average potential field of the other electrons makes it hard to obtain an accurate description of an orbital. For example, the $2s$ orbital in the lithium

atom is a function, which determines the motion of an electron in the potential field of the nucleus and in the average field of the two electrons in the 1s orbital. However, the 1s orbital is itself determined by the nuclear potential field and the average potential field exerted by the electron in the 2s orbital. In a system, all orbitals are relevant to one another and to know the form of one orbital we need to know the forms of all of them[75]. There is a mathematical solution to overcome this problem. The difference between molecular and atomic orbitals is that, in the former the orbital must demonstrate the motion of an electron in the field of more than one nucleus, as well as in the average field of the other electrons[75]. A molecular orbital generally encompasses all the nuclei in the molecule, rather than being centered on a single nucleus as in the atomic case. After defining the forms and properties of molecular orbitals, we can use the Pauli's exclusion principle to assign electrons to the molecular orbitals, in the order of increasing energy, to specify the electronic configuration and properties of the molecule[75]. According to the valence bond theory, a covalent bond is formed between two atoms by the overlap of half-filled valence atomic orbitals of each atom containing one unpaired electron (or mathematically formulation of the theory, the product of atomic orbitals). In contrast, in the molecular orbital theory the electrons are not assigned to individual bonds between atoms, but are treated as moving under the influence of the nuclei in the whole molecule.

1.6.5 The basis set approximation

In the Hartree-Fock method, the equations for small highly symmetric systems may be solved by mapping the orbitals on a set of gridpoints. Nevertheless, to express the unknown MOs (molecular orbitals) in terms of a set of known functions, all calculations use a basis set expansion. A basis set in theoretical and computational

chemistry is a set of functions (called basis functions) which are combined in linear combinations to create MOs.[76] Different types of basis functions such as exponential, Gaussian, polynomial, cube and plane wave can be used [77]. We can choose the basis function according to two different recipes. In the first recipe, the basis functions should have a behaviour, which agrees with the physics of the problem. In this case, the convergence is reasonably rapid as more basis functions are added. For bound atomic and molecular systems, the functions should go towards zero as the distance between the nucleus and the electrons becomes large [77]. In the second recipe, the chosen functions should make it easy to calculate all the required integrals. Slater type orbitals (STO) and Gaussian type orbitals (GTO) are two different types of basis functions, which are generally used in electronic structure calculations. GTO gives less accurate results but it uses a simple calculation process, making it more favorable [78]. Slater type orbital has the functional form:

$$X_{\xi,n,l,m}(r, \theta, \phi) = NY_{l,m}(\theta, \phi) r^{n-1} e^{-\xi r}. \quad (1.33)$$

where N is a normalization constant and $Y_{l,m}$ are the usual spherical harmonic functions. STOs are primarily used for atomic and diatomic systems, where high accuracy is required [78]. We can use polar or Cartesian coordinates to write Gaussian type orbitals:

$$X_{\xi,n,l,m}(r, \theta, \phi) = NY_{l,m}(\theta, \phi) r^{(2n-2-1)} e^{-\xi r^2}, \quad (1.34)$$

$$X_{\xi,l_x,l_y,l_z}(x, y, z) = Nx^{l_x} y^{l_y} z^{l_z} e^{-\xi r^2}. \quad (1.35)$$

where the sum of l_x , l_y and l_z determines the type of orbital (for example $l_x + l_y + l_z = 1$ is a p-orbital). There is a precise difference between the two sets of GTO coordinates. A d-

type GTO is written in terms of the spherical function which has five components ($Y_{2,2}, Y_{2,1}, Y_{2,0}, Y_{2,-1}, Y_{2,-2}$), but there appears to be six components in the Cartesian coordinates ($x^2, y^2, z^2, xy, xz, yz$). The latter six functions, however, may be understood as five spherical d-functions and one additional s-function ($x^2 + y^2 + z^2$). Similarly, there are 10 Cartesian "f-functions" which may be modified into seven spherical f-functions and one set of spherical p-functions. Having decided on the type of function (STO or GTO) and the location (nuclei), the most important factor is the number of functions to be used. In the minimum basis set we have the least number of possible functions. For example for hydrogen and helium only a single s-function is necessary, while for the first row elements in the periodic table two s-functions (1s and 2s) and one set of p-functions ($2p_x, 2p_y$ and $2p_z$) are required. Lithium and beryllium formally only require two s-functions, but a set of p-functions is usually also added. For the second row elements, three s-functions (1s, 2s and 3s) and two sets of p-functions (2p and 3p) are used [78]. A brief description of some common basis sets (generally called Pople Style Basis Sets) are mentioned by Jensen (1998) [78] as follows:

a) STO-nG basis sets: There are Slater type orbitals that have n PGTOs (primitive Gaussian type orbitals). This is a minimum type basis, where the exponents of the PGTO are determined by fitting to the STO, rather than optimizing them by a variational procedure. Although basis sets with $n = 2, 3 \dots 6$ have been derived, it has been found that using more than three PGTOs to represent the STOs gives little improvement, and the STO-3G basis is a widely-used minimum basis [76].

b) 3-21G: This is a split valence basis, where the core orbitals are a contraction of three PGTOs, the inner part of the valence orbitals is a contraction of two PGTOs and the outer part of the valence is represented by one PGTO. Note that the 3-21G basis

contains the same number of primitive GTOs as the STO-3G. However, it is much more flexible as there are twice as many valence functions, which can combine freely to make MOs [76].

c)6-31G:This is also a split valence basis, where the core orbitals are a contraction of six PGTOs, the inner part of the valence orbitals is a contraction of three PGTOs and the outer part of the valence is represented by one PGTO. In terms of contracted basis functions it contains the same number as 3-21G, but the representation of each function is better since more PGTOs are used [76].

d)6-311G:This is a triple split valence basis function, where the core orbitals are a contraction of six PGTOs and the valence orbital splits into three functions, represented by three, one and one PGTOs, respectively. To each of these basis sets, diffuse and/or polarization functions can be added. Diffuse functions are normally s- and p-functions and consequently written before the G, denoted by + or ++, with the first + indicating one set of diffuse s- and p-functions on heavy atoms, and the second + indicating that a diffuse s-function is also added to hydrogen. Polarization functions are indicated after the G, with a separate designation for heavy atoms and hydrogen atoms. The 6-31+G(d) is a split valence basis with one set of diffuse sp-functions on heavy atoms only and a single d-type polarization function on heavy atoms [78]. Similarly 6-311++G is a triple split valence with additional diffuse sp-functions, and two d- and one f-functions on heavy atoms and diffuse s- and two p- and one d-functions on hydrogen. The largest standard Pople style basis set is 6-311++G. These types of basis sets have been derived for hydrogen and the first row elements, and some of the basis sets have also been derived for second and higher row elements [78]. If only one set of polarization functions is used, an alternative notation in terms of * is also widely used. The 6-31G*

basis is identical to 6-31G(d), and 6-31G** is identical to 6-31G(d,p). A special note should be made for the 3-21G* basis. The 3-21G basis is basically too small to support polarization functions (it becomes unbalanced). However, the 3-21G basis by itself performs poorly for hypervalent molecules, such as sulfoxides and sulfones. This can be substantially improved by adding a set of d-functions. The 3-21G* basis has only d-functions on second row elements (it is sometimes denoted as 3-21G(*) to indicate this), and should not be considered a polarized basis [78].

1.7 Objectives and outline of the chapters in this thesis

Glycolipids are one of the principle components in the cell membrane, and play important roles in many cellular processes; therefore, there is a need to understand them at the molecular level to relate their structures to the properties of their assemblies. The combination of self-assembly with the special functionality of some supra-molecular structure provides a way to scale up this specific function from molecular level to the nano scale, offering improved performance to the self-assembly system. For example, macrocyclic ligands, like crown ethers which can bind with sugar based surfactant has the ability to increase the solubility of selected ions. Additionally, their spherical structure with metal complexation implies a large surface area for the polar head group of a crown ether-sugar based surfactant.

According to the packing theory, an increase in the surface areas of the macrocyclic head group compare to the hydrophobic chain, limits the ability of the surfactant to form a lamellar phase, but instead promotes the formation of non-lamellar phases. In this thesis, we investigate the electronic properties of synthesized sugar based crown ether molecules and proceed with the study of the self-assembly behaviour of

glycolipids in two different phases namely, two-dimensional bilayer and three-dimensional hexagonal phase.

The thesis is divided into seven chapters. The first chapter includes a general introduction on glycolipid and crown ether systems, the underlying principles of quantum mechanics and the review of some basic concepts of molecular dynamics simulation.

In the second chapter we have a brief overview of the past experimental and computational research on crown ether systems and also the investigations of the self-assembly of glycolipids in hexagonal, bilayer and micellar phases.

Methodology and technical parts of the DFT calculation of crown ether systems and their complexes with cation, the techniques used for modeling and the simulation of a reverse hexagonal (H_{II}) phase and bilayer systems are explained in Chapter 3.

Chapter 4 presents the results of the density functional theory (DFT) investigation of glucose-based glycolipid crown ethers and their complexes with alkali metal cations Na^+ and K^+ . This probe helps to have a deeper understanding of the electronic properties, molecular conformation, thermodynamic behaviour of crown ethers and their complexes with cations Na^+ and K^+ and determine the selectivity of different crown ether sugar-based surfactants toward Na^+ and K^+ .

The results from the simulation of the bilayer (thermotropic) and hexagonal (lyotropic) phases are given in chapter 5 and 6 respectively. From the simulation of the anhydrous bilayer we expected to gain knowledge on the molecular interactions within the hydrophilic region of bilayer, considers the effect of detailed stereochemistry of

sugar without any solvent and find the molecular substantiation on the likely relationship between two pairs of liner glycolipids, namely, α/β -octyl-galactosides (α/β -C₈Gal) and α/β -octyl-glucosides (α/β -C₈Glc) in thermotropic bilayer system. The interactions between the sugar head and water molecules in H_{II} phase and examine the extension and compression of the alkyl chain by calculating the distribution of average radial distance of CH₃ group over the angle around a cylinder is another achievement of this project.

Finally, in Chapter 7 we discuss the overall conclusion of the three different works in this thesis and future research undertakings as a result.

CHAPTER 2

LITERATURE REVIEW ON CROWN ETHER, BILAYER AND REVERSED HEXAGONAL SYSTEMS

2.1 Literature review of quantum study on crown ether system

Since the fortuitous discovery of macrocyclic polyethers by Pedersen in 1967 [34], there has been huge interest in these compounds as complexing agents, primarily for metal ions and also for some neutral and anionic species [79]. They exhibit strong affinity and high selectivity for alkali and alkaline earth metal ions because of a hydrophilic cavity consisting of heteroatoms, demarcated by a lipophilic envelop of ethylene units [80, 81]. Researchers use them as a model for biologically significant host-guest interactions [79]. Their specific efficiency can be found in the areas of chromatography separation, molecular transport, catalysis, selective transport and separation of metals, phase-transfer catalysis, solvation of ions in nonpolar solvents, stabilization of proton action sites in biological molecules, and isolation of radioactive components of nuclear wastes [82-84]. Apart from this, crown ethers and their behaviours in different environments are interesting for theoretical scientists. In 1990 Dang and Kollman [85] performed a molecular dynamics simulation study on the free energy of association of 18-crown-6: K^+ complex in water. They investigated the cation-crown association process in aqueous solution using thermodynamic perturbation theory and molecular dynamics simulations. They found that, when the K^+ was in the center of the crown ether, the structure with D_{3d} symmetry was the stable structure. A hybrid of quantum mechanics and molecular mechanics calculation of the nature of K^+ /crown ether interactions was published by Mark A. Thompson [86]. Their results for the simulation of K^+ /18C6 in H_2O show that the most probable K^+ /18C6 center of mass displacement is 0.25 Å. A density functional theory with B3LYP/6-31G* method has been used by Hou to explore the molecular and electronic structures for 12- to 16-crown-4 (named 12C4, 13C4, 14C4, 15C4, 16C4, respectively) and their complexes with alkali metal cations Li^+ and Na^+ [87]. Their selectivity tendency shows that among all crown ethers, the highest cation selectivity for Li^+ over Na^+ belong to the 14-crown-

4. Their finding also shows that Li^+ /crown-4 series are more stable than Na^+ /crown-4 series in the gas phase. There are many other experimental and theoretical studies in the different compounds of crown ethers to understand their nature and function of crown ethers [88-91]. The result of an *ab initio* study of 18-crown-6 and its interaction with the alkali metal cations Li^+ , Na^+ , K^+ , Rb^+ , and Cs^+ was published by Glendening *et al.* [92]. They used the Restricted Hartree-Fock (RHF) method with 3-21G and 6-31+G* basis sets to calculate the geometries, binding energies, and binding enthalpies. MP2 method was used to estimate the electron correlation effect and the wave function analysis was performed by the natural bond orbitals (NBOs) and associated methods. The result of the research showed that the strong affinity of alkali metal cations (50-100 kcal mol⁻¹, depending on cation type) was due to the electrostatic (ionic) interaction of the cation with the nucleophilic ether backbone. Also, the charge transfer (covalent bonding) has less effect on the affinity of alkali metal cations. They found that in the gas-phase and in aqueous environments, 18-crown-6 preferentially bound to Li^+ , not K^+ [92].

Martínez-Haya *et al.* [93] applied infrared spectroscopy and quantum mechanical calculation to investigate the emergence of symmetry and chirality in gas-phase complexes formed by the 18-crown-6 ether with the alkali metal cations employed. The results showed that chirality and symmetry have a dominant role in the conformational landscape of the 18-crown-6-alkali system. C_{3v} is the dominant symmetry for 18-crown-6- M^+ conformers, while C_2 for Cs^+ , D_{3d} for K^+ , C_1 and D_{3d} for Na^+ , and D_2 for Li^+ .

In 1994 Kowall *et al.* [94] applied molecular dynamics simulations on crown ether 18-crown-6 and K^+ (18-crown-6/ K^+) in aqueous solution to investigate the structure and dynamics of the hydration shell. They found that on both sides of the

crown's plane a distinct water molecule was translationally fixed by two H-bonds. From the structural and dynamical properties of the hydration shell there was a clear distinction between the hydrophilic and hydrophobic regions. A complexed K^+ ion stayed about 1 Å outside the crown's center and could be regarded as replacing one of the two "complexed" water molecules. A molecular dynamics study on the mechanism of ion selectivity in aqueous solutions of 18-Crown-6 ether was performed by Dand [95] using the potential of mean force approach to the evaluation of crown ether selectivity in an aqueous solution. The free energy profiles and the corresponding binding free energies for $M^+ : 18\text{-crown-6}$ ($M^+ = K^+, Na^+, Rb^+, Cs^+$) indicated that minimum free energy surfaces for K^+ and Na^+ were located at the crown ether center of mass. At the same time, a second minimum for Na^+ was also observed in the potential of mean force. In their investigation they also considered the relevance between the size of cation and the crown ether cavity. The calculated binding free energies were less than the experimental values, but the trend ($K^+ > Rb^+ > Cs^+ > Na^+$) in both experimental and theoretical cases was the same.

2.2 Literature review of simulation studies on micellar, bilayer and hexagonal systems

Although, lamellar being the most studied lyotropic liquid crystalline phase and useful for drug delivery and biomembranes [96], other self-assembly structures such as hexagonal, micellar etc... have also drawn research interest in both experiments and simulations. The materials forming these phases are usually amphiphilic in nature such as phospholipids and glycolipids. Since this thesis concerns glycolipids that can form various phases for example micelles, bilayers and hexagonal phases, hence this section surveys a selection of literatures related to the present studies using mainly the pre-constructed computer atomistic models.

The simplest form of self-assembly system, the micellar phase has been studied by many groups using full atomistic models of real surfactants such as sodium dodecyl sulfate (SDS). Boguszet *al.* performed probably the earliest molecular dynamics simulation on a pre-constructed model to the structural properties of glycolipid micelle of n-octyl- β -D-glycopyranoside to explore the effect of aggregate size on the structural properties of octyl glucoside (OG) micelles [97]. They have selected micelle systems containing 1, 5, 10, 20, 27, 34, 50, and 75 surfactant molecules in water, as well as an OG bilayer, and neat octane. The results showed that micelles with aggregation containing at least 10 remained intact during the 4 ns simulations. In addition, some properties such as aggregate shape and internal properties (tail length, dihedral angle distributions, and isomerization rates) did not change much during the simulation time, while the changes in surface properties (hydrophobic accessible surface area and head group cluster size) were reasonable. Following this, there was another MD investigation for the micelle size of n-octyl- β -D-glucopyranoside, n-octyl- β -D-maltopyranoside and n-octyl- β -D-galactopyranoside[98]. This work showed that the n-octyl- β -D-galactopyranoside micelle was bigger in size than the n-octyl- β -D-glucopyranoside system, a result comparable with the experimental data of small-angle neutron scattering method[99]. In another study of the micellar phase using a galactose head group, an MD simulation of n-octyl- β -D-galactopyranoside with two different initial coordinates and velocities in explicit solvent was performed by Konidala *et al.* to determine the characteristic of n-octyl- β -D-galactopyranoside aggregate[100]. They calculated geometric packing parameters and distinguished the prolate ellipsoid for the average micelle structure. In addition they calculated the radial distribution functions for the hydroxyl oxygen atoms of the n-octyl- β -D-galactopyranoside. The results showed that at a minimum van der Waals contact distance sharper peaks were observed for the

hydroxyl oxygen atoms than those for the acetal oxygen, ring oxygen and aromatic carbon atoms [100].

Recently, there has been increasing interest in the more complicated self-assembly in 2-D and 3-D ordered structures of the lyotropic liquid crystalline phases, such as reverse hexagonal (H_{II}) and reverse bicontinuous cubic phases (V_2)[101]. These phases can be stable in excess water as in the case of lamellar phase, which simplifies the preparation of nanoparticle dispersions and makes them suitable for encapsulation and controlled release of drugs. Water channel diameter and lipid bilayer thickness are two important factors in the application of reverse phases for encapsulation and controlled release[101].The result of a 10 ns MD simulation of hydrogen bonding structure and dynamics of water at the dimyristoylphosphatidylcholine (DMPC) lipid bilayer surface was presented by Lopez[102].The average of hydrogen bonds per lipid's oxygen atom was varied depending on its position within the lipid. The hydrogen bonding dynamics of water at the lipid surface investigation revealed that the life of a single-bonded lipid oxygen atom was shorter than that between the water and the double-bonded lipid oxygen atoms. Moreover, hydrogen bonds between water and the head group oxygen atoms were shorter than those between water and the tail lipid oxygen atoms[102]. Shinoda *et al.* [103] performed an MD simulation on straight- and branched-chain dipalmitoylphosphatidylcholine (DPPC) and diphytanoylphosphatidylcholine (DPhPC) respectively to understand the effect of branching on bilayer properties. A comparison between the results of these compounds showed that the higher structural stability of the branched DPhPC bilayer was attributable to the slower conformational motion of the hydrophobic chain. Also, the characteristic conformation of the branched-chain decreased the probability of parallel chains in lipid. On the other hand, to date, detailed simulation studies on glycolipids self-assembly [104-108] are

relatively rare compared to studies conducted for phospholipids bilayer systems[109, 110].

An MD simulation on 200 n-octyl- β -D-glycopyranosides solvated in 584 water molecules was performed for 1 ns, and some different parameters such as the tilt angle and the chain length to investigate the bilayer structure were calculated [111]. They found that in the case of alkyl monosaccharide glycolipids, only branched-chain compounds gave a thermotropic fluid lamellar (L_{α}) phase at room temperature, and that this phase occurred at much higher temperatures for the monoalkylated systems. At room temperature, only the gel phase (L_{β}) or lamellar crystal (L_C) phase could be observed for monoalkylated systems[112]. Recently, Manickam Achari *et al.*[108] explored the effect of sugar head group and tail branching of four anhydrous bilayers of dodecyl β -maltoside, dodecyl β -cellobioside, dodecyl β -isomaltoside and a branched-chain maltoside (β BCM_{al}-C₁₂C₁₀) in lamellar phase. They found that glycolipid chain branching had a remarkable effect on the dimensions and interactions of the lamellar assembly but this effect was rather less than in the substitution of the maltosyl head group with an isomaltosyl moiety. This investigation also showed that the microscopic properties of the glycolipid assemblies were highly affected by the sugar head group stereochemistry.

Simulation interest in non-lamellar curved phases such as the hexagonal phase appeared in the literature very recently. These phases have interesting structural and dynamic roles in biological systems[17, 113]. They can be stable in excess water as in the case of the lamellar phase. They are characterized by densely-packed, straight water-filled cylinders and exhibit a 2-D ordering[114]. These systems are considered to be active as transient intermediates in biological phenomena that require topological

rearrangement of the lipid bilayers such as in membrane fusion[115]. The first normal hexagonal phase H_I was distinguished in aqueous solution of tobacco mosaic virus by Bernal[116]. This type of hexagonal phase is widespread in biological systems, especially in DNA solutions, polysaccharides and polypeptides. After that, Mc Bain found the first normal hexagonal phase H_I of lipid/water in hydrated dodecyl sulfonic acid in 23-70% in water[117]. Consequently, Luzzati *et al.* elucidated its structure [118], and also distinguished the H_{II} phase of phospholipids in the human brain lipid at below 22 wt% water contents and 37 °C[119, 120]. The same structure was characterized by Ekwall *et al.* in the ternary surfactant system of sodium caprylate-/decanol/water[121]. In 1992, Takada *et al.* performed X-ray diffraction studies on a series of cellobios octa-alkanoates with alkyl chain lengths from 7 to 14. They observed that all components form enantiotropic discotic columnar phases, and all these formed columns were in a two-dimensional lattice. Temperature and the member of the homologous were two important factors in this kind of phases. So hexagonal ordered columnar (Colho) phases would form with $n=9-14$ while rectangular ordered columnar (Colro) phase would form with $n=7$ [122]. Francescangeli reported the evidence of an inverted hexagonal phase H_{II} of phospholipid-DNA-metal complexes that self-assembled in an aqueous mixture of neutral lipid dioleoylphosphatidylethanolamine, DNA and divalent metal cations (Fe, Co, Mg, Mn). X-ray diffraction showed cylindrical DNA strands that arranged on a two-dimensional hexagonal lattice and covered by a lipid monolayer[123]. Recently, Zahid *et al.* showed the stable hexagonal phase of β -D-maltoside (comprised 65% (w/w)), using fluorescent probes[124]. A molecular dynamics study of the hexagonal mesophase of sodium dodecylsulphate (SDS) in aqueous solution has been carried out by Sanjoy[125]. The simulation system consisted of two cylindrical aggregates, each containing 128 SDS and 4350 water molecules plus 256 sodium counterions. The simulation production time was 260ps and it was

conducted at $T = 333\text{K}$. The result showed a small distortion from the ideal hexagonal symmetry. Meanwhile, Vesselin Kolev and coworkers [126] used molecular dynamics simulation to investigate the structure of water inside the cylinder of the inverse hexagonal mesophase (H_{II}) of glyceryl monooleate. They used an NVT ensemble and the simulation time was 10 ns with GROMACS software [126]. Radial distribution function, distribution of hydrogen bonds and density of a water molecule across the water cylinder showed the presence of water structure deep in the cylinder. A computer simulation of a hexagonal assembly for a Guerbet-type maltoside involving a long symmetrically branched-chain alcohol was performed by Chong [127]. This model consisted of 224 glycolipids and 560 water molecules. The simulation time was 5 ns at $300\text{ }^\circ\text{K}$ using Amber package [128]. They found stable hexagonal structures and classified water as bond water.

There are several experimental investigations on the transition from lamellar to an inverted hexagonal phase and also on the behaviour of the hexagonal structure for a variety of systems [129-132]. To study such phenomena, a fully atomistic simulation model is unsuitable. Therefore, many coarse-grain simulation models have been proposed. For example, Corsi *et al.* reported a coarse-grained molecular dynamics simulation of H_{II} phase formation in a dsDNA-HL system as a function of hydration, and a change from L_α to H_{II} [133]. They showed that a coarse-grained MD simulation is a powerful tool to understand and design novel lipoplex systems. Marrink and Mark also used coarse-grained (CG) molecular dynamics simulation to study the transition pathway from a multilamellar to an inverted hexagonal. They used the Lennard-Jones potential and considered every 4-6 heavy atoms as a single coarse-grained interaction center. On a nanosecond timescale, they saw spontaneous stalks formation from

multilamellar configuration, and finally, these stalks elongated to form the inverted hexagonal phase[134].

In the next chapter we demonstrate the methodology and quantum calculation of glycolipid crown ether system with GAUSSIAN 09 and also the initial configuration, model building procedures and molecular dynamics simulation with AMBER and GROMACS which are used for the simulation of bilayer systems (thermotropic phase) and also the simulation of hexagonal phase respectively.

CHAPTER 3

RESEARCH METHODOLOGY

3.1 System description and quantum calculations of sugar-based glycolipids with the crown ether

In this part of the project we used the Avogadro software package [135] for preparing the primary structures of five compounds which are combination of glycolipid dodecyl- β -D-glucoside with the crown ether attached to hydroxyl groups at O2 and O3 namely 15-crown-5 (G15C5), 18-crown-6 (G18C6) and 21-crown-7 (G21C7) and also 16-crown-5 (G16C5) and 19-crown-6 (G19C6) with the crown ethers attached to the hydroxyl groups at O4 and O6. The Molecular mechanics of Merck Molecular force field (MMFF94) available within the software was used to minimize the conformational energies for these models (Figure 3-1). Using these optimized conformations, glycolipid crown ether complexes with cations Na^+ or K^+ were prepared by bringing the cation close to the crown ether ring (Figure 3-2 and Figure 3-3). Further MMFF94 minimizations were performed to obtain the optimized complexes so that all oxygen atoms on the crown ether ring were as close as possible to the cations. These optimized structures and their complexes were studied using the density functional theory (DFT) at B3LYP/6-31 G* level. All the calculation was carried out using the Gaussian 09 program package [136]. The DFT method is an efficient method in the study of large molecules and has been widely used since it is capable of giving sufficiently accurate conformational analyses and thermodynamics properties. Meanwhile the B3LYP (Becke-Lee-Yang-Parr) version of DFT is the combination of Becke's three-parameter nonlocal hybrid functional of exchange terms [137] with the Lee, Yang and Parr correlation functional [138]. The basis set able to reproduce experimental data [139, 140].

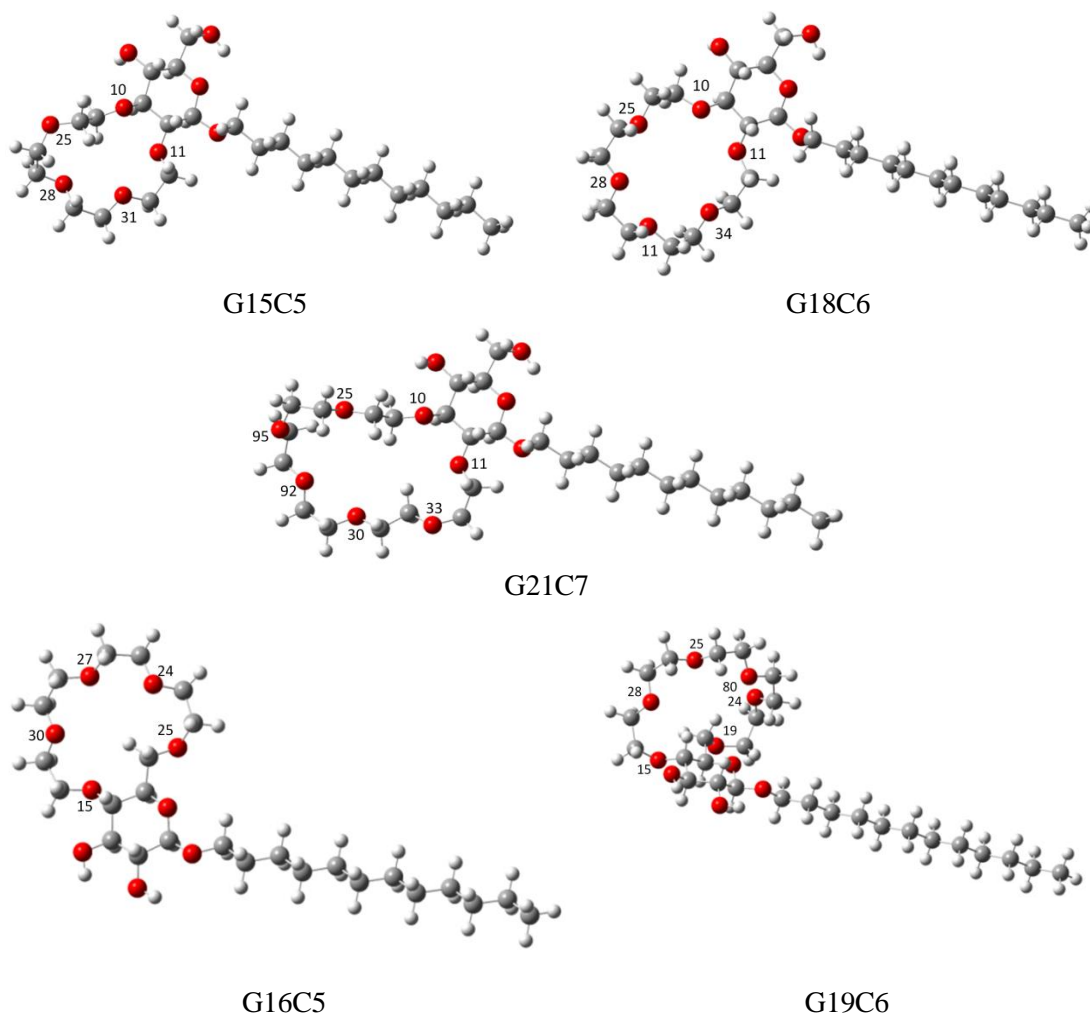


Figure 3-1: The optimized structures of the series of glycolipid crown ethers with the level of theory B3LYP/6-31G*.

Using the DFT method, the best minimum energy conformations were achieved by full geometry optimization of each crown ether glycolipid. In order to prove that each conformation is located at a stable minimum point of the potential energy surface, frequency calculations were carried out based on these optimized structures to subsequently obtain their vibrational frequencies. Furthermore, using the results obtained from the calculation, electron affinity (A) and condensed Fukui functions

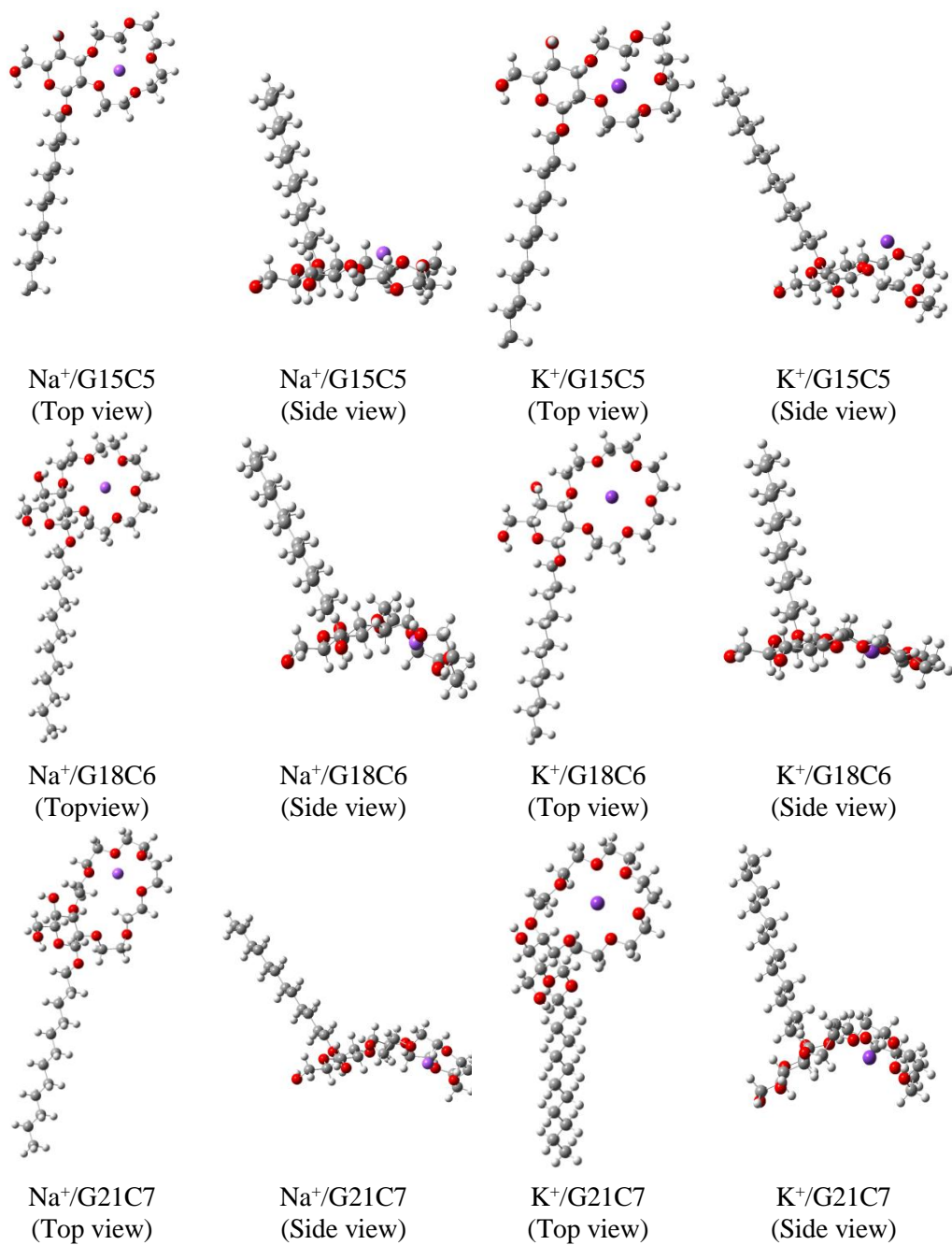


Figure 3-2: The optimized structures of complexes $M^+/G15C5$, $M^+/G18C5$ and $M^+/G21C5$ at the level of theory B3LYP/6-31 G* where M^+ represent the cations Na^+ and K^+

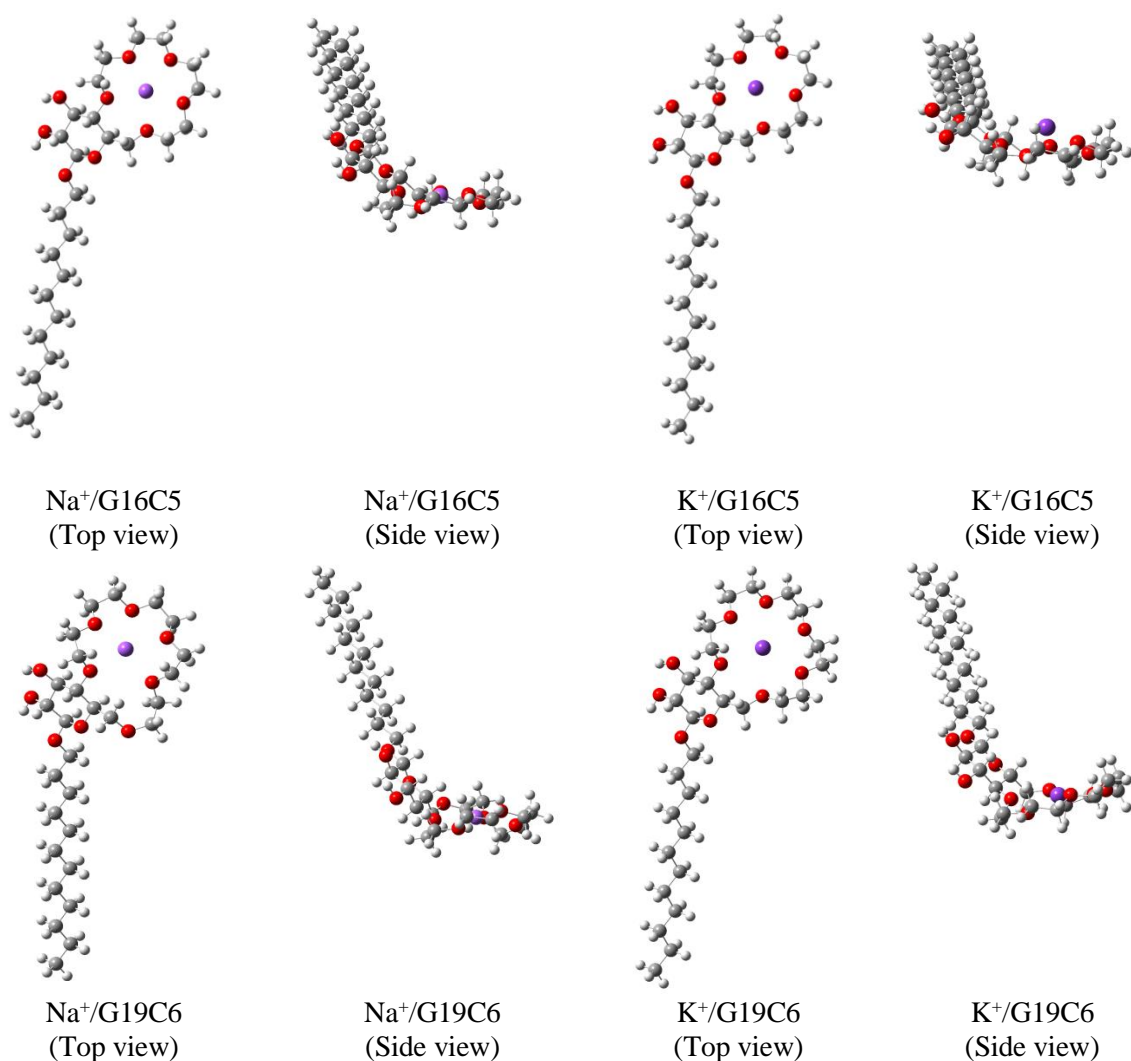
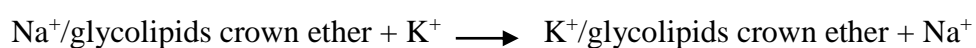


Figure 3-3: The optimized structures of complexes M⁺/G16C5 and M⁺/G18C5 at the level of theory B3LYP/6-31G* when M⁺ represents the cations Na⁺ and K⁺

(f^+) were investigated. The thermodynamic properties such as binding energy (ΔE^b), binding enthalpy (ΔH^b) and Gibbs free energies (ΔG^b) in gas phase of the complexes, formed by the combination of the glycolipids crown ethers with cation Na⁺ and K⁺, were also studied. The calculations were based on the reaction scheme 1 as follows:



In addition, the exchange enthalpies (ΔH) and the Gibbs free energies (ΔG) were also calculated for the reaction scheme 2 as follow:



It was known that a finite basis set such as 6-31 G*, can give rise to the basis set superposition error (BSSE) in the DFT calculation involving interaction of two different fragments, which in our case is between a glycolipid crown ether and a cation. To remove this error, the counterpoise method was applied in the DFT calculation of the complexes. The Simon and Boys[141, 142] counterpoise correction is a prescription for removing BSSE. In this method the interaction energies between two atoms or molecules A and B are typically calculated as the energy difference between the product complex AB and its components A and B:

$$E_{int} = E(AB, r_c) - E(A, r_e) - E(B, r_e). \quad (3.1)$$

r_c indicates the geometry of the product complex AB while r_e indicates the geometry of the separate reactants.

3.2 Calculated parameters

3.2.1 Electronic chemical potential and electronegativity: Bridging computational and conceptual DFT

Base on the excellent work of Parr *et al.*[143, 144] most of the frontier-electron theory of chemical reactivity can be rationalized from the density functional theory of the electronic structure of molecules [45]. For a system of N electrons with ground-state energy $E(N, v)$, where v is the potential energy acting on an electron due to the presence of all nuclei, several quantities of fundamental importance can be defined. The chemical potential μ could be written as a partial derivative of the system's energy E with respect to the number of electrons N at a fixed external potential $v(r)$,

$$\mu = \left(\frac{\partial E}{\partial N} \right)_{v(r)}, \quad (3.2)$$

In the early 1960s, Iczkowski and Margrave [145] explained that the energy E of an atom could be reasonably well represented by a polynomial in the order of n (where n equals the number of electrons (N) minus the nuclear charge (Z)) around $n=0$, on the basis of experimental atomic ionization energies and electron affinities:

$$E = E(N) = an^4 + bn^3 + cn^2 + dn; \quad n = N - Z \quad (3.3)$$

By considering the continuity and differentiability of E , the slope $-\left(\frac{\partial E}{\partial N} \right)_{N=0}$, at $n \rightarrow 0$ was simply seen as a measure of the electronegativity, χ [146]. Iczkowski and Margrave suggested defining the electronegativity as this derivative for fixed nuclear charge, so that:

$$\chi = -\left(\frac{\partial E}{\partial N} \right), \quad (3.4)$$

Since the cubic and quadratic terms in equation (3.3) were negligible, Mulliken's definition, [147]

$$\chi = \frac{1}{2}(I + A), \quad (3.5)$$

where I and A were the first ionization energy and electron affinity, respectively was calculated from:

$$I = E(N-1) - E(N), \quad (3.6)$$

$$A = E(N) - E(N+1), \quad (3.7)$$

where $E(N)$, $E(N-1)$ and $E(N+1)$ were the calculated total energies for the neutral, cationic and anionic states [148].

The linking of the chemical potential concept to the fundamental equation of density functional theory, bridging conceptual and computational DFT is a remarkable development [146]. The sharp definition of χ (electronegativity) and moreover, its form afford its calculation via electronic structure method [146]. The analogy with the thermodynamic chemical potential μ_i , of a component i in a macroscopic system at temperature T and pressure P [149]:

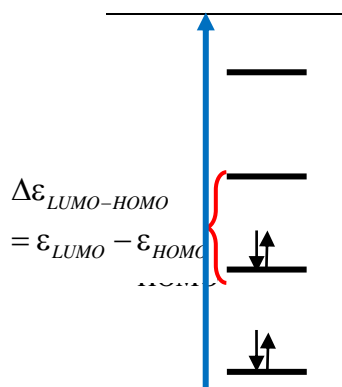
$$\mu_i = \left(\frac{\partial G}{\partial n_i} \right)_{P,T,n_j(j \neq i)}, \quad (3.8)$$

where n_j and μ_j refer to all species other than species i . Gibbs energy G is the chemical potential that is minimized when a system reaches equilibrium at constant pressure and temperature. Its derivative with respect to the reaction coordinate of the system vanishes at the equilibrium point. As such, it is a convenient criterion of spontaneity for processes with constant pressure and temperature [150]. If ΔG of a certain reaction is negative, this reaction is a spontaneous reaction and thermodynamically it is a useful reaction [93].

3.2.2 HOMO and LUMO

From the molecular orbital (MO) theory a linear combination of atomic orbitals (LCAO) forms bonding and antibonding molecular orbitals. The bonding orbital is at a lower energy than the corresponding antibonding orbital, so the bonding orbital is the first to be occupied. To understand molecular reactivity, it is important to identify the highest occupied molecular orbital (HOMO) and the lowest unoccupied molecular orbital (LUMO) [151]. They are also called the frontier orbitals. The energy difference between the LUMO and HOMO (i.e. the energy gap) ($\Delta\varepsilon_{LUMO-HOMO} = \varepsilon_{LUMO} - \varepsilon_{HOMO}$) is the key parameter for understanding the electronic structures. The energy gap is related to the polarizability and chemical hardness of the molecules, where a higher energy gap means lower molecular polarizability and higher chemical hardness [148]. In fact according to the Koopman theorem [152] chemical hardness η is equal to the energy gap.

Table 3-1: Comparison between HOMO and LUMO orbitals

	LUMO lowest unoccupied molecular orbital	<ul style="list-style-type: none"> * LUMO receives electrons, * Lowest energy orbital available, * Characteristic for electrophilic component.
	HOMO highest occupied molecular orbital	<ul style="list-style-type: none"> * Electrons from the HOMO are donated * Most available for bonding * Most weakly held electrons * Characteristic for nucleophilic component

3.2.3 Fukui Function

The local nucleophilicity and electrophilicity refer to the capability of a site in a particular molecule to donate or attract electron, respectively. Fukui function is used to describe this local reactivity toward an electron donor or acceptor. Parr and Yang [143] defined Fukui function $f(\vec{r})$, as follows:

$$f(\vec{r}) = \left(\frac{\partial \rho(\vec{r})}{\partial N} \right)_{v(\vec{r})}, \quad (3.9)$$

where $\rho(\vec{r})$ is the electron density and

$$N = \int \rho(r) dr, \quad (3.10)$$

is the total number of electrons, and $v(\vec{r})$ denotes the external potential of the system. In chemistry, one is seldom interested at which “point” in a molecule is most reactive; rather one wishes to identify which atom in a molecule that is most likely to react with an attacking electrophile or nucleophiles [153]. To achieve this, Yang and Mortier [144] proposed the condensed Fukui function. The condensed Fukui function calculation is based on the finite difference approximation and the electron density $\rho(\vec{r})$ between atoms in a molecular system. With the approximation, the Fukui function at the atom k , is denoted as f_k^+ and f_k^- , and can be estimated by using an atomic charge partitioning scheme, such as Mulliken population analysis [144]. Here, for a nucleophilic attack,

$$f_k^+ = q_{N+1} - q_N, \quad (3.11)$$

and for an electrophilic attack,

$$f_k^- = q_N - q_{N-1}, \quad (3.12)$$

q_N , q_{N-1} and q_{N+1} denote the charges for atom k on the neutral, cation and anions species respectively. While the condensed Fukui function gives the nucleophilicity locally at each atom, the overall or global nucleophilicity or electrophilicity [154] of the

systems can be measured according to their ionization potential I equation (3.6) and electron affinity A (3.7). Using the estimated I and A , we analyzed the global nucleophilicity according to the nucleophilicity index N defined as:

$$N = \left(\frac{(I + A)^2}{8(I - A)} \right)^{-1}. \quad (3.13)$$

3.3 System description and molecular dynamics simulation details of thermotropic bilayer phase

Each starting glycoside molecule (α/β -C8Gal and α/β -C8Glc) was built and geometry optimized using the HyperChem package [29]. The initial structure of each single bilayer of α/β -C8Gal and α/β -C8Glc was obtained by arranging a 10×10 array of 100 optimized lipids in the x and y plane, which constituted the first monolayer leaflet. The bilayer with the tail groups pointing to its center and the head groups facing the opposite direction was obtained using packmol [30]. GLYCAM_06d [25] and the *ff99* [31] force fields were used to assign the atom types, bond length, bond angle, dihedral angle and partial charges for the carbohydrate head group and the tail group, respectively. The GLYCAM_06 contains all the parameters for sugar and lipids [25]. For carbohydrates, it has a single parameter set applicable to both α - and β -anomers and to all monosaccharide ring sizes and conformations [25]. The *ff99* force field is a derivative of the original Cornell *et al.* *ff94* force field [32], where improvements have been made in many torsional parameters. Such parameterization supports both additive and non-additive (polarizable) force fields [32]. The *ff99* force field has been extensively used for MD simulation of the biomolecular systems [26,33,34]. Additionally, alkyl chain carbon atoms on α/β -C8Gal and α/β -C8Glc were assigned a charge of zero implying non-ionic surfactant nature. The molecular dynamics (MD) simulation was performed on each system using AMBER12 software package [23,24]. Prior to the actual molecular dynamics run, the energy minimization using first the steepest descent (SD) algorithm followed by applying the adopted basis Newton-Raphson method, was performed to eliminate any unfavorable contacts and overlapping of atoms resulting from the model building procedure [23]. Pre-equilibration under the constant number of particles N, volume, V and temperature, T, (NVT-ensemble) of the energy minimized structures was performed for 2 ns by increasing the temperature from

0 to 90°C using the Andersen thermostat ($\tau_P = 0.5$ ps) [35] with a 1 fs time step. Subsequently, the molecular dynamics simulation of the glycolipid lamellar system was carried out under the condition of constant number of particles N , pressure, p and temperature, T (NpT -ensemble). Periodic boundary conditions were applied to the simulation box in all three coordinate directions (with x , y in the bilayer plane and z normal to the bilayer) in cubic lattice geometry. The Berendsen pressure coupling method is normally used to simulate the bilayer system either anisotropically or semi-isotropically [36]. In the anisotropic case, the three unit-cell dimensions fluctuate independently, and the total pressure p remains constant 1 bar, corresponding to an $Np_x p_y p_z T$ ensemble, unlike the semi-isotropic case, which gives an $Np_N p_L T$ ensemble, where p_N and p_L are pressures along the normal and lateral to the bilayer respectively. In general, the two pressure coupling methods produce equilibrium properties, which cannot be differentiated statistically [14]. However the advantage of the semi-isotropic case is, the interface maintains a square, while in the anisotropic case the simulation box fluctuates independently in x and y directions [37]. Therefore, in our simulation we have used the semi-isotropic pressure coupling method, with a time constant 1ps and a compressibility of 4.5×10^{-5} /bar. The simulation temperature was set at 363 K for all the four glucosides. At this temperature, L_α phase is stable for three of these systems, namely α/β -C8Glc and α -C8Gal, while for β -C8Gal, it is at the border of L_α and L_C phases.

Non-bonded interactions were truncated with a cut-off range of 9.0 Å and long-range electrostatic interactions were treated using the particle mesh Ewald summation method [38,39]. The SHAKE algorithm was used to constrain covalent bonds involving hydrogen atoms [40]. The time step was 1 fs and the simulation's trajectories were saved once every 5 ps. The simulation was performed for a total duration of 200 ns dynamics. In order to monitor the equilibrium condition of the bilayer, we monitored

two parameters: area per lipid and the local density profiles (LDPs). Block averages of the local density profiles (LDPs) over 20 ns were calculated for the entire 200 ns simulation. The LDPs show small fluctuation in the interface, but does not change significantly after 40 ns, so we assume 40 ns is sufficient for the system to reach its equilibrium and the bilayer properties are calculated from the last 160 ns. The area per lipid is very sensitive to the simulation details and is generally considered to be a reliable criterion for comparing and validating the simulation results [14]. Incidentally, these simulations were performed using the GPU-accelerated version of the *pmemd* simulation engine on NVIDIA Tesla graphic card. A typical simulation performance for these systems on a normal PC-hardware is 18ns/day, which is more than an order of magnitude higher than that of a typical CPU-based simulation [41].



Figure 3-4: Schematic structure of *n*-octyl- β -D-glucopyranoside (β -C₈Glc) in HyperChem

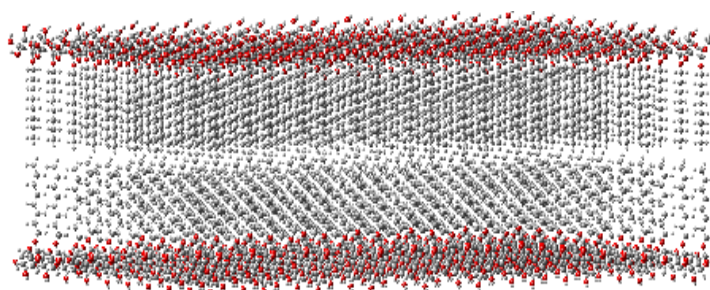


Figure 3-5: Schematic structure of bilayer system in thermotropic phase in packmole

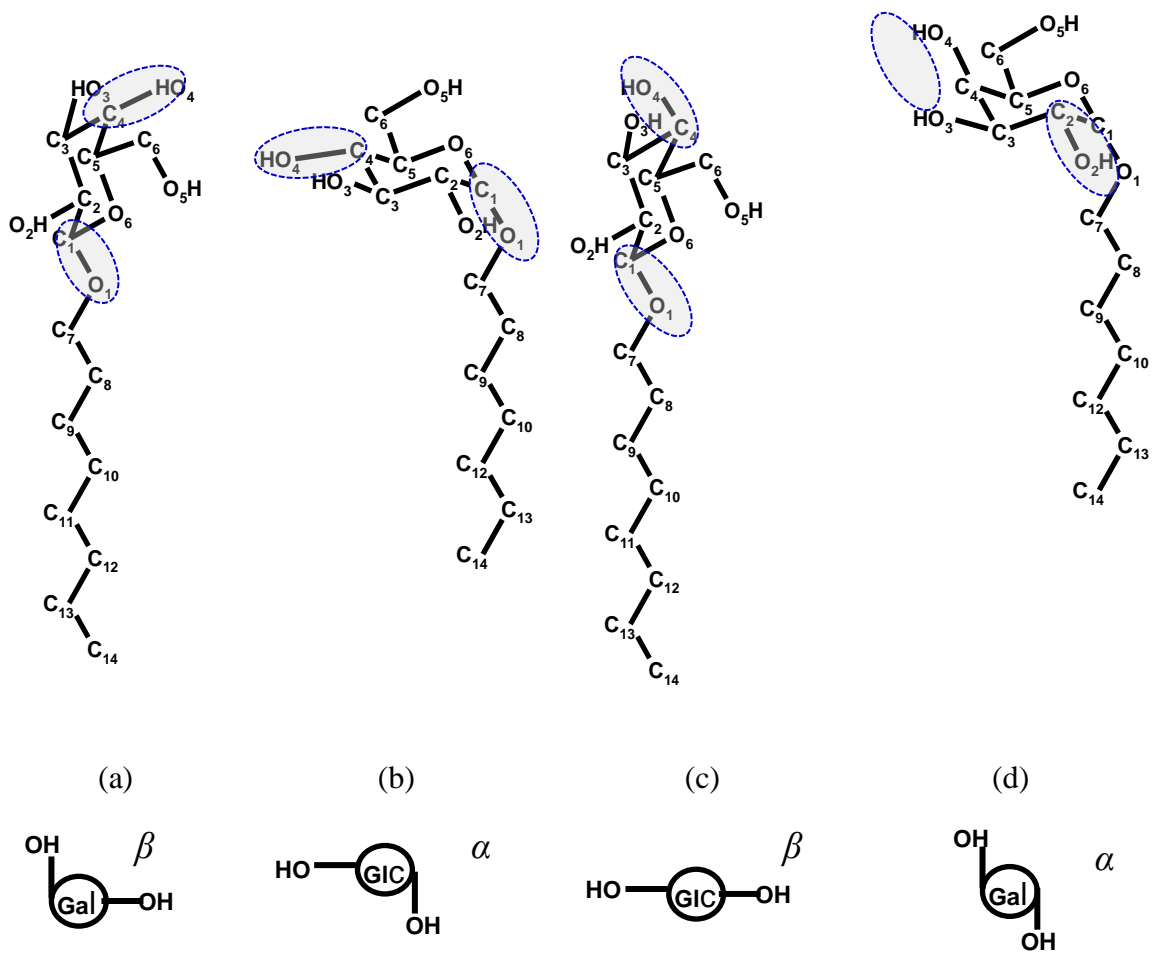


Figure 3-6: Chemical structures for glycolipids, a) *n*-octyl- β -Dgalactopyranoside (β -C₈Gal), b) *n*-octyl- α -D-glucopyranoside (α -C₈Glc), c) *n*-octyl- β -D-glucopyranoside (β -C₈Glc) and d) *n*-octyl- α -D-galactopyranoside (α -C₈Gal)

3.4 System description and molecular dynamics simulation details of the reverse hexagonal phase

We began by constructing a full atomistic model of $C_8C_{12}\beta$ -D-Glc (see Figure 3-7 a) using the modelling software package of Avogadro,[155] followed by a brief energy minimization using the molecular mechanics with MMFF94 forcefield [156]. Subsequently, in the pre-constructed atomistic model of $C_8C_{12}\beta$ -D-Glc, all hydrogen atoms were removed except the four hydrogen atoms from the hydroxyl groups within the sugar unit. Hence, a united atom model was built (see Figure 3-7, b), whose carbohydrate force field was obtained from GROMOS [157].

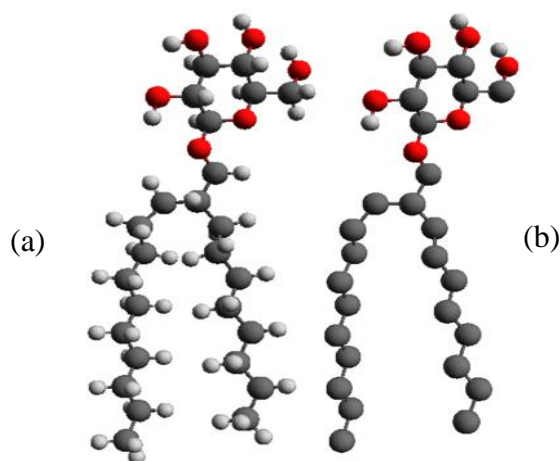


Figure 3-7: Full atomistic model of (2'-n-octyl-n-dodecyl)-β-D- glucopyranoside ($C_8C_{12}\beta$ -D-Glc), (b) United atom model of $C_8C_{12}\beta$ -D-Glc.

In order to construct the initial configuration of the reverse hexagonal phase using the united atom model of $C_8C_{12}\beta$ -D-Glc, the following steps were applied. Firstly, the $C_8C_{12}\beta$ -D-Glc was replicated into a number of copies. These were arranged into a disc with a hole in the middle. Ten of these disc aggregates were stacked to form a column. The column was replicated and arranged into a hexagonal lattice (see Figure 3-8 (a)). Separately, a configuration of randomly distributed water molecules residing in a rectangular box was generated using the *genbox* utilities software in the GROMACS MD simulation package [158, 159]. The length of the rectangular box along

its long axis was set according to the length of the column. In addition, the surface area perpendicular to its long axis was made small enough for the box to be inserted into the hollow space of the column. The water box was later replicated six times and each of these was inserted into the hollow space of the column. Subsequently, this configuration was used as the initial structure of the H_{II} phase in the simulation as shown in Figure 3-8 (b), where the yellow dotted lines indicate the boundaries of the periodic box.

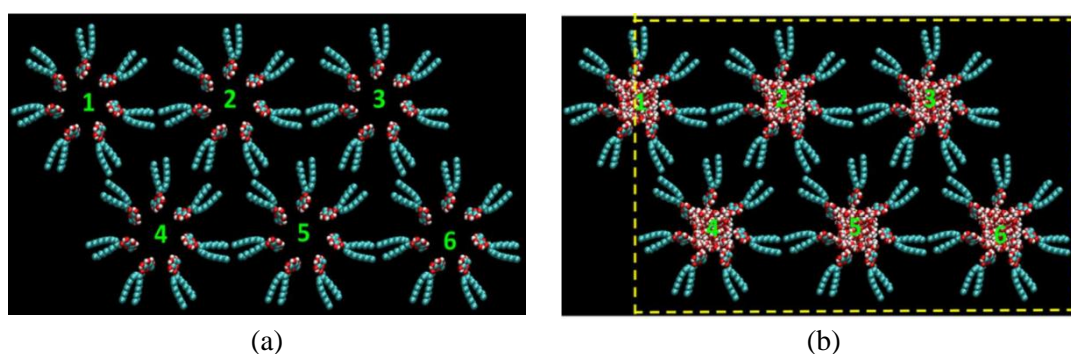


Figure 3-8: (a) Six columns of $C_8C_{12}\beta$ -D-Glc arrange in a hexagonal lattice. (b) The initial configuration for MD simulation, where the yellow lines indicate the periodic boundary.

Our approach in setting the periodic boundary condition is similar to the one used by Bandyopadhyay *et al.* [160]. Each column was assigned to a number in order to keep track of any changes during the simulation. In the construction of a single column, the size of the hole depends on how close the nearby $C_8C_{12}\beta$ -D-Glc molecules are to each other, when arranged into a column structure. It should be made large enough to accommodate the targeted number of water molecules, i.e. 1746 and 3023 water molecules, making a total number of 20,358 and 24,189 atoms for the 14% and 22% systems, respectively. These two concentrations were chosen since small angle X-ray measurements have been reported and corresponds a reverse hexagonal phase. In addition, at the 22% water concentration, the phase exists in an excess water condition which is more biologically relevant.

In the simulation, the starting structure can affect the time the simulation takes to achieve the equilibrium. The closer the initial hexagonal structure is to the experimental one, the faster the simulation will reach the equilibrium state that agrees with the real system. However, compare to the flat membrane like bilayer model system, it is relatively hard to construct the initial structure of a H_{II} phase that is close to the equilibrium state. Therefore, we tested on a number of different initial structures, each of which differed in terms of the radius and length of the hollow space, hence the size of the rectangular box of water molecules. These initial structures were first energy minimized using the steepest descent method to remove the bad contact between molecules; subsequently followed by MD simulations with constant pressure (NPT) performed for 5 ns at temperature $T = 298\text{K}$. From this series of simulations, the system whose result that gave the average lattice parameter closest to the experimentally measured value after 5 ns simulation was chosen. Amongst the configurations generated from the chosen simulation system, we further selected the frame, which matched closely the experimentally measured lattice parameter. The selected frame became the starting configuration for a further MD simulation of 50 ns. In this work we focused on two systems of H_{II} formed by $C_8C_{12}\beta\text{-D-Glc}$ at different water contents of 14% and 22%, respectively. Here, water molecules were modeled as the simple point charge (SPC)[161].

Energy minimization was performed to each of the initial configuration of the two systems, followed by 50 ns constant pressure simulation, where the first 10 ns was taken as the equilibration stage, while the last 40 ns was considered as the production stage. All the simulations applied the periodic boundary condition and leap-frog algorithm for the integration of the Newtonian equations of motion with a time-step of 2 fs. In addition, LINCS algorithm was used to fix the bond length involving the hydrogen atom.

The particle mesh Ewald (PME) approach was employed to calculate the electrostatic interactions with a cutoff of 12 Å. The cutoff of 12 Å was applied for the non-bonded interaction. The temperature was controlled by the Nose-Hoover thermostat, while the isotropic pressure was applied using the Parrinello-Rahman pressure coupling.

3.5 Calculated parameters

3.5.1 Lipid tail and order parameter

In order to monitor the stability of the bilayers, 20 ns block averages[108] of the local density profiles(LDP) were calculated up to 200 ns. Generally, the LDP was calculated along the bilayer normal, taking the centre of the bilayer as the origin. This distribution function $g(Z)$ was calculated from the number density, $\rho(x, y, z)$, given as:

$$N = \iiint \rho(x, y, z) dx dy dz, \quad (3.14)$$

where N is the total number of atoms. Along the z -direction, we defined $g(Z)$ as:

$$N = \iiint \rho(x, y, z) dx dy dz, \quad (3.15)$$

$$g(z) = \rho(z) / \rho = (N(z)V) / (NA\Delta z). \quad (3.16)$$

where A is the bilayer area, ΔZ is the bin size along the z -axis, and V is the volume.

3.5.2 Area at the interface per sugar head

the convergence of the simulated system to its equilibrium state may be monitored through the time evolution of the area per lipid calculated by dividing the total area in the x and y directions of the bilayer by the total number of glycolipids (100) in a single bilayer leaflet[162]. Area per lipid is one of the parameters that can be used to determine how well equilibrated the simulated system is[163] because among the bulk quantities it gives a more detailed convergence perspective[164]. It was found that from the total 200 ns simulation run, the first 40 ns dynamics could be regarded as the equilibrium phase. Subsequently, for the analysis purpose, every 5 ps frame was archived from the last 160 ns dynamics.

3.5.3 Lipid tail and order parameter

The conformational disorder of the hydrophobic chain is related to the bilayer stability under the mechanical stress and it is more disordered in a liquid-crystal state than in a gel or a crystal state[164]. Therefore the chain order parameter S_{CH} has been used to estimate the degree of ordering in the chain region. This is derived from the general 3×3 Saupe ordering tensor, S whose element, S_{ij} is given as:

$$S_{ij} = \frac{1}{2}(\overline{3\cos\theta_i\cos\theta_j} - \delta_{ij}), \quad (3.17)$$

where θ_i is the angle between the i^{th} molecular axis and the bilayer normal, and the bar represents the time or ensemble averaged quantity [165]. The alkyl chain order parameter was defined according to van der Ploeg and Brendsen[166], where the molecular axes for the n th methylene group are defined by the H-H vector (x-axis), the bisectrix of the H-C_n-H angle (y-axis), and the vector C_{n-1} to C_{n+1}(z-axis). From the symmetry argument, the tensor S is diagonal and S_{ZZ} illustrates the chain order

parameter. S_{zz} takes a value of unity if the average orientation is parallel to the bilayer normal (i.e., fully ordered), $-\frac{1}{2}$ if it is perpendicular to the normal, and zero if the system is completely disordered. S_{CH} is related to S_{CD} determine by the deuterium NMR experiment, where:

$$S_{CH} = S_{CD} = \frac{2}{3}S_{xx} + \frac{1}{3}S_{yy}, \quad (3.18)$$

where S_{xx} and S_{yy} are the order parameters in the x and y directions, respectively. In the case of a bilayer system, reduction of the length of the lipid chains correspond to decreasing density and increasing free volume fraction towards the middle bilayer[167]. The order parameter is indirectly related to the chain's tilt angle and trans-gauche distribution of chain dihedral. Simulations show that the number of gauche defects in membranes above the phase transition is smaller than in liquid alkanes. The fraction of gauche dihedrals decreases with decreasing temperature or increasing chain length[168].

3.5.4 Hydrogen bonding interaction

From the biological relevance, one of the main characteristic of sugars is the ability to participate in hydrogen bonds as both acceptor and donor. Each sugar has hydrophilic and hydrophobic region; the detailed interaction of hydrophilic part is under the control of the carbohydrate head group which can involve in hydrogen bonding, whereas the hydrophobic interaction is due to the branching of the alkyl chains. There is also a close relationship between the properties of biological membrane and the self-assembly of glycolipid dominated by this network of hydrogen bonds [104]. Thus, to determine quantitatively the hydrogen bonds is necessary to gain deep understanding on

the self-assembly behaviour. According to the classical chemical theory hydrogen has a valance of one but sometimes in some special cases it can behaves as bivalent[169]. That may be so, is the basis of the concept of hydrogen bonding: that between molecule A-H and a second atom, or a molecule, B, a particular force of attraction may operates Figure 3-9 shows a typical hydrogen bond. Although the bonding represented by the broken line is much weaker than the covalent bond A-H, such a formation does amount to assign some degree of bivalency to the hydrogen atom. Significant bonding will happen only when atoms A and B are sufficiently electronegative. Hydrogen bonding is probably favored when it is stereochemically possible for a lone-pair of electrons on B to point towards H. Ideally bonding is favored when the angle ψ is near to 180° . For weak bonds considerable deviations from 180° are often found [170]. Inter-molecular and intra-molecular hydrogen bond analysis was performed in each layer using the *ptraj* module in AMBER 12, and CARNAL (from AMBER7) respectively, by defining the O-O distance to be $\leq 3.5 \text{ \AA}$ and 4 \AA and the cut-off angle of 120° from linearity. Since the results of both O-O distances are almost similar we show only the results of O-O distance $\leq 3.5 \text{ \AA}$ here.

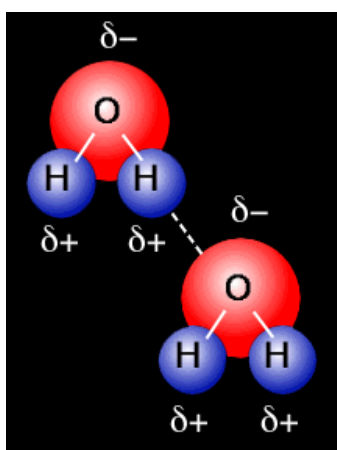


Figure 3-9: Typical hydrogen bonding in water molecule

3.5.5 Tilt angle and head group orientation

The tilt angle for the headgroup orientation was calculated based on the definition used by Tomasz[104]. The vector representing sugar headgroup is defined from C9-O4 (see Figure 3-6) and the orientation of the head group is defined by the angle between this vector and bilayer normal (along z axis). In this study we chose the above vector definition for the sugar headgroup to compare the results obtained by others and subsequently discern the effect of chain length[171] and branching[104] on the sugar head stereochemistry.

3.5.6 Lipid Dynamics in Anhydrous Bilayer

To examine the dynamic behaviour of sugar molecules in the bilayer system, we computed the mean square displacement (MSD) of the translational diffusion for the sugars at the lipid surface using the *ptraj* module in AMBER. Generally, the translational mobility of lipids in the bilayer membrane model is considered to be two-dimensional. The lateral diffusion of the molecules was evaluated from the mean square displacement (MSD) of their centre of mass in two-dimension i.e. $\langle \Delta r_{xy}(t) \rangle$, as a function of time.

$$\langle \Delta r_{xy}^2(t) \rangle = \left(\frac{1}{N} \sum_{i=1}^N [(\Delta x_i(t))^2 + (\Delta y_i(t))^2] \right). \quad (3.19)$$

where Δx_i and Δy_i represent the differences of the centre of mass (COM) for the i^{th} molecule between a time t and t_0 .

CHAPTER 4

RESULT AND DISCUSSION DFT STUDY OF GLUCOSE BASED GLYCOLIPID CROWN ETHERS AND THEIR COMPLEXES WITH ALKALI METAL CATIONS NA Na⁺AND K⁺

Journal of Molecular Modeling 2012, 18, 5041–5050

This chapter contains the results of the DFT study of glucose based glycolipid crown ethers and their complexes with alkali metal cations Na^+ and K^+ . We shall explain about the structures and coordination of these complexes. Meanwhile, there is the result of the investigation of the electronic structures, molecular conformations and the thermodynamic properties of glucose based glycolipid crown ethers and also their complexes with cations Na^+ and K^+ .

4.1 Structure of glycolipid crown ethers and their nucleophilicity

Figure 4-1 shows the optimized structures of different glycolipid crown ethers calculated at B3LYP/6-31G* level of DFT in ground state. From these structures we can see that the shape of crown ethers in G18C6 and the G16C5 is less deformed compared to the rest. The reactivity of the oxygen atoms around the crown ethers of the five molecules described using condensed Fukui function are given in Table 4.1. Positive values of the condensed Fukui function f_k^+ at site k mean that the particular atom is especially reactive to nucleophilic attacks. The higher the values of the f_k^+ on the site, the more reactive the particular site. From Table 4.1 we can see that not all the oxygen atoms in the crown ethers are reactive sites for nucleophilic attacks and the most reactive site of each molecule is located further away from the sugar ring, i.e., O31 in G15C5 and G18C6, O92 in G21C7, O24 in G16C5 and O80 in G19C6.

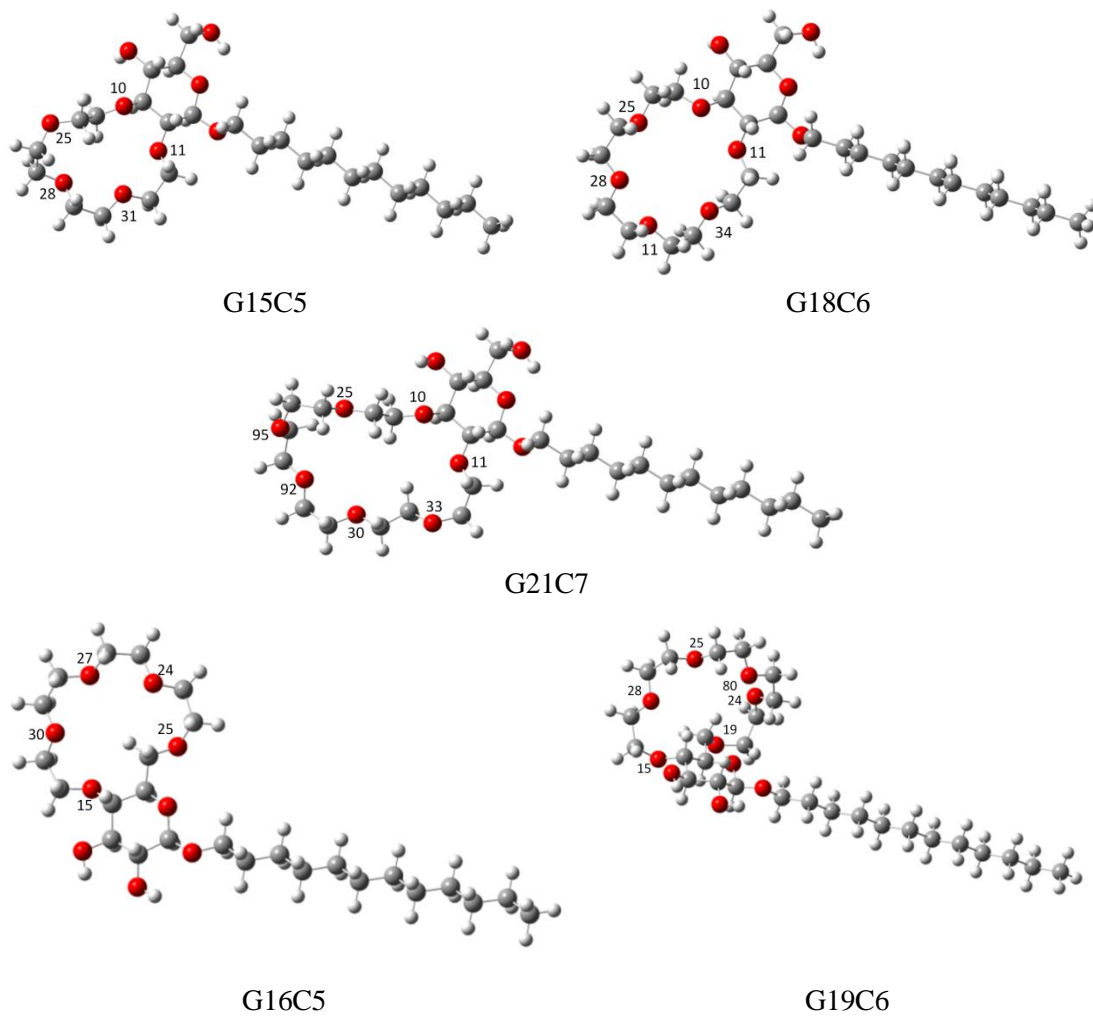


Figure 4-1: The optimized structures of the series of glycolipids crown ethers with the level of theory B3LYP/6-31G*. The oxygen atoms on the crown ethers are labelled

Table 4-1: Fukui function values for a nucleophilic for the different crown ethers

G15C5		G18C6		G21C7		G16C5		G19C6	
Atom	f_k^+	Atom	f_k^+	Atom	f_k^+	Atom	f_k^+		f_k^+
O3	-0.0073	O3	-0.0266	O3	0.0022	O4	-0.0122	O4	0.0008
O25	-0.0033	O25	0.0027	O25	-0.0096	O30	0.0061	O28	-0.0025
O28	0.0041	O28	0.0055	O95	-0.0116	O27	0.0055	O25	0.0041
O31	0.0121	O31	0.0060	O92	0.0128	O24	0.0079	O80	0.0124
O2	-0.0008	O34	0.0011	O30	0.0064	O6	0.0047	O24	-0.0011
		O2	-0.0041	O33	-0.0138			O6	-0.0070
				O2	0.0037				

Table 4-2, gives the overall electronic properties of the optimized structures in terms of HOMO-LUMO energies, energy gaps, ionization energies, electron affinity and nucleophilicity index. The energy gaps $\Delta\varepsilon_{LUMO-HOMO}$ calculated show that they are more or less the same for the five glycolipids crown ethers. However, among them G16C5 has the highest energy gap, suggesting that G16C5 is chemically the hardest. The ionization potential of the five molecules gives values that are also rather close to one another, while their electron affinities are more sensitive to the difference in size of crown ethers. Relatively, the largest glycolipids crown ether G21C7 has the highest ionization potential and electron affinity. However, G19C6 is the lowest in both quantities although it is not the smallest molecule. This is probably due to the optimized structure of the G19C6 being deformed in such a way that its cavity became as small as that of G15C5 (see Figure 4-1). In terms of global nucleophilicity, the relative nucleophilicity index N is $G19C6 > G15C5 > G16C5 > G18C6 > G21C7$.

Table 4-2: HOMO and LUMO energies ϵ_{HOMO} and ϵ_{LUMO} , energy gap $\Delta\epsilon_{LUMO-HOMO}$, ionization potential I , electron affinity A and nucleophilicity index N for the glycolipids crown ethers

Molecule	ϵ_{HOMO} (eV)	ϵ_{LUMO} (eV)	$\Delta\epsilon_{LUMO-HOMO}$ (eV)	I (eV)	A (eV)	N (eV)
G15C5	-6.372	1.559	7.889	7.385	-2.226	2.890
G18C6	-6.395	1.534	7.932	7.412	-1.713	2.247
G21C7	-6.565	1.397	7.962	7.534	-1.629	2.102
G16C5	-6.326	1.957	8.283	7.465	-1.906	2.425
G19C6	-6.032	1.881	7.913	7.346	-2.611	3.552

4.2 Geometrical structure of the complexes

The optimized structures of the complexes formed by the glycolipids crown ethers with the cations as given in Figure 4-2 and Figure 4-3. For each complex, the distances in Angstrom between the binding sites of oxygen atoms in the crown ethers to the cation Na^+ and K^+ have been worked out and presented in Table 4-2. From Figure 4-2, the optimized structure of complexes $Na^+/G15C5$ and $K^+/G15C5$ shows that the cations are located on the mean planes formed by the crown ethers, where K^+ is slightly further away from its crown ethers mean plane. This suggests that the cavity size for G15C5 is fit to accommodate Na^+ but too small for K^+ . For bigger sized crown ethers such as G18C6 and G21C7, the crown ethers cavity is big enough to encapsulate cation Na^+ by distorting their structure from being planar to form $Na^+/G18C6$ and $Na^+/G21C7$ complexes. The cavity size of G18C6 matches the size of cation K^+ , such that the cation is located on the mean plane of the crown ethers in the $K^+/G18C6$ complex.

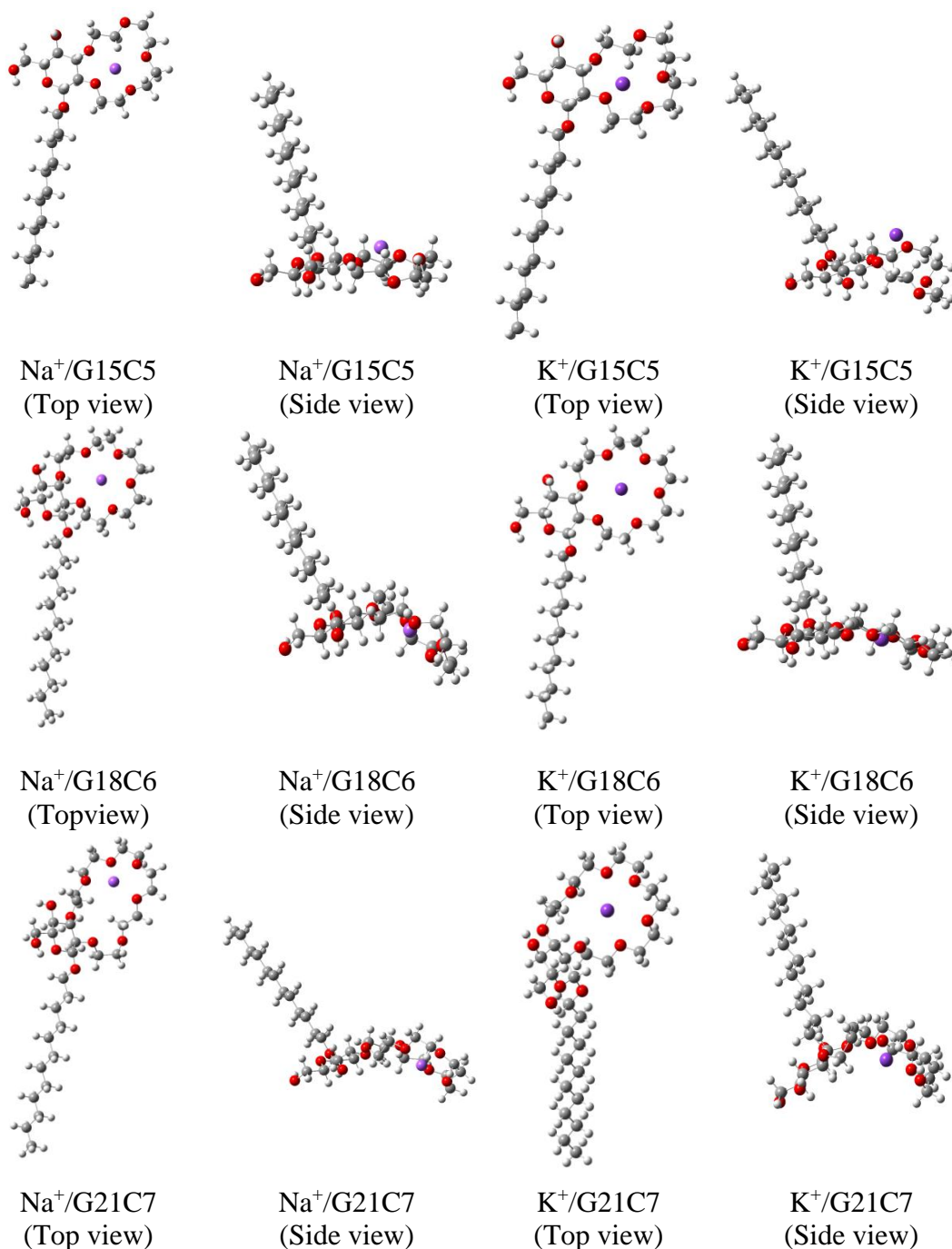


Figure 4-2: The optimized structures of complexes M⁺/G15C5, M⁺/G18C5 and M⁺/G21C5 at the level of theory B3LYP/6-31 G* where M⁺ represent the cations Na⁺ and K⁺

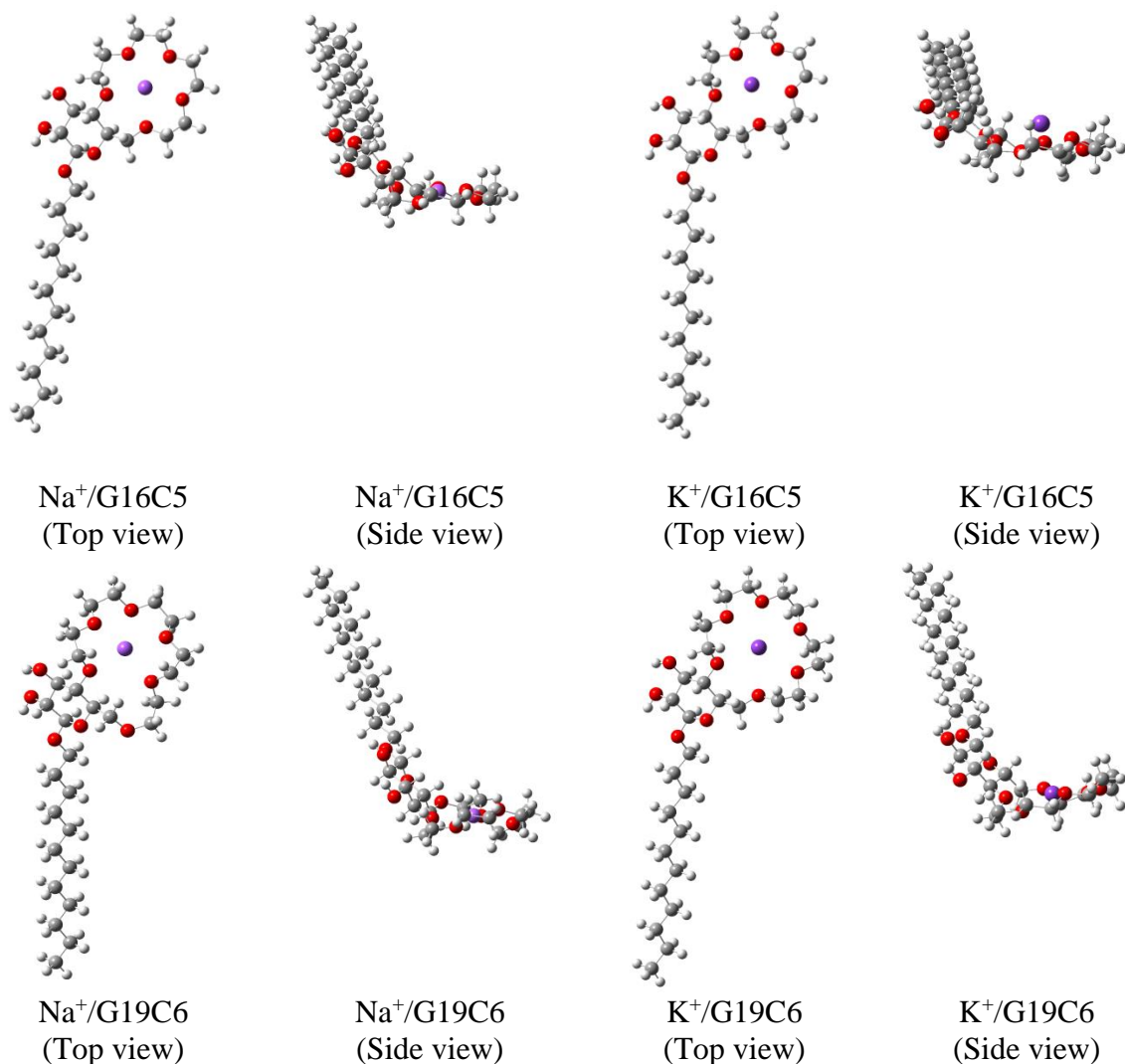


Figure 4-3: The optimized structures of complexes M⁺/G16C5 and M⁺/G18C5 at the level of theory B3LYP/6-31G* when M⁺ represents the cations Na⁺ and K⁺

Nevertheless, the cavity size of G21C7 is still bigger than that of cation K⁺. Therefore the crown ether of the structure of the complex K⁺/G21C7 is distorted from planar.

On the other hand, glycolipid crown ethers G16C5 and G19C6, which have a different linkage to the sugar ring from the other three, form complexes with the two cations Na⁺ and K⁺ with their crown ethers in planar structure (see Figure 4-3). G16C5 is shown to have the cavity size that matches well the size of the Na⁺ since its optimized structure in Figure 4-3 shows that the cation Na⁺ is located at the mean plane formed by

the crown ether. Meanwhile the cation K^+ in the $K^+/G16C5$ complex is located at slightly above the mean plane of its crown ethers. The crown ether of $G19C6$ is expected to have a bigger cavity size than the crown ether in $G15C5$, $G16C5$ and $G18C6$. Surprisingly the optimized structure of the $Na^+/G19C6$ complex in Figure 4-3 shows that the crown ether of $G19C6$ still forms a plane with its cation Na^+ in the middle of the plane. Comparing the top view of the structure of the $Na^+/K19C6$ complex with its side view, we can see that the mean plane is formed by five out of six of its oxygen binding sites. This can also be seen from the distribution of the Na^+-O distances for the complex in Table 4-2, where only five out of six oxygens are coordinated to the Na^+ . This makes up the five Na^+-O distances ranging from 2.367 Å to 2.507 Å, while a remaining Na^+-O distance of 3.568 Å. The crown ether of the $K^+/G19C6$ complex is also planar with the cation located in the middle of the plane. This time all six oxygen atoms are involved in forming the plane.

Table 4-3: Geometry parameters (GP) of different glycolipid crown ethers complexes with Na⁺ or K⁺

optimized at the level of theory B3LYP/6-31g*(Å)

	GP	G15C5	GP	G18C6	GP	G21C7	GP	G16C5	GP	G19C6
Na ⁺	rNa-O3	2.371	rNa-O3	3.487	rNa-O3	4.502	rNa-O4	2.365	rNa-O4	3.568
	rNa-O25	2.300	rNa-O25	2.628	rNa-O72	2.367	rNa-O30	2.321	rNa-O28	2.347
	rNa-O28	2.388	rNa-O28	2.451	rNa-O69	2.423	rNa-O27	2.409	rNa-O25	2.409
	rNa-O31	2.293	rNa-O31	2.572	rNa-O66	2.485	rNa-O24	2.357	rNa-O80	2.447
	rNa-O2	2.351	rNa-O34	2.471	rNa-O63	2.448	rNa-O6	2.341	rNa-O24	2.399
			rNa-O2	2.511	rNa-O60	2.388			rNa-O6	2.356
				rNa-O2	3.162					
K ⁺	rk-O3	2.732	rk-O3	2.796	rk-O3	3.852	rk-O4	2.701	rk-O4	2.802
	rk-O25	2.705	rk-O25	2.722	rk-O72	2.826	rk-O30	2.684	rk-O28	2.794
	rk-O28	2.756	rk-O28	2.851	rk-O69	2.811	rk-O27	2.768	rk-O25	2.854
	rk-O31	2.739	rk-O31	2.813	rk-O66	2.867	rk-O24	2.715	rk-O80	2.864
	rk-O2	2.938	rk-O34	2.724	rk-O63	2.887	rk-O6	2.704	rk-O24	2.755
			rk-O2	2.972	rk-O60	2.801			rk-O346	2.908
				rk-O2	2.874					

From the geometrical parameters in Table 4-3, in general, within a complex, the cation Na^+ can bind with the donor oxygen more closely than the K^+ . Moreover, the distribution of the cation-O distances within each complex in Table 4-3 implies that the majority of the complexes have all their oxygen atoms in the crown ethers coordinated to the cations. The complexes that do not have their oxygen atoms in crown ethers fully coordinated to the cations are $\text{Na}^+/\text{G18C6}$, $\text{Na}^+/\text{G19C6}$, $\text{Na}^+/\text{G21C7}$ and $\text{K}^+/\text{G21C7}$. In these four complexes, the oxygen atoms in the crown ether rings that are not coordinated to the cation are those from the glucose ring, namely, O3 for $\text{Na}^+/\text{G18C6}$, O4 for $\text{Na}^+/\text{G19C6}$, O2 and O3 for $\text{Na}^+/\text{G21C7}$, and O3 for $\text{K}^+/\text{G21C7}$ (see Table 4-3). Furthermore, from Table 4-3, one can see that the pairs of oxygen atoms in the crown ether rings that belong to the sugar rings are most likely to be further away from the cation compared to other oxygen atoms in the crown ether. This indicates that some constraint is imposed by the glucose ring on the O2 and O3 or O4 and O6, resulting in the latter to be less involved in the coordination with the cation compared to the other oxygen atoms from the crown ether. This restriction from the sugar ring can be seen in all the complexes except $\text{Na}^+/\text{G15C5}$, $\text{Na}^+/\text{G16C5}$ and $\text{K}^+/\text{G16C5}$. The cavity size in G15C5 and G16C5 fit for Na^+ cation. Therefore, the O- Na^+ coordination distances do not vary much in the cases of $\text{Na}^+/\text{G15C5}$ and $\text{Na}^+/\text{G16C}$. On the other hand, K^+ is too big to be fully contained within the cavities of G15C5 and G16C5 . For $\text{K}^+/\text{G15C5}$, the constrained sugar ring causes the O2 not to be as close to the cation as that of the O3, which has similar cation coordination distance as the other oxygen atoms. Meanwhile, both O4 and O6 in $\text{K}^+/\text{G16C5}$ have similar coordination distances to the cation. This is because, unlike the O2 in $\text{K}^+/\text{G15C5}$, the O6 has one C-C bond away from its sugar ring, therefore it has a greater flexibility. One way for the pairs of O2 and

O3 or O4 and O6 to minimize the coordination distances with the cation, is by reducing their dihedral angles O2-C-C-O3 for G15C5, G18C6 and G21C7, and O4-C-C-C for the G16C5 and G19C6, where the -C-C- belongs to the sugar rings (see Figure 4-1). This can be verified by comparing the dihedral angles of the free crown ethers and those of the complexes. The comparison is given in Table 4-4 and Table 4-5.

Table 4-4: Dihedral angle O2-C-C-O3 for optimized structures of molecules G15C5, G18C6 and G21C7 and their complexes with cations Na⁺ and K⁺

M(glycolipids crown ether)	Dihedral angles of O2-C-C-O3(°)		
	M	Complex Na ⁺ /M	Complex K ⁺ /M
G15C5	71.047	61.831	61.855
G18C6	74.375	61.141	64.613
G21C7	69.845	68.067	67.362

Table 4-5: Dihedral angle O4-C-C-C for optimized structures of molecules G16C5 and G19C6 and their complexes with cations Na⁺ and K⁺

M(glycolipids crown ether)	Dihedral angles of O4-C-C-C(°)		
	M	Complex Na ⁺ /M	Complex K ⁺ /M
G16C5	65.158	59.809	63.114
G19C6	68.018	62.116	58.571

From Table 4-4 and Table 4-5, we can see that these dihedral angles of the glycolipid crown ethers generally become smaller when the complexes are formed due to the interaction of the oxygen binding sites with the cation. As for the other dihedral angles O-C-C-O, around each crown ethers beside the O2-C-C-O3, the optimized structures in Figure 4-1 show that G18C6, G16C5 and G19C6 all have their dihedral angles of O-C-C-O in their crown ethers, either in the state of gauche⁺ ($0^\circ \leq \Phi < 120^\circ$) or gauche⁻ ($120^\circ \leq \Phi < 0^\circ$). Besides the gauche⁺ and gauche⁻ states, the G15C5 has one of its O-C-C-O in the trans state ($120^\circ \leq \Phi$ and $\Phi < -120^\circ$), while G21C7 has two trans states. However, all the trans states are transformed to the gauche states when the optimum coordination of oxygen atoms to the cations was considered.

4.3 Binding and exchange enthalpies and Gibbs free energies

The thermodynamics properties of the five molecules calculated at the B3LYP levels of theory using 6-31 G* basis set are given in Table 4-6. All the results in Table 4-6 have been corrected for their BSSE using the counterpoise method. The table shows that the binding energies, ΔE^b , of the molecules to smaller cation Na^+ are lower than the binding energies to the cation K^+ which are higher. This is consistent with previous experimental and theoretical studies of other crown ethers systems [172, 173] and cryptand [174] systems in gas phase which have shown that the binding energies are lower for small size alkali cations. This is because smaller size cations can have higher charge density and are able to bond with the coordination oxygens in crown ethers. Hence, Na^+ /glycolipid crown ethers complex are more stable than their counterpart complex of K^+ /glycolipid crown ethers, as shown in their binding enthalpies (Table 4-6). Furthermore, the feasibility of the complex formation is given by the Gibbs free energy. The Gibbs free energies calculated are negative values, indicating that all the complexes formation in gas phase considered here are chemically feasible.

Comparing the Na^+ complexes, our results show that the trend of the binding energies, binding enthalpies and the Gibbs free energies is in the order of G21C7 < G19C6 < G18C6 < G16C5 < G15C5. For the K^+ complexes, the trend is slightly different and is given as G21C7 < G18C6 < G19C6 < G16C5 < G15C5. From this comparison, we may deduce that, in gas phase, the glycolipid crown ether G21C7 is the most reactive in forming the stable complex with both the cations Na^+ and K^+ , while G15C5 is the least reactive. The sequence of the complex binding energies indicates that the higher the number of oxygen atoms in the crown ether ring, the more reactive is the formation of the complex with a cation. When comparing G16C5 and G15C5, both of which have the same number of oxygen atoms in their crown ether rings, suggests that

the additional flexibility in G16C5 makes it more reactive than G15C5 toward the formation of the complex. On the other hand, while Na⁺ is small compared to the cavities of G18C6 and G19C6, the additional flexibility of the latter, enable it to encapsulate Na⁺ better than the former. However, the formation of the K⁺/G18C6 complex is more reactive than that of K⁺/G19C6, which seems to suggest that the cavity of G18C6 fits better for K⁺ compared to the cavity of G19C6.

Table 4-6: The binding energies ΔE^b , binding enthalpies ΔH^b , and Gibbs free energies ΔG^b , in the gas phase for the complexes at 298K

Molecule	Metal cation	ΔE^b (kcal/mol)	ΔH^b (kcal/mol)	ΔG^b (kcal/mol)
G15C5	Na ⁺	-79.4503	-80.0433	-69.2432
	K ⁺	-50.3658	-50.9582	-41.0366
G18C6	Na ⁺	-83.6138	-84.2074	-74.8544
	K ⁺	-69.0568	-69.6498	-59.9580
G21C7	Na ⁺	-90.3181	-90.9118	-80.0107
	K ⁺	-69.3405	-69.9335	-59.1654
G16C5	Na ⁺	-81.7037	-82.2967	-73.0679
	K ⁺	-52.8257	-53.4180	-44.3599
G19C6	Na ⁺	-84.0154	-84.6084	-75.9036
	K ⁺	-64.4974	-65.0897	-56.7369

To further understand the selectivity of these molecules toward Na⁺ we calculated the exchange enthalpies and exchange free energy given by the chemical reaction of:



The results are tabulated in Table 4-7. The exchange enthalpies and Gibbs free energies for these molecules can be arranged in the following order G15C5 > G16C5 > G21C7 > G19C6 > G18C6. The exchange enthalpies for G15C5 and G16C5 are significantly higher than G21C6, G19C7 and G18C6, which implies two of the former show much higher selectivity toward Na⁺ against K⁺. Although these results were obtained based on the gas phase condition, it is qualitatively similar to the experimental cation selectivity performed in an aqueous solution with an equimolar ratio of cations Na⁺ and K⁺[45],

where the measurements were done using electrospray ionization method. The significantly higher ion selectivity of the two compounds G16C5 and G15C5 to the Na⁺ over K⁺ than the others was also confirmed by the experiment [45]. However, G21C7 was shown experimentally to have a slightly higher affinity toward K⁺, in contradiction to the theoretical result obtained in the gas phase. Nevertheless, the selectivity patterns of the five molecules over Na⁺ and K⁺ were similar to those of crown ethers with a similar number of oxygen atoms in the crown in gas phase as measured in the experiment [175].

Table 4-7: Exchange enthalpies ΔH and Gibbs free energies ΔG for the cation exchange in the gas phase at 298 K

Molecule	$\Delta H(\text{kcal/mol})$	$\Delta G(\text{kcal/mol})$
G15C5	29.0851	28.2066
G18C6	14.5576	14.8965
G21C7	20.9783	20.8453
G16C5	28.8786	28.7080
G19C6	19.5187	19.1667

It is well known that the preference of the crown ether binding with a cation in the gas phase would shift toward a bigger cation in the aqueous solution [176, 177]. The crown ether G18C6 is known to bond more strongly with Na⁺ than K⁺ in the gas phase, while in the aqueous solution it shifts toward a stronger bond with K⁺ than Na⁺. Two reasons have been suggested for this change of ion selectivity [92, 173, 178]. Firstly, the stronger solvation effect on the smaller cation Na⁺ than K⁺, to some extent, make the complexation of K⁺/G18C6 preferable toward Na⁺/G18C6. Secondly the stronger solvation of the complexes with a bigger cation K⁺ adds to the extra stability of the solvated complexes of K⁺/G18C6 compared to Na⁺/G18C6. On the other hand, the glucose based crown ethers of G18C6 equivalents, studied by Bako *et al.* [179] in an experiment, shows that it prefers Na⁺ over K⁺ in an aqueous solution. The same effects on the glycolipid crown ethers can be expected, thus in aqueous condition these prefer

Na⁺ over K⁺, especially G18C6 and G19C6, which are the equivalent of G18C6. The solvation effect on the glycolipid crown ethers is undoubtedly interesting to the behavior of these molecules in aqueous solution as well as when they are dissolved in other solvents. This is currently under investigation and will be reported in the near future.

CHAPTER 5

**RESULT AND DISCUSSION:
ATOMISTIC SIMULATION STUDIES OF THE
 α/β GLUCOSIDE AND GALACTOSIDE IN
ANHYDROUS BILAYERS: EFFECT OF THE
ANOMERIC AND EPIMERIC CONFIGURATIONS**

Journal of Molecular Modeling 2014

In this chapter we shall report the result of the full atomistic molecular dynamics simulation studies of four different bilayer systems which performed using a set of glycosides namely n-octyl- β -D-glucopyranoside (β -C₈Glc), n-octyl- α -D-glucopyranoside (α -C₈Glc), n-octyl- β -D-galactopyranoside (β -C₈Gal) and n-octyl- α -D-galactopyranoside (α -C₈Gal). The present objective is to find molecular substantiation on the likely relationship between two pairs of liner glycolipids, namely, α/β -octyl-galactosides (α/β -C₈Gal) and α/β octyl-glucosides (α/β -C₈Glc) using computer simulation method in the thermotropic liquid crystal phase.

5.1 Local density profiles (LDPs)

The 20ns block averages of the local density profiles for four systems (α/β -C₈Gal and α/β -C₈Glc) over the last 160 ns are given in Figure 5-1. The LDPs show the bilayers do not break or fluctuate far from the equilibrium values and there are only minor differences between different block averages during the simulations. The expected microphase separation of the hydrophilic and the hydrophobic regions is demonstrated by the maximum and minimum density values along the bilayer normal in this figure. This implies that throughout the simulation the structures are intact. The LDPs of the four systems (α/β -C₈Gal and α/β -C₈Glc) are qualitatively similar in general. However, the d -spacings (or precisely the Luzzati's thickness[180]) are different, implying that these bilayers have slightly different packing arrangements which affect their melting points [181]. The experimental bilayer spacing at 25°C for β -C₈Gal is 25.1 Å, while at 90°C this value is 25.8 Å (Table 5-1), which is slightly less than the simulated value of 27.5 Å at 90°C. Similarly, for β -C₈Glc the simulated value of 27.5 Å is slightly more than the experimentally determined X-ray d -spacing of 25.6 Å and 25.3 Å at 70°C and 105°C respectively [182]. Generally the present data for d -spacings are accord with those from the X-ray measurements for these phases within

less than 10%. This percentage difference is not too dissimilar from those found in other simulation studies of disaccharides in thermotropic phase when compared with the experimental data[106, 108, 183]In addition, it seems for β -C8Glc/C8Gal increasing the temperature does not change the thickness very much. Table5-1also shows that the bilayer spacings for α -anomers are smaller than those of the β -anomers, which imply the former pack more tightly compared to the latter. Comparing the d -spacing of the quartets (α/β -C8Gal and α/β -C8Glc) reveals that the anomeric effect is more dominant than the epimeric effect.

Table5-1: d -spacing for β -C8Gal in L_C phase, α -C8Gal and α/β -C8Glc in L_α phase and their average surface areas at the interface per lipid from160 ns simulations and the corresponding X-ray experimental data.

Lipid	Simulation at 90°C		Experimental data from X-ray	
	d -spacing/Å	Area/head group(Å ²)	d -spacing/Å	Area/head group/Å ²
β -C8Gal	27.5 ± 0.4 (L_C)	32.2 ± 0.4	25.1/25.8 (at 25/90°C)[182]	34.49 ^a
β -C8Glc	27.6 ± 0.3 (L_α)	32.3 ± 0.3	25.6/25.3 (at 70/105°C)[182]	36.1 [184, 185]
α -C8Glc	24.4 ± 0.2 (L_α)	36.0 ± 0.3	23.3 (at 75 °C)[186]	39.1 [187]1
α -C8Gal	25.4 ± 0.3 (L_α)	35.1 ± 0.4	NA	-

^acalculated from the data of ref. [188]

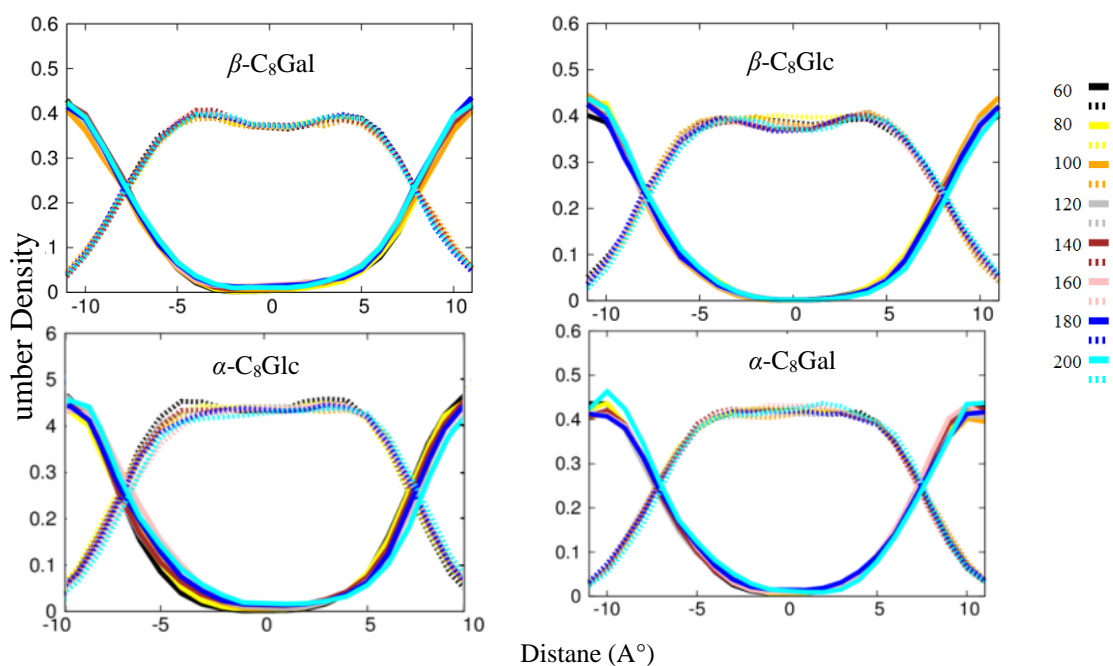


Figure 5-1:(A) Local density profiles: averages over block of 20 ns from 40 ns to 200 ns for (a) α -C8Gal, (b) β -C8Glc, (c) α -C8Glcand (d) β -C8Gal. The solid lines are for head group and the dotted lines are for alkyl chain. Each colored line in the legend shows the ldp of different 20 ns block averages spread over the 160 ns production stage.

5.2 Area at the interface per sugar head

The average surface area at the interface per sugar head group over 160 ns dynamics runs for the four selected glycosides namely α/β -C8Gal and α/β -C8Glc, are given in Table 5-1. This data shows that the areas for α -C8Glc and α -C8Gal with the values of 36.0 and 35.1 \AA^2 respectively are greater than those of β -C8Glc and β -C8Gal by 10-12%. These results show the anomeric factor is important in controlling this property in the same manner as in the case of d -spacing. Thus, both thickness and interfacial area per head group are less sensitive to the C4 epimeric effect. According to the phase diagrams, both α/β -C8Glc and α -C8Gal are in the L_α phase. Therefore, chains within this phase are more fluid. In contrast, at this temperature β -C8Gal is in the L_c phase but very close to the transition into the L_α phase. Hence, it was observed the β -C8Gal bilayer has the least area per head group (32.2 ± 0.4) \AA^2 . Our results show that α -anomers have higher surface area at the interface and lower densities than β -anomers.

5.3 Hydrogen bonds analysis

For a sugar-based surfactant system in a dry state, the sugar heads interact strongly with each other to stabilize the bilayer. This interaction originates mainly from the hydrogen bonds between sugar hydroxyl groups which makes sugar surfactants very fascinating in terms of their solid state behaviour [189]. In addition, detailed sugar stereochemistry could generate hydrophobic or apolar surface on the sugar moiety giving its amphoteric character, which is important for molecular recognition [190]. Glycolipid system has the ability to participate in hydrogen bonding as both donor and acceptors, unlike phosphatidylcholines, which can act only as an acceptor [104, 191]. Each sugar head group in the bilayer system can be involved in two types of hydrogen bonds: inter- and intra-molecular hydrogen bonds. The results of hydrogen bonds for four sugar surfactants (α/β -C8Glc and α/β -C8Gal) are tabulated in Table 5-2, β -C8Gal has more affinity to be involved in both inter- (3.21) and intra-molecular (1.71)

hydrogen bonds compared to β -C8Glc whose values are 3.06 and 1.12 respectively. In the former the hydroxyl group at C4 is oriented axially[182]. On the other hand, the inter-molecular hydrogen bond for α -C8Gal is 2.37 while that for α -C8Glc is 3.10. But a reverse trend is observed for intra-molecular hydrogen bonds with the values of 1.31 and 1.71 for α -C8Glc and α -C8Gal respectively. Table 2 also shows that, the trend for the total hydrogen bonds of the four compounds is the same as that of the inter-molecular hydrogen bonds, i.e. β -C8Gal > α -C8Glc > β -C8Glc > α -C8Gal. This trend is also similar to the clearing temperatures of the four compounds, both from experimental and calculated based on the intermolecular hydrogen bond. In Table 5-3, the calculated clearing temperature assumes β -C8Glc is the reference compound. In the Supplementary, we have included all the calculated clearing temperatures, using different compounds as a reference. These predicted clearing temperatures are consistent with each other within less than 3%, except when using α -C8Gal as a reference, where the difference is about 10%. Thus, it supports the previous proposal that inter-molecular hydrogen bonds contribute to the thermal stability of the bilayer assembly [192].

Moreover, the axially orientated hydroxyl group at C4 makes α/β -C8Gal more capable of being involved in the intra-molecular hydrogen bonds than α/β -C8Glc. Incidentally, these results agree with those reported by Mosapouret *al.*, [193] who had performed DFT calculations and analysed them using atoms in molecules approach (AIM) and natural bond orbital analysis (NBO). The AIM results proved that for β -C8Glc there is one intra-molecular hydrogen bond (HO6...O4), while for β -C8Gal, there are two extra bonds (HO6...O4 and HO6...O3). In fact the inter-molecular hydrogen bond trend we observed here for the four glycosides agree with the same trend (intra-layer hydrogen bond) from the previous simulation [107]. Of course quantitatively, the detailed numbers differ since their systems were simulated at 300 K, for 5ns simulation

run. The total lipid-lipid hydrogen bonds for these glycosides are about 40-50% higher than those of 1,2-di-*O*-palmitoyl-3-*O*- β -D-C8galactosyl-*sn*-glycerol (DP-C8GALA) and 1,2-di-*O*-palmitoyl-3-*O*- β -D-glucosyl-*sn*-glycerol (DP-GLUC) [104]. Lower values of lipid-lipid inter-molecular hydrogen bonds for these glyco-glycerol lipids are expected since the simulations were conducted in the lyotropic phase, where there was a variety of hydrogen bonds involving lipid-lipid, lipid-water, water-bridge and H-bonded water [104]. However, the trend for hydrogen bonds (of DP-C8GALA versus DP-GLUC) agrees with the present results of galactosides versus glucosides. A similar pattern of dependency was also observed in the micellar (L_1) systems of for β -C8Gal and β -C8Glc, with the total number of inter head group hydrogen bonds at 2.14 and 1.8 respectively [106].

The role of polar interaction of the monosaccharide head group is important to stabilize the self-assembly. In theory, the maximum number of hydrogen bonds which a monosaccharide can make is 16, corresponding to 6 oxygen atoms able to accept 2 hydrogen bonds and 4 polar hydrogen atoms able to donate hydrogen bond. Simulation result of the bilayer system shows the values are less than 16 and these are 4.92, 4.41, 4.18 and 4.08 for β -C8Gal, α -C8Glc, β -C8Glc and α -C8Gal respectively. Orientation constraint of hydroxyl groups and the steric effect in the bulk environment are some of the reasons, which cause the decrease of hydrogen bonding ability of the sugar head group [108]. It is interesting to calculate the distribution of these hydrogen bonds over the different OHs sites on the sugar moiety. Figure 5-2 shows the results of the individual donor and acceptor contributions to hydrogen bonding. A closer look into this in Figure 5-2 reveals that the interaction scheme of inter-lipid hydrogen bonding are dominated by oxygen O2 and O6 in all four compounds (α/β -C8Gal and α/β -C8Glc), which suggests greater availability of O2 and O6 to accept inter-head group hydrogen bonds. The low interaction for O1 and O5 is expected based on the missing hydrogen

donor ability due to the lack of a proton acceptor. In general O2 contributes almost 45% more in hydrogen bonding compared to O3 in all four compounds, but the order and trend of hydrogen bond of the quartet on both sites are almost the same (see Figure, 5-2). Specifically, the trend for the hydrogen bond distribution on O2 and O3 of the four compounds is α -C8Gal > β -C8Gal > β -C8Glc > α -C8Glc. But this trend is slightly different for the O6 site, which is α -C8Glc > α -C8Gal > β -C8Glc > β -C8Gal. Thus, on O2 and O3, the epimeric effect is more dominant, while on O6 the anomeric effect is more dominant. The hydrogen bonding trend on the O4 site is β -C8Gal > α -C8Glc > β -C8Glc > α -C8Gal, which is similar to the overall trend for hydrogen bonding. Even though β -C8Gal and α -C8Glc are anomerically different, the hydrogen bonds on the O4 site of the former and the O6 site of the latter contribute nearly 80% of the total hydrogen bonds. The axial orientation of OH on the O4 epimer in β -C8Gal causes the increase in the capacity of donor and acceptor of this compound. On the other hand, for α -C8Glc the exocyclic group at C6 position extends out to form a hydrogen bond with neighbouring lipids. These hydrogen bond interactions may be attributed to the high clearing temperatures of 127°C and 116°C for β -C8Gal and α -C8Glc respectively.

Table 5-2: Total number of hydrogen bonds per sugar for α -C8Glc, β -C8Glc, α -C8Gal and β -C8Gal comprised of inter-molecular and intra-molecular hydrogen bonds.

Mol/HB	β -C8Gal	α -C8Glc	β -C8Glc	α -C8Gal	Trend
Inter-mol	3.21	3.10	3.06	2.37	β -C8Gal > α -C8Glc > β -C8Glc > α -C8Gal
Intra-mol	1.71	1.31	1.12	1.71	α -C8Gal > β -C8Gal > α -C8Glc > β -C8Glc
Total	4.92	4.41	4.18	4.08	β -C8Gal > α -C8Glc > β -C8Glc > α -C8Gal
Exp. Clearing point °C	127[182]	116[182]	107[182]	98[10]	β -C8Gal > α -C8Glc > β -C8Glc > α -C8Gal
Calc. Clearing point °C	132	115	107	72	β -C8Gal > α -C8Glc > β -C8Glc > α -C8Gal
Exp. Melting point °C	96[182]	69[182]	69[182]	40[192]	
From other literatures					
Intra-layer [107]27(°C)	2.9	2.77	2.70	2.43	β -C8Gal > α -C8Glc > β -C8Glc > α -C8Gal
Inter-mol[104]70(°C)	1.63 ^a	-	1.28 ^a	-	DP-C8GALA > DP-GLUC
Inter-mol[106]	2.14 ^b	-	1.8 ^b	-	β -C8Gal > β -C8Glc

^a Calculation is in lyotropic phase, ^b Calculation is in micellar phase

Table 5-3: calculated clearing temperatures, using different compounds as a reference

	Exp. T(°C)	Exp. T(K)	inter-mol-HB	Calc. T (K) ¹	% error	Calc. T(°C)		Calc. T (K) ²	% error	Calc. T(°C)		Calc. T (K) ³	% error	Calc. T(°C)		Calc. T (K) ⁴	% error	Calc. T(°C)
<i>α</i> -Gal	98	371	2.74	344.77	7.07	71.77		340.37	8.26	67.37		346.06	6.72	73.06		371.00	0.00	98.00
<i>α</i> -Glc	116	389	3.08	387.55	0.37	114.55		382.61	1.64	109.61		389.00	0.00	116.00		417.04	7.21	144.04
<i>β</i> -Gal	127	400	3.22	405.17	-1.29	132.17		400.00	0.00	127.00		406.68	-1.67	133.68		435.99	9.00	162.99
<i>β</i> -Glc	107	380	3.02	380.00	0.00	107.00		375.16	1.27	102.16		381.42	-0.37	108.42		408.91	7.61	135.91

1. *β*-Glc selected as reference.
2. *β*-Gal selected as reference.
3. *α*-Glc selected as reference.
4. *α*-Gal selected as reference.

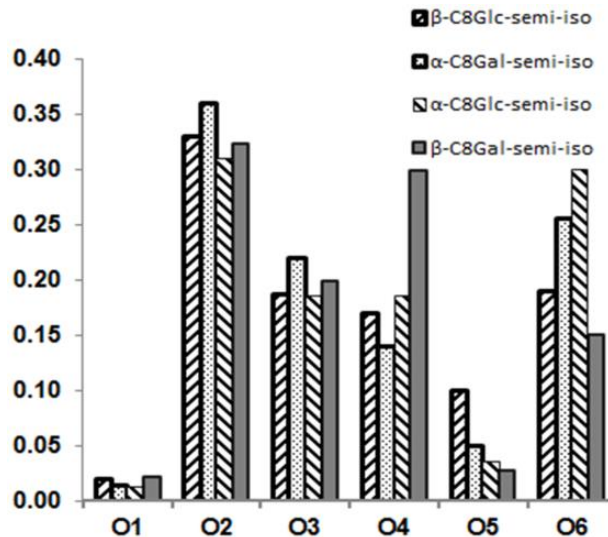


Figure 5-2: Inter-molecular hydrogen bond distribution over different oxygen locations (see Fig. 2) for β -C8Glc (\square), α -C8Gal (\square), α -C8Glc (\square), and β -C8Gal (\square)

5.4 Head group orientation

Figure 5.3 shows the distribution of the angle between the C9-O4 vector and the bilayer normal [104]. From the non-Gaussian plots, we observe the population maxima occur at 28° and 36° for β -anomeric pairs, β -C8Gal and β -C8Glc respectively; whereas, for the α -anomeric pairs, α -C8Glc and α -C8Gal, these occur at 42° and 40° respectively. We notice that β -C8Gal, which is in the L_C phase, is tilting significantly less compared to the other isomers, which are in the fluid L_α . As expected, β -anomers are tilting less than α -anomers for the equatorially linked anomeric carbon to the glycosidic oxygen. The angle distribution profiles for β -C8Glc and β -C8Gal from the current study are similar to those from the published work by Roget *al.* [104], for β -anomers of DP-C8GALA and DP-GLUC with di-palmitic chains in L_α lyotropic phase. This similarity indicates that the orientation of sugar head group is not much affected by the branching and chain length. Moreover, in these cases the maxima occurred at about 38° , which is

not too different from our measurement for the β -C8Glc (36°), in the anhydrous L_α , but is strikingly different from the dry L_C phase of β -C8Gal (28°).

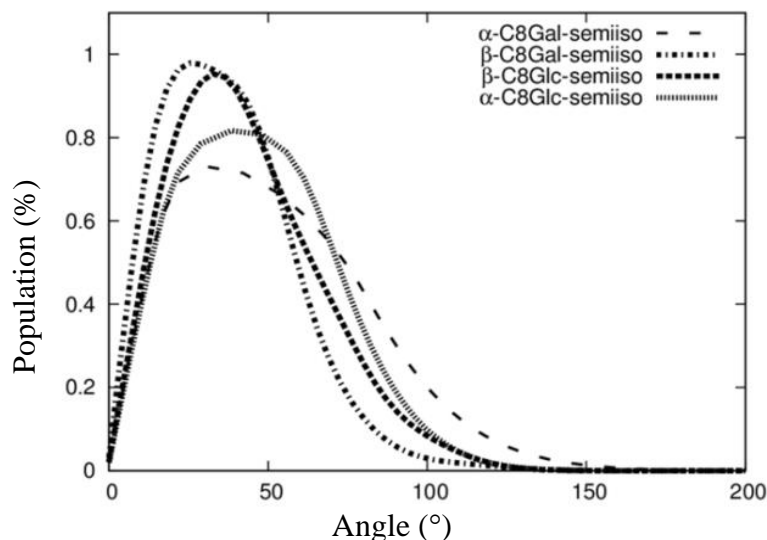


Figure 5-3: Distribution of angles between C9-O4 vector and bilayer normal in α -C8Gal (- -), β -C8Gal (5-...), β -C8Glc(-.-) and α -C8Glc (.....) bilayers

5.5 Order parameter

Chain ordering in the bilayer is an interesting property used to determine the type of phase of the lipid assemblies [194]. Experimentally, $^2\text{H-NMR}$ (deuterium Nuclear Magnetic Resonance) measurement is used to determine the C-D bond order of the deuterated chain [195]. But, in a simulation, the order parameter is calculated using C-H bond and the Saupe ordering tensor, and this is correlated with, the $-\langle S_{CD} \rangle$ [104]. Figure 5.4 shows the $-\langle S_{CD} \rangle$ as a function of the methylene carbon position [196, 197] for the four compounds. In general, the plot shows the bond (C-H) order parameter decreasing from C9 to C14 for the quartet α/β -C8Gal and α/β -C8Glc. The farther the position of the carbon from glycosidic bond, the less the order becomes; hence the increase in the flexibility of the chain. Van Buuren *et al.* also found the same diminishing chain ordering behaviour for α/β -C10Glc in lyotropic systems [198]. It is interesting to note that the chain order parameters profiles (which are in the hydrophilic

region) can be differentiated for the four compounds despite a diminutive difference in the head group stereochemistry. The two β compounds (β -C8Gal and β -C8Glc) have higher chain order parameter profiles compared to α compound (α -C8Gal and α -C8Glc). Except for β -C8Gal which is in the L_c phase, all other lipids are in the liquid crystalline, $L\alpha$ phase. This leads to the expectation that the bond order parameter of β -C8Gal will be higher compared to that of the other three lipids. This is because in the $L\alpha$ the chains are expected to be more disordered compared to those in the L_c phase. However, we observed a contradicting behaviour, where β -C8Gal which is in the L_c phase, has a lower $-\langle S_{CD} \rangle$ profile than does β -C8Glc. This could be related to the higher hydrogen bonding interaction at C4 (see Figure 5-2, O4) compare to those for the other lipids. The melting temperature of β -C8Gal is $96 \pm (5-8)^\circ\text{C}$ [182] which is very close to the simulated temperature 90°C . This observation may be justified from the thermal fluctuation viewpoint according to Sakya *et al.*,[182] the high hydrogen bonding at the O4 position constrain the head group, but allows the chain to fluctuate more, thus lowering the order parameter in the L_c phase of β -C8Gal. Meanwhile, from Figure 5-4 a higher degree of chain ordering is also related to a lower tilt angle of the chains. When the tilt angle is high, less chain packing is expected. Therefore, β -C8Glc and β -C8Gal with the smaller tilt angles have higher chain ordering.

Comparing the α/β anomers, α -anomers have lower order parameter compared to β -anomers. α -anomers give a bent molecular shape especially at the sugar head group to carbon chain and the arrangement in bilayer ordering of these molecules causes the alkyl chains to pack less densely. Similar results were observed for the n-decyl- α -D-glucopyranoside and n-decyl- β -D-glucopyranoside monolayers at the water-decane inter-face [198] which suggests that increased tilt of the α -glucose head groups leads to poorer packing of the decyl chains.

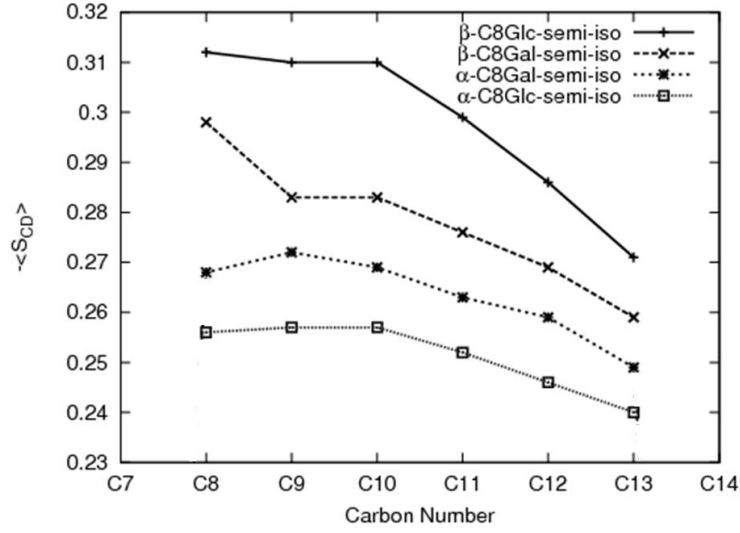


Figure (5.4) The average bond order parameters of C-H along the chain, $-\langle S_{CD} \rangle$, for β -C8Gal (*), β -C8Glc (□), α -C8Gal (+), and α -C8Glc (x), Connecting lines drawn only as a guide. The error in these values is less than 4%.

5.6 Lipid Dynamics in Anhydrous Bilayer

The Einstein relation (also known as Einstein–Smoluchowski relation) of diffusion coefficient and mobility, for a typical system, where the particles motion is Brownian, should be linear[199]. For this diffusion process, the mean square displacement (MSD) is linear in time with a constant slope representing the diffusion coefficient D . Deviation from this linearity indicates anomalous behaviour, which can be categorized sub- or super-diffusion, and the MSD can be more generally defined as:

$$g\langle \Delta r^2(t) \rangle = Dt^\alpha \text{ with } 0 < \alpha < 1 \quad (5.1)$$

$$\lg \langle \Delta r^2(t) \rangle = \lg D + \alpha \lg t \quad (5.2)$$

where t denotes the time axis, and D is the diffusion coefficient which has the dimensionality of $\text{cm}^2/\text{sec}^\alpha$ [200]. The double logarithmic regression enables the determination of the power α of the diffusion law. When Einstein relation is satisfied α

equals to one. On the other hand, when α is not equal to 1, the system experiences either a sub- ($\alpha < 1$) or super-diffusion ($\alpha > 1$). In *Nature*, sub-diffusion is necessary for local interactions in cells,[201]even though it slows down long-distance diffusional surface-bulk exchange[202]. For instance, the localization of objects such as chromosomes or membrane channels and the formation and dynamics of membrane domains, all depend on the magnitude of the exponent α .

Table 5-4: The anomalous diffusion exponent, α and diffusion coefficient, D [$\times 10^{-8}$ m²/s] for α/β -C8Gal and α/β -C8Glc (40-200 ns) in dry state.

Lipid	Exponent α	Calc. D [$\times 10^{-9}$ cm ² /s ^{α}]	Cis/Trans- epimer/anomer
β -C8Gal	0.7 \pm (0.3%)	9.0 \pm 0.3	Cis
β -C8Glc	0.6 \pm (0.2%)	6.4 \pm 0.4	Trans
α -C8Gal	0.5 \pm (0.3%)	6.2 \pm 0.3	Trans
α -C8Glc	0.5 \pm (0.4%)	2.0 \pm 0.8	Cis
	Exp. D [$\times 10^{-8}$ cm ² /s]	Calc. D [$\times 10^{-8}$ cm ² /s]	
DPhPC	18.1 \pm 5.6 [70,71]	13.7 \pm 0.5 [70]	In water
DPPD	20.7 \pm 2.8[70,71]	35.3 \pm 0.6 [70]	In water

In order to evaluate the lateral diffusion process in our bilayer systems, the double log MSD was calculated as a function of time (see Figure 5-5), which displays the anomalous diffusion characteristics of the four lipid systems. This is based on equation(5.2), which describes the diffusion for both normal and anomalous systems [72]. This linear graph gives the exponent α and the diffusion coefficient, D are given in Table (5-4). The observed sub-diffusive behavior of these lipids is reasonable and is attributed to the unique structural complexity of the sugar head group, consistent with those observed for phospholipids in the liquid disordered, liquid ordered and gel phases [200]. From Table (5-4) we note also that the trans-epimer/anomer pair (β -C8Glc and α -C8Gal) in the L_α phase, have similar values of diffusion coefficients 6.4 and 6.2 ($\times 10^{-9}$ cm²/s ^{α}) respectively. The diffusion of the trans-epimer/anomer pair is similar to the gel phase of phospholipids bilayer membrane[200]. In contrast the cis-epimer/anomer pair has strikingly different values of diffusion coefficient, i.e. 9.0×10^{-9} cm²/s ^{α} for β -C8Gal

(L_C phase), and $2.0 \times 10^{-9} \text{ cm}^2/\text{s}^{\alpha}$ for α -C8Glc (L _{α} phase). These results may be understood from considering the thermal stability of these glycosides assembly with respect to their molecular structures. The thermal stability of amphiphilic liquid crystal is due to the hydrogen bond networks and the ability to store energy without disrupting the assembly. In the chain region, most of the energy will be stored in the vibrations of the alkyl chains [182]. Figure 5-6 shows the packing density and hydrogen bonding for α/β -anomeric pairs. The more linear shape of β -glycosides leads to a significantly more dense packing of the alkyl tails compared to the bent shaped of the α -anomers. The former has less hydrophobic area for the chains to vibrate, and so they eventually push each other apart, hence greater diffusion is expected. On the other hand, the chain groups of the α -anomers vibrate more due to the extra area in the chain region, and so the L _{α} phase is stable to higher temperatures [182].

In Table (5-4) we have included some experimental and simulation results of DPhPC and DPPC in the lyotropic phase for comparison. As expected, these lyotropic systems has larger diffusion coefficient compare to our dry systems. We have included some experimental and simulation results of DPhPC and DPPC in the lyotropic phase for comparison. As expected, these lyotropic systems has larger diffusion coefficient compare to our dry systems.

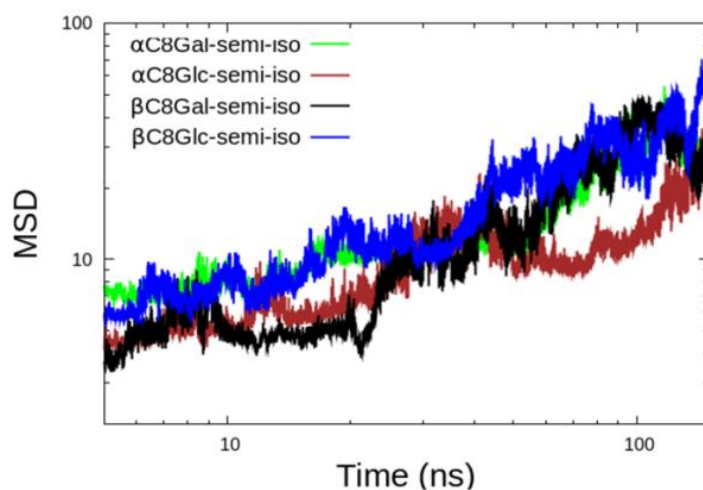


Figure 5- 5:Logarithmic scale of diffusion in xy direction for 160 ns for α/β -C8Gal and α/β -C8Glc.

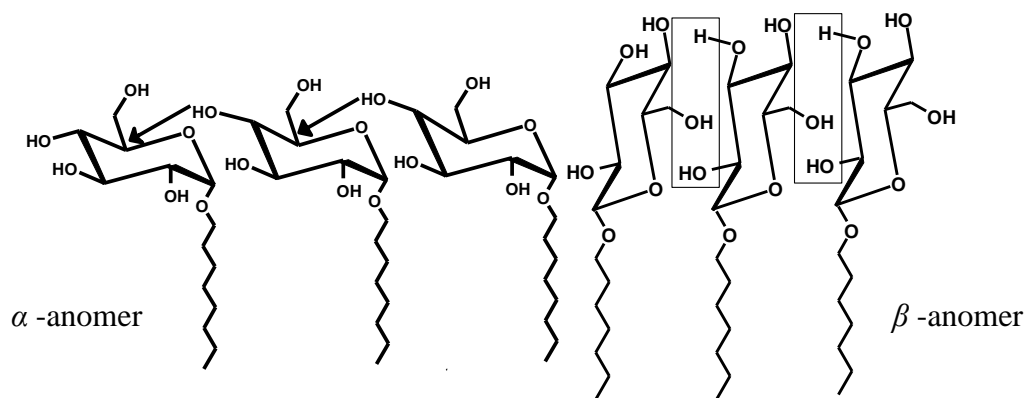


Figure (5-6) Packing density and hydrogen bonding for α/β -anomeric pairs

CHAPTER 6

RESULT AND DISCUSSION: MOLECULAR DYNAMICS SIMULATION OF LYOTROPIC REVERSE HEXAGONAL (H_{II}) OF GUERBET BRANCHED CHAIN *B*- D-GLUCOSIDE

Journal of Physical Chemistry Chemical Physics, 2014, 116, 324

6.1 Structure of the reverse hexagonal H_{II}

The final configurations from the simulations of the two systems with different concentrations are given in Figure 6-1, which show the stable hexagonal arrangements, with box dimensions of 11.8nm×6.9nm×4.8nm and 11.8nm×6.9nm×4.8nm, respectively. The stability of the simulation systems over the course of the simulation time was checked by monitoring the profile of the lattice parameter (i.e. average distance between two cylinders) and the radial density over time. Here, the distance between two cylinders is defined as a two dimensional (i.e. X and Y axes) distance between the centres of mass of the two water columns (the lattice parameter). For each time frame, the lattice parameter between two neighboring cylinders is evaluated from all the possible pairs of neighbors from the six cylinders. The time averaged lattice parameters are tabulated in Table 6-1, which is in relatively good agreement with the experimental measurements.

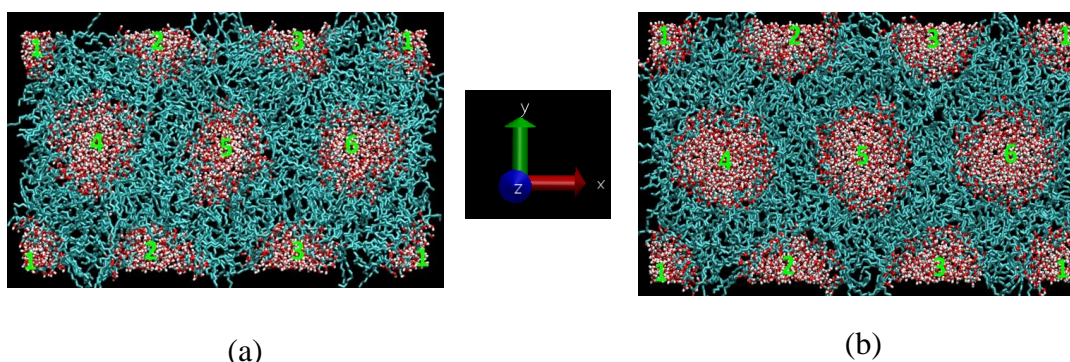


Figure 6-1: The Configurations of the H_{II} phase after 50 ns for C₈C₁₂β-D-Glc system with (a) 14% water and (b) 22% water.

Table 6-1: The average lattice parameters and surface area per molecule obtained from the MD simulations and compared with those of experimental measurements and estimations.

Water concentration %	Lattice parameter (Å)		Surface area per molecule estimated (Å ²)	
	SAXS Exp. [203]	MD simulation	Estimation from Exp.[14]	MD simulation
14	39	40 ± 1	33	39 ± 4
22	42	41 ± 1	43	44 ± 4

The lyotropic H_{II} self-assembly of C₈C₁₂β-D-Glc has three regions, namely water, sugar head region and hydrocarbon chain. Slight overlapping between regions is

expected at the interface. Taking advantage of the hexagonal symmetry, we calculated the radial distribution of the mass density with a center located in the water region of cylinder number 5 (see Figure 6-1) as a reference point. The radial density distributions are as displayed in Figure 6-2. Extensive overlapping exists in the H_{II} of $C_8C_{12}\beta$ -D-Glc with 14% water concentration Figure 6-2 (a), implying the sugar head group penetrates into the water channel. In contrast, the overlapping of sugar and water density profiles is less in the system with 22% water. This suggests at low water concentration, the sugar head is less able to separate from the water region, compare to the case of a higher water concentration where water column free of sugar head group is found. Based on these results, we estimated the area per head group, A , using the equation,

$$A = \frac{2\pi r L}{N}. \quad (6.1)$$

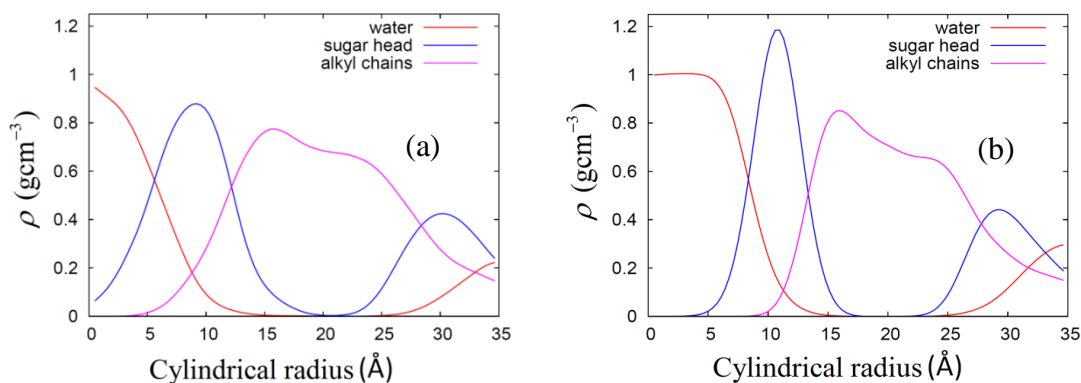


Figure 6-2: The radial density profiles of water, sugar head group and alkyl chains for $C_8C_{12}\beta$ -D-Glc system of H_{II} with (a) 14% water and (b) 22% water.

where, r denotes the average radial distance of the sugar head group from the centre of the cylinder, estimated based on the position of the first peak of the sugar head density in Figure 6-2, which is 9.5 Å and 11.5 Å for systems of 14% and 22% water, respectively. L denotes the length of the cylinder and N denotes the number of molecule $C_8C_{12}\beta$ -D-Glc forming the cylinder. For both systems, N is 70, while L is about 46 Å and

47 Å for the 14% and 22% water systems, respectively. In the SAXS experiment, the area per head group can be estimated based on the lattice parameter [17, 183, 204]. The simulated area per head group and its estimation based on the SAXS experiment are given in Table 6-1. For the 22% system, our simulation shows the area per head group being remarkably close to that estimated by the SAXS data. But for the system at lower water concentration (14%), the results from the two techniques differ by about 15%, which is still acceptable to within the error of the measurements for area per lipid, commonly observed for many lipidic systems [180]. Thus, the simple united atom model applied here is effective to represent the hexagonal phase formed by the chosen Guerbet glycoside [205]. These two concentrations, (14%) and (22%), were chosen based on the small angle X-ray measurements which have been reported corresponding to the reverse hexagonal phase. The later concentration, in excess water, is more relevant in biological environment.

6.2 Diffusion of water molecules in the water channel of H_{II}

It is well known that the dynamics of water confined in the nanoscale space is different from that of bulk water [206, 207], since the interactions between the water molecules to its wall is significant in an overall system. These interactions depend on the type of functional groups on the wall [208, 209], which could be stronger in the confined environment than in the bulk [210, 211]. The famous examples of such a condition are water inside the carbon nanotube [212, 213] and the aquaporin [214-216]. One of the direct consequences of the water wall interaction is the flow properties of the confined water. Recent experiment has found heterogeneity in the diffusion of the water regions within the H_{II} system formed by the hexaethylene glycol, a non-ionic surfactant [217]. Since C₈C₁₂β-D-Glc is also a non-ionic surfactant, we believe the behavior of waters in its H_{II} phase resembles that of a hydrophilic nano-channel, similar to the case

of hexaethylene glycol referred to previously[217]. The experimental results showed that in the reverse hexagonal phase, H_{II}, there are two types of diffusions, namely ordinary Einstein's diffusion (due to the thermal effect) and an anomalous diffusion, which may be due to the restricted motion. The Einstein diffusion phenomena can be described by the Einstein relation, $\langle \Delta r^2 \rangle \sim t$, where $\langle \Delta r^2 \rangle$ is the mean square displacement of particles and t is the time. This relationship can be written into Einstein's diffusion equation,

$$\langle \Delta r^2 \rangle = 2dDt, \quad (6.2)$$

where d is the dimension of the displacement and, D is the diffusion coefficient. Meanwhile in the anomalous diffusion phenomena, the relationship between $\langle \Delta r^2 \rangle$ and t is accordingly to the power law as:

$$\langle \Delta r^2 \rangle \sim t^\alpha \text{ where } \alpha \neq 1. \quad (6.3)$$

We investigated the diffusion behavior of two simulated systems by calculating the mean square displacement of the water molecules. The mean square displacement along the columnar axis, i.e. the z -axis, was calculated separately from the mean square displacement in the plane perpendicular to the columnar axis, i.e. the xy -plane. These calculations were performed using the utility program *g_msdis* in the GROMACS software package. The log-log plots of the mean square displacement as a function of time are given Figure 6-3.

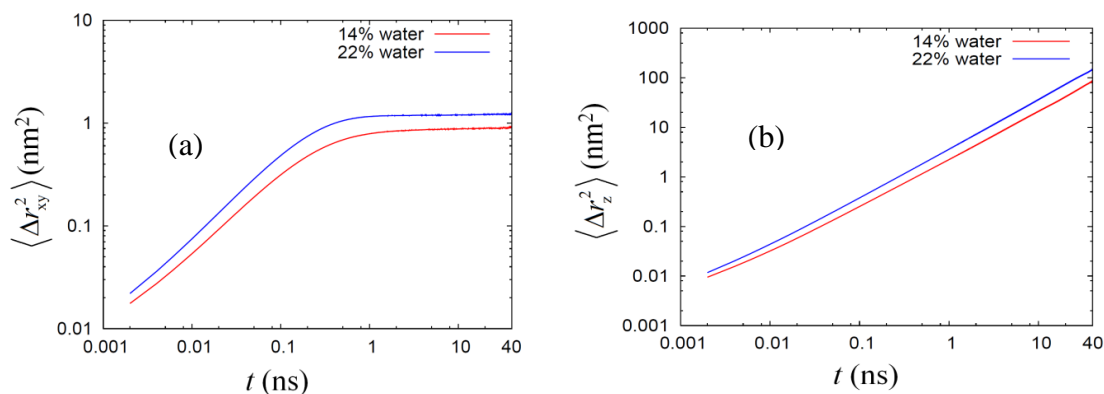


Figure 6-3: The mean square displacements of water versus time (a) in the xy plane and (b) in the z direction

Figure 6-3 shows the mobilities of confined water in the z direction and the xy plane are higher for the system of higher water concentration. Figure 6-3 (a), shows the diffusion of water in the xy direction is anomalous, with the exponents α equal to 0.76 and 0.81 for system of 14% water and 22% water, respectively (see Table 6-2) for the region less than 100ps. These results were obtained by a linear regression analysis, where values of α were calculated from the slope of the linear fitting lines. We observed that the time scale for the anomalous diffusion is independent of the water concentration. Beyond 100ps, the mean square displacement of water levels off at different limiting values for different concentrations. Moreover, the limiting mean square displacement for the 22% system is larger compared to that for the lower concentration system. In the former, the motion of water is less confined since it has a bigger water channel. In addition, upon close inspection of these long time-scale diffusions, we found that these are not completely flat. Instead, both have significantly measurable gradients (see Table 6-2). In contrast, the diffusion along the z -direction in Figure 6-3 (b), for the 22% system conforms to the Einstein's relation, while for the less concentrated system 14% water, this deviates slightly from the Einstein's relation (see Table 6-2). Ignoring the slight deviation, and assuming a normal behavior for both, the values of the diffusion coefficients for the 14% and 22% systems are $(1.0 \pm 0.1) \times 10^{-5} \text{ cm}^2 \text{ s}^{-1}$ and $(1.8 \pm 0.1) \times 10^{-5} \text{ cm}^2 \text{ s}^{-1}$, respectively. Compared to the diffusion of SPC water measured

in a bulk system, which is $(4.20 \pm 0.01) \times 10^{-5} \text{ cm}^2 \text{ s}^{-1}$ [218], these simulated values are 4–2 times slower.

Table 6-2: The exponents α for the diffusion of water in the xy plane and the z direction and the diffusion coefficient D in the z direction for the $\text{C}_8\text{C}_{12}\beta\text{-D-Glc}$ system at 14% and 22% water.

System	Diffusion in the xy plane		Diffusion in the z axis	
	α when $t \leq 100$ ps	α when $t \geq 5$ ns	α over the production	D (10^{-5} cm^2/s)
14% water	0.76	0.02	0.98	1.1 ± 0.1
22% water	0.81	0.01	1.00	1.8 ± 0.1

Since $\text{C}_8\text{C}_{12}\beta\text{-D-Glc}$ is a non-ionic surfactant and the sugar head group is not too different from the glycol moiety of a similar common surfactant hexaethylene glycol (C_{12}E_6) the water diffusion phenomena for both should be relatively similar. Therefore our simulation results could offer an alternative detailed explanation for the particles tracking experiment in the H_{II} phase formed by hexaethylene glycol. They measured the diffusion of polystyrene (PS) probes using optical tweezers technique in isotropic, reverse hexagonal and lamellar phases at three concentrations, 20%, 50% and 80% of C_{12}E_6 respectively. They found that the diffusions of PS in both lamellar and isotropic phases conform to a normal diffusion pattern, but in the reverse hexagonal phase, both normal diffusion and sub-diffusion behavior was observed. They explained that the presence of two diffusions phenomena is due to the heterogeneous local environment within the reverse hexagonal structure, i.e. the presence of an isotropic local domain where PS diffusion is normal, and a hexagonal local domain where the PS diffusion is restricted giving the sub-diffusion phenomenon. However, based on our simple simulation model of the reverse hexagonal phase, the diffusion of water in the z axis along the column is normal but in the xy plane is sub-diffusion. Since the particle tracking experiment only captured two-dimensional displacements of the PS, the diffusion pattern of the probe in 2D is necessarily subdiffusion depending on the orientation of the water column with respect to the laboratory Z axis. Therefore, we

believe that the origin of heterogeneity in the local environment is due rather to the existence of the local domains of H_{II} in the measured sample with different columnar orientations. The probe particles inserted during the experiment could have been distributed among these local domains, therefore various diffusion behaviours were observed. To show how is the orientation of columnar axis affects the two-dimensional diffusion pattern, we begin with a three dimensional mean square displacement of a probe particle in a certain columnar phase, denoted by $\langle r_{XYZ}^2 \rangle$, where the labels X, Y and Z represent the laboratory axes. $\langle r_{XYZ}^2 \rangle$ can be defined as:

$$\langle r_{XYZ}^2 \rangle = \langle \Delta X^2 \rangle + \langle \Delta Y^2 \rangle + \langle \Delta Z^2 \rangle, \quad (6.4)$$

where ΔX , ΔY and ΔZ are the components of the displacements in the laboratory axis. Next, we define a columnar axis system denoted as x , y and z for a column in the H_{II} phase, where z is the principal axis of a particular column, while x and y axes form the plane perpendicular to the principal axis. The mean square displacement based on this reference axes is written as $\langle r_{xyz}^2 \rangle$ such that,

$$\langle r_{xyz}^2 \rangle = \langle \Delta x^2 \rangle + \langle \Delta y^2 \rangle + \langle \Delta z^2 \rangle. \quad (6.5)$$

Here, ΔX , ΔY and ΔZ are the displacements according to the columnar axis system. In principle,

$$\langle r_{XYZ}^2 \rangle = \langle r_{xyz}^2 \rangle. \quad (6.6)$$

If the z axis of this column deviates from the Z axis by an angle θ ,

$$\Delta Z = \Delta z \cos \theta. \quad (6.7)$$

In the particles-tracking experiment, the two-dimensional displacement measured is $\langle r_{XY}^2 \rangle$. Consequently,

$$\langle r_{XY}^2 \rangle = \langle r_{XYZ}^2 \rangle - \langle \Delta Z^2 \rangle = \langle r_{xyz}^2 \rangle - \langle \Delta z^2 \rangle \cos^2 \theta. \quad (6.8)$$

As shown in our simulation, the diffusion of water molecules in the confined xy plane behaves anomalously, hence the probe particles' diffusion should behave likewise. This implies that:

$$\langle r_{xy}^2 \rangle = 4D_{xy}t^\beta, \quad (6.9)$$

and

$$\langle \Delta z^2 \rangle = 2D_z t, \quad (6.10)$$

where $0 < \beta < 1$, D_{xy} and D_z represent the diffusion coefficients in the xy plane and in the z -axis, respectively. Substituting, equation (6.9) and equation (6.10) into equation (6.8) we obtain,

$$\begin{aligned} \langle r_{XY}^2 \rangle &= [4D_{xy}t^\beta + 2D_z t] - (2D_z t) \cos^2 \theta = 4D_{xy}t^\beta + 2D_z t(1 - \cos^2 \theta) = \\ &\left(1 + \frac{2D_{xy}}{D_z(1 - \cos^2 \theta)} t^{\beta-1} \right) 2D_z t(1 - \cos^2 \theta). \end{aligned} \quad (6.11)$$

Equation (6.11) shows that the particle displacement measurement in two dimensions can deviate from the normal diffusion phenomenon depending on the orientation of the columnar axis. One can be seen that as long as $\theta \neq 0$, the time-dependent term,

$\frac{2D_{xy}}{D_z(1 - \cos^2 \theta)} t^{\beta-1}$ will decrease as time increases. Eventually, $\frac{2D_{xy}}{D_z(1 - \cos^2 \theta)} t^{\beta-1}$

becomes insignificant, then equation (6.11) effectively conform to Einstein's diffusion relation. Therefore, for a long enough time, the two-dimensional diffusion in the H_{II} is normal, except when the direction of the z axis of the column coincides with the laboratory Z axis, i.e. when $\theta=0$, where the anomalous diffusion will be observed. Moreover, when these two axes do not coincide but the time of measurement is long enough, only normal diffusion is observed, such that,

$$\langle r_{XY}^2 \rangle \approx 2D_z t (1 - \cos^2 \theta). \quad (6.12)$$

This means the diffusion coefficient measured in the laboratory reference axes, D_{lab} , is effectively related as,

$$D_{lab} = D_z (1 - \cos^2 \theta) / 2. \quad (6.13)$$

which is different according to the deviation angle between the principal z axis of the column and the Z axis in the laboratory frame.

From this analysis, we show that the 2D diffusion pattern observed depends on the columnar orientation with respect to the laboratory axis. In reality, the columns' orientations in the H_{II} at thermal equilibrium are not perfectly uniform due to the existence of local domains, which leads to deformations and defects in the system that can be observed under the polarizing microscope [219]. In the experiment, different probe particles inserted might fall into some parts of the columnar phase with different orientations, leading to different diffusion patterns observed. This seems to explain the diffusion phenomena H_{II} of $C_{12}E_6$ given by the experiment [217].

6.3 Interaction between water and sugar head group at different water concentrations

Within the reverse hexagonal phase, H_{II}, the water molecules interact extensively with the sugar head group at the interface between the water region and the sugar head region. One of the important interactions is the hydrogen bond, which involves the water molecules and the oxygen atoms from the sugar head group. These hydrogen bonding interactions can be extracted from the simulations. A hydrogen bond is characterized according to the geometric criteria such that the oxygen to oxygen atom distance must be less than 3.5 Å and the O-H...O angle less than 30° [220, 221]. Based on these criteria and using the *g_hbond* utilities software in GROMACS, we calculated the time-averaged number of hydrogen bond per sugar head for each hydroxyl group (donor) and the oxygen atoms (acceptor) on the sugar head itself (see Figure 6-4). The results of the calculations for the two water concentrations system are given in Table 6-3. It shows that for both water concentrations, among the six oxygen atoms acting as hydrogen bonding acceptors on the sugar head, O6 gives the highest number of hydrogen bond with water molecules, followed by O3, O2, O4, O5 and finally O1. Meanwhile, among the four hydroxyl groups on the sugar head, the highest hydrogen bond is the donor O4-H, followed by O3-H, O6-H and O2-H (Table 6-3).

Table 6-3 also shows that for each site, (both for donor and acceptor) the number of hydrogen bonds is higher for a high water system due to the higher availability of water molecules to participate in the hydrogen bond formation and a larger interface in the system of high water content.

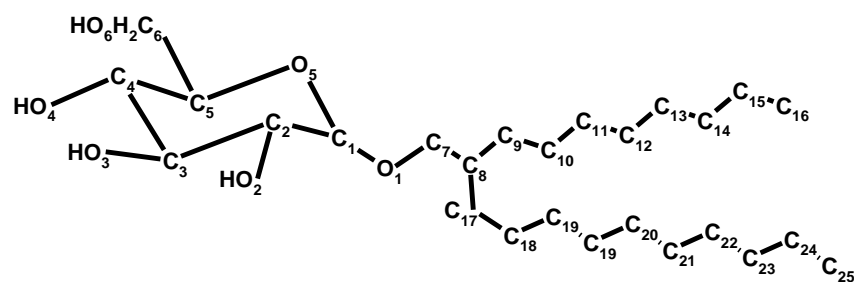


Figure 6-4: Designation of oxygen atoms on the sugar head for $C_8C_{12}\beta$ -D-Glc.

Table 6-3: Average number of hydrogen bonds on different oxygen sites of the sugar head and their respective lifetime

Water-sugar hydrogen bond		Average no. of hydrogen bond per sugar head		Hydrogen bond lifetime (ps)	
		14% water	22% water	14% water	22% water
Acceptor	O1...H-O _{water}	0.02	0.03	1.5	1.5
Acceptor	O2...H-O _{water}	0.30	0.36	30.8	18.0
Acceptor	O3...H-O _{water}	0.44	0.50	13.1	9.4
Acceptor	O4...H-O _{water}	0.27	0.29	15.6	13.6
Acceptor	O5...H-O _{water}	0.08	0.12	8.3	5.2
Acceptor	O6...H-O _{water}	0.57	0.69	16.7	11.9
Donor	O2-H...O _{water}	0.26	0.36	53.0	38.3
Donor	O3-H...O _{water}	0.34	0.40	32.5	25.1
Donor	O4-H...O _{water}	0.46	0.50	25.9	20.5
Donor	O6-H...O _{water}	0.34	0.43	39.0	31.8

The dynamics of the hydrogen bonding interactions between water and sugar head were also investigated. The lifetime of the hydrogen bond was analysed by calculating the autocorrelation function of the hydrogen bond existence, $C(\tau)$, defined as,

$$C(\tau) = \langle s_i(t) \rangle s_i \langle (t + \tau) \rangle, \quad (6.14)$$

Where $s_i(t) = \{0, 1\}$ [217, 222]. The lifetime of the hydrogen bond is,

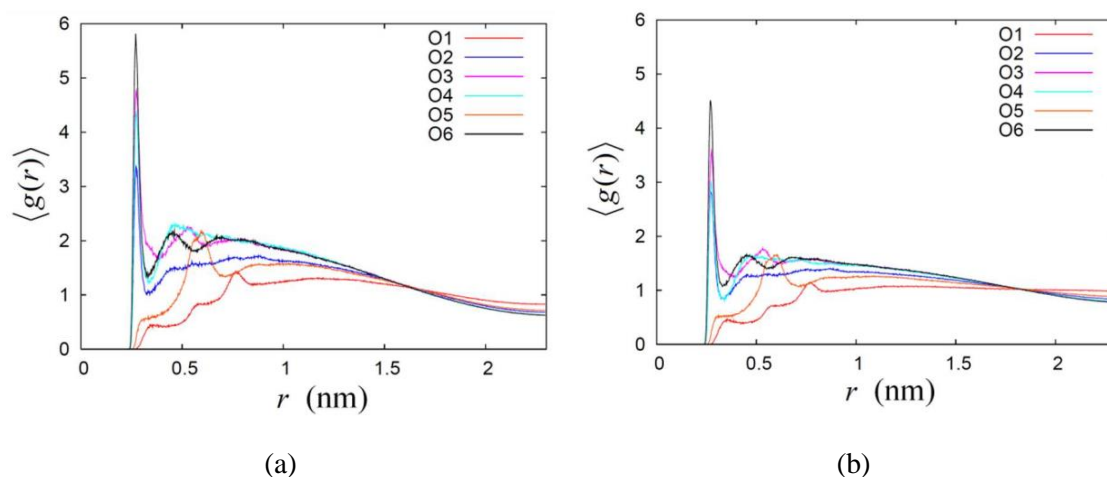


Figure 6-5: The radial distribution function (RDF) of water-oxygen around the six oxygen atoms for two systems (a) 14% and (b) 22% water concentrations

$$\tau_{life} = \int_0^{\infty} C(\tau) d\tau. \quad (6.15)$$

Table 6-3 gives the results of this analysis and shows that in both systems, the donor hydrogen bond at O2-H... O_{water} has the longest lifetime compared to other sites. In addition, the hydrogen bond O2...H-O_{water} has the longest lifetime among acceptor oxygen. This indicates that the water molecules are more confined, when bonded to the hydroxyl O2-H site compared to when bonded with the other hydroxyl groups. Consequently, water molecules close to the O2 site penetrate deeper into the sugar region and are somewhat trapped. On the other hand, even though the glycosidic oxygen O1 and O5 are located deeper within the sugar structure, their partial charges are less negative than those of O2. Therefore, the hydrogen bonds on O1 and O5 are less stable than that of O2. Table 3 also shows that the lifetime of each particular hydrogen bond considered for the system of 14% water, is longer than that of the 22% water system. This is expected since the diffusion of water molecules in smaller size water channels of 14% water is lower than in the 22% water system, which has a larger water channels.

Both systems also show differences in the number of hydrogen bonds with water at different hydroxyl group sites or oxygen atoms on the sugar head. This feature indicates different degrees of exposure of different parts of the sugar head group to the water molecules at the interface. This can be further illustrated by the radial distribution function (RDF) of the water oxygen atoms with respect to the six oxygen sites on the sugar head denoted as RDF_O x , where $x = 1, 2, \dots, 6$ denoting the particular site (see Figure 6-4). The RDF_O x of the two systems were calculated using the *g_rdf* utilities software in GROMACS, whose results are given in Figure 6-5. Qualitatively, the results of RDF_O x for both systems are rather similar regardless of the water concentration. For the two systems, RDF_O2, RDF_O3, RDF_O4 and RDF_O6 show the formation of hydration shells around the oxygen atoms O2, O3, O4 and O6. The RDF_O2 of both systems show only one definite water structure such that it peaks at the radial distance of 2.7 Å (see Figure 6-5), which corresponds to the first hydration shell around O1. Two water structures can be seen in the RDF_O3 and RDF_O4 of the two systems indicating two layers of hydration formed around their O3 and O4, while the RDF_O6 shows the existence of three hydration layers around the O6 site. The positions of the peaks in these four RDF_O x , for both systems, are similar and given in Table 6-4. Our simulation results were found to be comparable to those measurements for the peak positions of the water RDF with respect to another water molecule, namely RDF_OW, obtained from experimental measurement [223] except the positions of second peak for RDF_O3. Based on the number of hydration layers as well as the height of the RDF_O first peak, we can conclude that hydroxyl group O6-H is most exposed to water, and this is followed by O3-H, O4-H and O2-H. This also means that the oxygen O6 penetrates deepest into the water region, and belongs to the outermost region of the water-sugar interface.

Table 6-4: The peak positions in the oxygen to oxygen RDF of water for the four oxygen atoms from the hydroxyl groups, namely O2, O3, O4 and O6. These are compared with those from the experimental measurements for RDF of oxygen to oxygen in the bulk water.

RDF	Peak positions (Å)		
	1st	2nd	3rd
RDF_O2	2.72	Nil	Nil
RDF_O3	2.74	5.31	Nil
RDF_O4	2.74	4.60	Nil
RDF_O6	2.70	4.50	6.82
RDF_OW[223]	2.88	4.50	6.73

On the other hand, RDF_O1 and RDF_O5 show the highest peak at the radial distance of 7.6 Å and 6.0 Å, respectively. The radial distances of these two peaks can be explained approximately as the distance of O1 and O5, to the water structure right outside the outermost region of water–sugar interface formed by O6-H, as explained previously. The estimated distances are obtained by approximating the distances of O1 and O5 to O6, i.e. 6.0 Å and 3.7 Å, plus the radial distance of first water structure for O6, which is 2.7 Å. This gives approximately 8.7 Å and 6.4 Å for O1 and O5, respectively, which are close to their respective peaks positions in the RDF_O.

6.4 The packing of the alkyl chains

It is known that the cross-section of a column in the H_{II} is not a smooth circular shape, but instead this is a hexagon with smooth corners [17, 224-226]. This hexagonal shaped column is necessary for the columnar structure to fill the space while maintaining the hexagonal lattice arrangement. This would mean the alkyl chains have to stretch out to the corner and be compressed on the face of the hexagon. The energy of compression and the extension of the alkyl chains is called the frustration energy [19]. To see this effect in our simulation systems, we calculated the distribution of the radial distance from the methyl group, CH₃, from the centre of its cylinder with respect

to the angle around the column axis. We focused our analysis on the middle cylinder number 5 for the two systems from 10ns to 50ns, i.e. during the production stage.

Figure 6-6 gives the time averaged radial distances of CH₃ from the centre of the cylinder as a function of the angle around the column for the two simulation systems. The averaged radial distances of CH₃ for the two systems peaked roughly at the six hexagonal corners, indicated by the vertical straight lines in

Figure 6-6. On the other hand, the radial distances of CH₃ are lowest in between the two peaks, implying the compression of alkyl chain at the faces of the hexagon. In

Figure 6-6, the non-uniform heights among the peaks and the dips indicate imperfection in the cylindrical symmetry of the columnar phase.

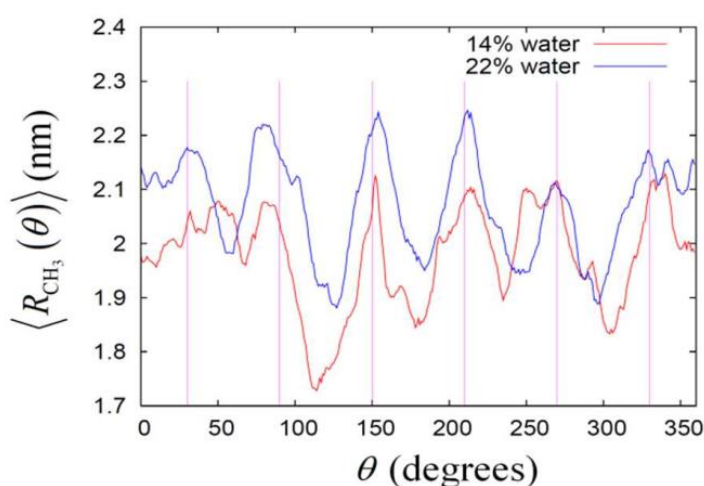


Figure 6-6: The distribution of the average radial distance of the CH₃ over angles around the cylinder, where the straight vertical lines are at the angles 30°, 90°, 120°, 180°, 240° and 270°

CHAPTER 7

CONCLUSION

In this chapter we shall bring the conclusion of each investigation separately and followed by the future research in this area.

7.1 Conclusion

In the first part of this thesis the geometrical and electronic structures of a series of five glycolipid crown ethers and their complexes with Na^+ and K^+ cations were studied using the B3LYP with the 6-31 G* basis set. The condensed Fukui functions were evaluated to give the local reactivity of the oxygen atoms on the crown ethers of each molecule to the nucleophilic attacks. It was found that these oxygen atoms were partially reactive, while the most reactive sites of each molecule tend to be located a distance away from the sugar ring. The calculated global nucleophilicity index revealed that upon optimization, smaller crown ethers size generally gave higher nucleophilicity. The five molecules give the energy gaps, which are close to one another. Among them, G16C5 has the highest energy gap, which means it has the highest chemical hardness. These molecules also have rather similar ionization potential but their electron affinities are sensitive to the difference in the geometrical size of their crown ethers. The lowest electron affinity is given by G16C5.

From the optimized structures of the glycolipid crown ethers, it was found that the cavity size of G15C5 is the best match with the Na^+ cation. The cavity size of G18C6 and G19C6 fits with K^+ better than other glycolipid crown ethers, where the cation is located at the mean plane of the crown ethers with all the oxygen coordinated to the encapsulated cation. On the other hands, there are a few cases, where the cavity sizes of the crown ether rings are too big such that some oxygen atoms are not coordinated to the cation. Furthermore, we observed that the sugar oxygen atoms O2, O3, O4 and O6 in their respective glycolipid crown ethers are in most cases further

away from the cation compare to other oxygen atoms in their respective crown ether rings. Constrained by the sugar ring, these sugars' oxygen atoms are hindered from getting nearer to the cation. These oxygen atoms move toward the cation by lowering their dihedral angles of O2-C-C-O3 or O4-C-C-C from their initial optimized structures.

The calculated binding energies, enthalpies and Gibbs energies in the gas phase at temperature 298 K showed that all five molecules bound more strongly with cation Na⁺ than K⁺. Based on this, the molecular binding stability with Na⁺ could be arranged in the order of G21C7 > G19C6 > G18C6 > G16C5 > G15C5, while that with K⁺ was in the order of G21C7 > G18C6 > G19C6 > G16C5 > G15C5. The exchange enthalpies and Gibbs energies for the exchange reaction calculated showed that the ion selective capability toward Na⁺ over K⁺ of these molecules was in the order of G15C5 > G16C5 > G21C7 > G19C6 > G18C6. Among them, the exchange enthalpy of G16C5 was close to G15C5 and both were significantly higher than the others. This was similar to the selectivity pattern found in the experiment in aqueous solution of equimolar cation Na⁺ and K⁺, [16] except for the G21C7, which might be due to the effect of the solvation of the water.

The second part of this thesis includes the fully atomistic MD simulations of the epimeric/anomeric quartet liner glycolipids with the same octylchain group, namely, α/β octyl-galactosides and α/β octyl-glucosides to investigate the stereo-chemical relationship. Local density profile, inter- and intra-molecular hydrogen bonds, average area at the interface per sugar, head group tilt angle and chain order parameter are some of the properties which have been used to scrutinise the effect of subtle stereochemical changes of these systems.

The results show that, the anomeric stereochemistry or the axial/equatorial orientation of C1-O1 (α/β) is an important factor controlling the area and d -spacing of glycolipid bilayer systems in thermotropic phase, while the epimeric stereochemistry is secondary. Thus, thickness for β -C8Glc/C8Gal is larger than that for α -C8Glc/C8Gal. Meanwhile the area per lipid head group is higher for the α -compound than for the β -compound. In addition, the head group tilt angles are similar for those in the fluid L_α of about 36–42, which is significantly larger than that for β -C8Gal in the L_C phase. Similarly, for the chain ordering property of the bilayer, the α -anomer was found to be less ordered compared to the β -anomer. Additionally, the assembly of sugar surfactant with α -anomer, in which the sugar head group bent to the hydrocarbon chain gave a slightly bent shape molecular structure, while in bilayer arrangement the alkyl chains of these surfactants packed less densely.

The C4-epimeric (axial/equatorial) stereochemistry becomes dominant together with the anomeric one for the inter-molecular hydrogen bond. Thus, the trend in hydrogen bonding goes as β -C8Gal > α -C8Glc > β -C8Glc > α -C8Gal, which is in agreement with the previous studies of Hashim *et al.*[10] and Rog *et al.*, [_ENREF_28\[47\]](#) implying the axial orientation of the hydroxyl group on the C4 position in β -C8Gal increases the capacity of donor and acceptor of this compound. Likewise, the α -glucoside has a similar behaviour. Therefore, these results support the proposal that when the hydroxyl group at the C4 carbon is cis with respect to the C1-O1 (i.e. β -C8Gal and α -C8Glc), greater bilayer stability is achieved compared to the case when these links are in a trans-configuration (i.e. β -C8Glc and α -C8Gal). The thermotropic bilayer of the four lipids studied here exhibited anomalous diffusion behaviours, where the observed trend for the diffusion coefficient for these compounds is (β -C8Gal > β -C8Glc > α -C8Gal > α -C8Glc). This trend shows that for a given epimer

(gluco- or galacto-), β -anomer is more diffusive than the α -anomer. The latter has more space in the hydrophobic region, causing both chain vibration and chain disorganization to increase, but reducing the overall molecular diffusion, since thermal energy is dispensed more entropically for the chain region.

In the third part of this dissertation, we have modelled and simulated the system of lyotropic H_{II} formed by C₈C₁₂ β -D-Glc at two different water concentrations, 14% and 22%, for 50 ns simulation. The average lattice parameters and area per head group obtained from the simulations for these systems agree quantitatively to within the error with those estimated from the SAXS measurements. At 14% water concentration the radial distribution of density profile shows the sugar head group region and the water region overlap each other, such that the water column is not completely free of the sugar head group. Meanwhile, at the higher concentration of 22% water, the water region in the column does not overlap extensively with the sugar head group and in fact, we also observed a sugar free water region. Two water diffusion processes are detected. While in the xy plane, the water mobility is anomalous for both systems. However, in the z direction the diffusion of 22% water system obeys Einstein's relationship, but for the less water system (14%), the diffusion is slightly anomalous. The anomalous diffusion in xy plane is caused by the confined space in the plane. Thus, our findings provide alternative explanation to the recent experimental results by Penaloza *et al.*, who found the space heterogeneity of diffusion in the water region of a lyotropic H_{II}.

The interactions between the sugar head and water molecules were investigated by the hydrogen bond analysis and the calculations of RDF of water oxygen atom around the six sugar oxygen atoms. In a system of 14% water, the number of hydrogen bonding between water and sugar is lower, but a longer lifetime was observed compared to that of the 22% water system. This is attributed to the smaller surface area of water-

sugar interface and lower mobility of water in the 14% water compared to that of the 22% water system. The RDF of water oxygen atom around the six sugar oxygen atoms relates the level of contact or exposure of individual oxygen on sugar to the water molecules, which follows the ordering of $O_6 > O_3 > O_4 > O_2 > O_5 > O_1$ regardless of the water concentrations. Finally, we examined the extension and compression of the alkyl chain by calculating the distribution of average radial distance of CH_3 group over angle around a cylinder. The profile of the distribution conforms to the description in the frustration theory.

To summarise, we have used extensively the computer modelling and simulation techniques to understand and explore the self-assembly behaviour of bulky systems (micellar, bilayers and hexagonal phases). In future, we can use quantum mechanical calculation to obtain the electronic properties of branched synthetic glycolipid systems. This will give an improved force-field for these materials to study their self-assembly in both polar and nonpolar solvents. In addition, the hybrid QM/MM approach is another molecular simulation method which uses both QM (for improved accuracy) and MM (for higher speed) calculations, thus allowing for the study of chemical processes in solution and in proteins. The development of the hybrid QM/MM approaches is guided by the general idea that large chemical systems may be partitioned into an electronically important region which requires a quantum chemical treatment and a remainder which only acts in a perturbation fashion and thus admits a classical description. Therefore, in future we plan to use this method to study the complex self-assembly behaviour.

REFERENCES

1. Mouritsen, O.G. and K. Jørgensen, *A new look at lipid-membrane structure in relation to drug research*. *Pharmaceutical research*, 1998. **15**(10): p. 1507-1519.
2. Merz Jr, K.M. and B. Roux, *A Molecular Perspective from Computation and Experiment*. 1996: Birkhäuser, Boston.
3. R. Komanduria, E-mail the corresponding author, and L.M.R. N. Chandrasekarana, *Molecular dynamics (MD) simulation of uniaxial tension of some single-crystal cubic metals at nanolevel*. *International Journal of Mechanical Sciences*, 2001. **43**.
4. Alder, B.J. and T. Wainwright, *Studies in molecular dynamics. I. General method*. *The Journal of Chemical Physics*, 1959. **31**: p. 459.
5. Korn, E.D., *Structure of biological membranes*. *Science*, 1966. **153**(3743): p. 1491-8.
6. Boullanger, P., *Amphiphilic carbohydrates as a tool for molecular recognition in organized systems*. *Glycoscience Synthesis of Substrate Analogs and Mimetics*, 1997: p. 275-312.
7. Hato, M., et al., *Self-assembly of synthetic glycolipid/water systems*. *Advances in colloid and interface science*, 1999. **80**(3): p. 233-270.
8. Balzer, D. and H. Luders, *Nonionic surfactants: Alkyl polyglucosides*. Vol. 91. 2000: CRC.
9. Shinoda, K., T. Yamanaka, and K. Kinoshita, *Surface Chemical Properties in Aqueous Solutions of Non-ionic Surfactants Octyl Glycol Ether, α -Octyl Glyceryl Ether and Octyl Glucoside*. *The Journal of Physical Chemistry*, 1959. **63**(5): p. 648-650.
10. Dupuy, C., et al., *Anomeric effects on the structure of micelles of alkyl maltosides in water*. *Langmuir*, 1997. **13**(15): p. 3965-3967.
11. Vill, V. and R. Hashim, *Carbohydrate liquid crystals: structure–property relationship of thermotropic and lyotropic glycolipids*. *Current opinion in colloid & interface science*, 2002. **7**(5): p. 395-409.
12. Barón, M., *Definitions of basic terms relating to low-molar-mass and polymer liquid crystals*. *PURE AND APPLIED CHEMISTRY* 2001. **73**(5): p. 845-895.
13. Tschierske, C., *Amphotropic liquid crystals*. *Current opinion in colloid & interface science*, 2002. **7**(5-6): p. 355-370.
14. Seddon, J.M., *Structure of the inverted hexagonal (H II) phase, and non-lamellar phase transitions of lipids*. *Biochimica et Biophysica Acta (BBA)/Reviews on Biomembranes*, 1990. **1031**(1): p. 1-69.
15. P. Sakya, J.M. Seddon, and R. H. Templer, *J. Phys. II.*, 1994. **4**: p. 1311-1331.
16. Israelachvili, J.N., *Intramolecular and Surface Forces* 1992, London: Academic press.
17. Seddon, J.M., *Structure of the inverted hexagonal (HII) phases, and non-lamellar phase transitions of lipids*. *Biochimica et Biophysica Acta*, , 1990. **1031**: p. 1-69.
18. Barón, M., *Definitions of basic terms relating to low-molar-mass and polymer liquid crystals (IUPAC Recommendations 2001)*. *Pure and Applied Chemistry*, 2001. **73**(5): p. 845-895.
19. Shearman, G.C., et al., *Calculations of and evidence for chain packing stress in inverse lyotropic bicontinuous cubic phases*. *Langmuir*, 2007. **23**(13): p. 7276-7285.
20. Uddin, M.H., N. Kanei, and H. Kunieda, *Solubilization and emulsification of perfume in discontinuous cubic phase*. *Langmuir*, 2000. **16**(17): p. 6891-6897.

21. Nishida, Y., et al., *An easy α -glycosylation methodology for the synthesis and stereochemistry of mycoplasma α -glycolipid antigens*. Beilstein Journal of Organic Chemistry, 2012. **8**.
22. Kitamoto, D., H. Isoda, and T. Nakahara, *Functions and potential applications of glycolipid biosurfactants—from energy-saving materials to gene delivery carriers*—. Journal of bioscience and bioengineering, 2002. **94**(3): p. 187-201.
23. Hantgan, R.R., J.V. Braaten, and M. Rocco, *Dynamic light scattering studies of α . IIb. beta. 3 solution conformation*. Biochemistry, 1993. **32**(15): p. 3935-3941.
24. Wiegandt, H., *Glycolipids*. Vol. 10. 1985: Elsevier Science.
25. Yamashita, T., et al., *A vital role for glycosphingolipid synthesis during development and differentiation*. Proceedings of the National Academy of Sciences, 1999. **96**(16).
26. Simons, K. and D. Toomre, *Lipid rafts and signal transduction*. Nature Reviews Molecular Cell Biology, 2000. **1**(1): p. 31-39.
27. Hunter, T., *Signaling--2000 and beyond*. Cell, 2000. **100**(1).
28. Kasahara, K. and Y. Sanai, *Functional roles of glycosphingolipids in signal transduction via lipid rafts*. Glycoconjugate journal, 2000. **17**(3): p. 153-162.
29. Gillard, B.K., L.T. Thurmon, and D.M. Marcus, *Variable subcellular localization of glycosphingolipids*. Glycobiology, 1993. **3**(1): p. 57-67.
30. Stubenrauch, C., et al., *Interactions between nonpolar surfaces coated with the nonionic surfactant hexaoxyethylene dodecyl ether C12E6 and the origin of surface charges at the air/water interface*. Langmuir, 2004. **20**(12): p. 4977-4988.
31. Allende, D., S. Simon, and T.J. McIntosh, *Melittin-induced bilayer leakage depends on lipid material properties: evidence for toroidal pores*. Biophysical journal, 2005. **88**(3): p. 1828-1837.
32. Cheng, K.H., et al., *The role of cholesterol in the activity of reconstituted Ca-ATPase vesicles containing unsaturated phosphatidylethanolamine*. Journal of Biological Chemistry, 1986. **261**(11): p. 5081-5087.
33. Seddon, J.M., et al., *Phosphatidylcholine-fatty acid membranes: effects of headgroup hydration on the phase behaviour and structural parameters of the gel and inverse hexagonal ($H < sub > II < /sub >$) phases*. Biochimica et Biophysica Acta (BBA)-Biomembranes, 1997. **1327**(1): p. 131-147.
34. Pedersen, C.J., *Cyclic polyethers and their complexes with metal salts*. Journal of the American Chemical Society, 1967. **89**(26): p. 7017-7036.
35. Pedersen, C.J., *The discovery of crown ethers (Noble Lecture)*. Angewandte Chemie International Edition in English, 1988. **27**(8): p. 1021-1027.
36. Cram, D.J. and J.M. Cram, *Design of complexes between synthetic hosts and organic guests*. Accounts of Chemical Research, 1978. **11**(1): p. 8-14.
37. Bradshaw, J.S. and R.M. Izatt, *Crown ethers: The search for selective ion ligating agents*. Accounts of Chemical Research, 1997. **30**(8): p. 338-345.
38. Gokel, G.W., W.M. Leevy, and M.E. Weber, *Crown Ethers: Sensors for Ions and Molecular Scaffolds for Materials and Biological Models*. ChemInform, 2004. **35**(32): p. no-no.
39. Payer, D., et al., *Toward mechanical switching of surface-adsorbed [2]catenane by in situ copper complexation*. Journal of the American Chemical Society, 2007. **129**(50): p. 15662-15667.
40. Ruben, M., et al., *2D supramolecular assemblies of benzene-1,3,5-triyl-tribenzoic acid: Temperature-induced phase transformations and hierarchical organization with macrocyclic molecules*. Journal of the American Chemical Society, 2006. **128**(49): p. 15644-15651.

41. Lehn, J.-M., *Toward complex matter: Supramolecular chemistry and self-organization*. Proceedings of the National Academy of Sciences of the United States of America, 2002. **99**(8): p. 4763-4768.
42. Gokel, G.W. and A. Mukhopadhyay, *Synthetic models of cation-conducting channels*. Chemical Society Reviews, 2001. **30**(5): p. 274-286.
43. Barboiu, M., G. Vaughan, and A. van der Lee, *Self-organized heteroditopic macrocyclic superstructures*. Organic Letters, 2003. **5**(17): p. 3073-3076.
44. Cazacu, A., et al., *Columnar self-assembled ureido crown ethers: An example of ion-channel organization in lipid bilayers*. Journal of the American Chemical Society, 2006. **128**(29): p. 9541-9548.
45. Sabah, K., T. Heidelberg, and R. Hashim, *Novel crown ethers on glucose based glycolipids*. Carbohydrate Research, 2011.
46. Karplus, M. and J.A. McCammon, *Molecular dynamics simulations of biomolecules*. Nat Struct Biol, 2002. **9**(9): p. 646-52.
47. Tavernelli, I., S. Cotesta, and E.E. Di Iorio, *Protein dynamics, thermal stability, and free-energy landscapes: a molecular dynamics investigation*. Biophys J, 2003. **85**(4): p. 2641-9.
48. Saiz, L., S. Bandyopadhyay, and M.L. Klein, *Towards an understanding of complex biological membranes from atomistic molecular dynamics simulations*. Biosci Rep, 2002. **22**(2): p. 151-73.
49. Metropolis, N. and S. Ulam, *The monte carlo method*. Journal of the American statistical association, 1949. **44**(247): p. 335-341.
50. Rahman, A. and F.H. Stillinger, *Molecular dynamics study of liquid water*. The Journal of Chemical Physics, 1971. **55**: p. 3336.
51. Cornell, W.D., et al., *A second generation force field for the simulation of proteins, nucleic acids, and organic molecules*. Journal of the American Chemical Society, 1995. **117**(19): p. 5179-5197.
52. Binder, K., *Monte Carlo and Molecular Dynamics Simulations Polymer*. 1995: Oxford University Press, Inc.
53. Verlet, L., *Computer" experiments" on classical fluids. I. Thermodynamical properties of Lennard-Jones molecules*. Physical review, 1967. **159**(1): p. 98.
54. Plotter, M.-D., *Computational physics*. 2012.
55. Leach, A.R. and D. Schomburg, *Molecular modelling: principles and applications*. 1996: Longman London.
56. Kirschner, K.N., et al., *GLYCAM06: a generalizable biomolecular force field. Carbohydrates*. Journal of computational chemistry, 2008. **29**(4): p. 622-655.
57. Heermann, D.W., *Computer simulation methods: in theoretical physics*. 1986.
58. Leach, A. and L.B. Kier, *Molecular modeling: principles and applications*. Journal of Medicinal Chemistry, 1997. **40**(18): p. 2969-2969.
59. Hansson, T., C. Oostenbrink, and W. van Gunsteren, *Molecular dynamics simulations*. Current opinion in structural biology, 2002. **12**(2): p. 190-196.
60. Haile, J.M., *Molecular Dynamics Simulation-Elementary Methods*, John Willey & Sons. Inc., New York, 1992.
61. Loncharich, R.J. and B.R. Brooks, *The effects of truncating long - range forces on protein dynamics*. Proteins: Structure, Function, and Bioinformatics, 1989. **6**(1): p. 32-45.
62. Lagüe, P., R.W. Pastor, and B.R. Brooks, *Pressure-based long-range correction for Lennard-Jones interactions in molecular dynamics simulations: Application to alkanes and interfaces*. The Journal of Physical Chemistry B, 2004. **108**(1): p. 363-368.

63. Baumketner, A. and J.E. Shea, *The influence of different treatments of electrostatic interactions on the thermodynamics of folding of peptides*. The Journal of Physical Chemistry B, 2005. **109**(45): p. 21322-21328.
64. Christen, M., et al., *The GROMOS software for biomolecular simulation: GROMOS05*. Journal of computational chemistry, 2005. **26**(16): p. 1719-1751.
65. Darden, T., D. York, and L. Pedersen, *Particle mesh Ewald: An $N \cdot \log(N)$ method for Ewald sums in large systems*. The Journal of chemical physics, 1993. **98**: p. 10089-10089.
66. Young, D., *Computational chemistry: a practical guide for applying techniques to real world problems*. 2004: Wiley. com.
67. Shalini, M., et al., *Microwave-assisted synthesis, anticonvulsant activity and quantum mechanical modelling of N-(4-bromo-3-methylphenyl) semicarbazones*. Journal of Zhejiang University SCIENCE B, 2007. **8**(1): p. 45-55.
68. Atkins, P.W. and R.S. Friedman, *Molecular quantum mechanics*. Vol. 3. 1997: Oxford university press Oxford.
69. Friesecke, G., *The multiconfiguration equations for atoms and molecules: charge quantization and existence of solutions*. Archive for rational mechanics and analysis, 2003. **169**(1): p. 35-71.
70. Lewin, M., *Solutions of the multiconfiguration equations in quantum chemistry*. Archive for rational mechanics and analysis, 2004. **171**(1): p. 83-114.
71. Nguan, H., S. Ahmadi, and R. Hashim, *DFT study of glucose based glycolipid crown ethers and their complexes with alkali metal cations Na^+ and K^+* . Journal of molecular modeling, 2012. **18**(12): p. 5041-5050.
72. Parr, R.G. and Y. Weitao, *Density-functional theory of atoms and molecules*. Vol. 16. 1994: Oxford University Press, USA.
73. Hohenberg, P. and W. Kohn, *Inhomogeneous electron gas*. Physical Review, 1964. **136**(3B).
74. Kohn, W. and L.J. Sham, *Self-consistent equations including exchange and correlation effects*. 1965: APS.
75. Pople, J.A. and D.L. Beveridge, *Approximate molecular orbital theory*. Vol. 30. 1970: McGraw-Hill New York.
76. Levine, I.N., *Quantum chemistry*. Vol. 5. 2000: Prentice Hall Upper Saddle River, NJ.
77. Auerbach, A., *Interacting electrons and quantum magnetism*. 1994: Springer.
78. Jensen, F., *Introduction to computational chemistry*. 2007: Wiley.
79. Christy, F.A. and P.S. Shrivastav, *Conductometric Studies on Cation-Crown Ether Complexes: A Review*. Critical Reviews in Analytical Chemistry, 2011. **41**(3): p. 236-269.
80. Lamb, J.D., et al., *The relationship between complex stability constants and rates of cation transport through liquid membranes by macrocyclic carriers*. Journal of the American Chemical Society, 1980. **102**(22): p. 6820-6824.
81. Popov, A.I., J.M. Lehn, and G.A. Melson, *Coordination Chemistry of Macrocyclic Compounds*. by GA Melson, Plenum Press, New York, 1979.
82. Kasapbasi, E.E. and M. Yurtsever, *A DFT study on the structural and optical properties and cation selectivities of some metal-coumarin-crown ether complexes*. Turk. J. Chem, 2012. **36**: p. 147-158.
83. Damewood Jr, J.R., W.P. Anderson, and J.J. Urban, *A molecular mechanics study of neutral molecule complexation with crown ethers*. Journal of computational chemistry, 1988. **9**(2): p. 111-124.
84. Erk, Ç., *Cation Recognition with Fluorophore Crown Ethers 1*. Industrial & engineering chemistry research, 2000. **39**(10): p. 3582-3588.

85. Dang, L.X. and P.A. Kollman, *Free energy of association of the 18-crown-6: K⁺ complex in water: a molecular dynamics simulation*. Journal of the American Chemical Society, 1990. **112**(15): p. 5716-5720.
86. Thompson, M.A., E.D. Glendening, and D. Feller, *The nature of K⁺/crown ether interactions: A hybrid quantum mechanical-molecular mechanical study*. The Journal of Physical Chemistry, 1994. **98**(41): p. 10465-10476.
87. Hou, H., X. Zeng, and X. Liu, *DFT study of a series of crown-4 ethers and their selectivity trend for alkali metal cations: Li⁺ and Na⁺*. Journal of Molecular Modeling, 2009. **15**(2): p. 105-111.
88. Su, C.C., L.H. Lu, and L.K. Liu, *Comparative study of molecular mechanics and theoretical conformational analysis of a new 16-crown-5 ether via X-ray crystallography and NMR spectroscopy*. The Journal of Physical Chemistry A, 2003. **107**(22): p. 4563-4567.
89. Grushin, V.V., C. Bensimon, and H. Alper, *Potassium complexes containing both crown ether and tertiary phosphine oxide ligands*. Inorganic Chemistry, 1993. **32**(3): p. 345-346.
90. Martinez-Haya, B., et al., *Spectroscopic investigation of the gas-phase conformations of 15-crown-5 ether complexes with K⁺*. J Phys Chem A, 2009. **113**(27): p. 7748-52.
91. Martinez-Haya, B., et al., *Emergence of symmetry and chirality in crown ether complexes with alkali metal cations*. J Phys Chem A, 2010. **114**(26): p. 7048-54.
92. Glendening, E.D., D. Feller, and M.A. Thompson, *An ab initio investigation of the structure and alkali metal cation selectivity of 18-crown-6*. Journal of the American Chemical Society, 1994. **116**(23): p. 10657-10669.
93. Martínez-Haya, B., et al., *Emergence of symmetry and chirality in crown ether complexes with alkali metal cations*. The Journal of Physical Chemistry A, 2010. **114**(26): p. 7048-7054.
94. Kowall, T. and A. Geiger, *Molecular dynamics simulation study of 18-crown-6 in aqueous solution. 1. Structure and dynamics of the hydration shell*. The Journal of Physical Chemistry, 1994. **98**(24): p. 6216-6224.
95. Dang, L.X., *Mechanism and thermodynamics of ion selectivity in aqueous solutions of 18-crown-6 ether: a molecular dynamics study*. Journal of the American Chemical Society, 1995. **117**(26): p. 6954-6960.
96. Kaasgaard, T. and C.J. Drummond, *Ordered 2-D and 3-D nanostructured amphiphile self-assembly materials stable in excess solvent*. Phys. Chem. Chem. Phys., 2006. **8**(43): p. 4957-4975.
97. Bogusz, S., R.M. Venable, and R.W. Pastor, *Molecular dynamics simulations of octyl glucoside micelles: structural properties*. The Journal of Physical Chemistry B, 2000. **104**(23): p. 5462-5470.
98. Teoh, T.C., R. Hashim, and *Molecular dynamics simulations of n-octyl-β-D-glycosides: some structural properties of micelles*. Malaysian Journal of Science, 2003. **22**: p. 95-103.
99. He, L.Z., et al., *Determination of micelle structure of octyl-β-D-glucoside in aqueous solution by small angle neutron scattering and geometric analysis*. Journal of molecular liquid, 2000. **89**: p. 239-249.
100. Konidala, P., L. He, and B. Niemeyer, *Molecular dynamics characterization of n-octyl-β-D-glucopyranoside micelle structure in aqueous solution*. Journal of Molecular Graphics and Modelling, 2006. **25**(1): p. 77-86.
101. Kaasgaard, T. and C.J. Drummond, *Ordered 2-D and 3-D nanostructured amphiphile self-assembly materials stable in excess solvent*. Physical chemistry chemical physics, 2006. **8**: p. 4957-4975.

102. Lopez, C.F., et al., *Hydrogen bonding structure and dynamics of water at the dimyristoylphosphatidylcholine lipid bilayer surface from a molecular dynamics simulation*. The Journal of Physical Chemistry B, 2004. **108**(21): p. 6603-6610.
103. Shinoda, W., et al., *Dynamics of a highly branched lipid bilayer: a molecular dynamics study*. Chemical Physics Letter, 2004. **390**,(1-3): p. 35-40.
104. Róg, T., et al., *Glycolipid membranes through atomistic simulations: effect of glucose and galactose head groups on lipid bilayer properties*. the Journal of physical chemistry B, 2007. **111**(34): p. 10146-10154.
105. Stephenson, B.C., et al., *Application of computer simulation free-energy methods to compute the free energy of micellization as a function of micelle composition. 2. Implementation*. J Phys Chem B, 2008. **112**(6): p. 1641-56.
106. Chong, T.T., R. Hashim, and R.A. Bryce, *Molecular Dynamics Simulation of Monoalkyl Glycoside Micelles in Aqueous Solution: Influence of Carbohydrate Headgroup Stereochemistry*. The Journal of Physical Chemistry B, 2006. **110**(10): p. 4978-4984.
107. Chong, T.T., et al., *Computer modelling and simulation of thermotropic and lyotropic alkyl glycoside bilayers*. Liquid Crystals, 2007. **34**(2): p. 251-265.
108. Manickam Achari, V., et al., *Molecular Dynamics Study of Anhydrous Lamellar Structures of Synthetic Glycolipids: Effects of Chain Branching and Disaccharide Headgroup*. the Journal of Physical Chemistry B, 2012. **106**(38): p. 11626-11634.
109. Murtola, T., et al., *Transient ordered domains in single-component phospholipid bilayers*. Phys Rev Lett, 2006. **97**(23): p. 238102.
110. Ollila, S., M.T. Hyvonen, and I. Vattulainen, *Polyunsaturation in lipid membranes: dynamic properties and lateral pressure profiles*. J Phys Chem B, 2007. **111**(12): p. 3139-50.
111. Bogusz, S., R.M. Venable, and R.W. Pastor, *Molecular dynamics simulations of octyl glucoside micelles: structural properties*. journal of physical chemistry B, 2000. **104**: p. 5462-5470.
112. chong, T.T., et al., *Computer modelling and simulation of thermotropic and lyotropic alkyl glycoside bilayers*. Liquid Crystals, 2007. **34**(2): p. 267-281.
113. Gradzielski, M., *Investigations of the dynamics of morphological transitions in amphiphilic systems*. Current opinion in colloid & interface science, 2004. **9**(3): p. 256-263.
114. Libster, D., A. Aserin, and N. Garti, *Interactions of biomacromolecules with reverse hexagonal liquid crystals: Drug delivery and crystallization applications*. Journal of Colloid and Interface Science, 2011. **356**(2): p. 375-386.
115. Ellens, H., et al., *Biochemistry*, 1989. **28**: p. 3692-3703.
116. Bernal, J.D. and Fankuchen, J. *Gen. Physiol*, 1941. **25**: p. 111-165.
117. Marsden Jr, S.S. and J.W. McBain, *X-Ray Diffraction in Aqueous Systems of Dodecyl Sulfonic Acid*. Journal of the American Chemical Society, 1948. **70**(5): p. 1973-1974.
118. Evans, D.F. and B.W. Ninham, *Molecular forces in the self-organization of amphiphiles*. The Journal of Physical Chemistry, 1986. **90**(2): p. 226-234.
119. Luzzati, V. and F. Husson, *The structure of the liquid-crystalline phasis of lipid-water systems*. J Cell Biol, 1962. **12**: p. 207-19.
120. Stoeckenius, W., *Some electron microscopical observations on liquid-crystalline phases in lipid-water systems*. J Cell Biol, 1962. **12**: p. 221-9.
121. Ekwall, P., L. Mandell, and K. Fontell, *Ternary systems of potassium soap, alcohol, and water:: I. Phase equilibria and phase structures*. Journal of Colloid and Interface Science, 1969. **31**(4): p. 508-529.

122. Takada, A., et al., *Columnar liquid crystals in oligosaccharide derivatives. II. Two types of discotic columnar liquid-crystalline phase of cellobiose alkanoates*. *Liquid Crystals*, 1992. **12**(2): p. 337-345.
123. Francescangeli, O., et al., *Evidence of an inverted hexagonal phase in self-assembled phospholipid-DNA-metal complexes*. *EPL (Europhysics Letters)*, 2004. **67**: p. 669-669.
124. Idayu Zahid, N., et al., *Characterization of the Head Group and the Hydrophobic Regions of a Glycolipid Lyotropic Hexagonal Phase Using Fluorescent Probes*. *Journal of physical chemistry. C*, 2011. **115**(40): p. 19805-19810.
125. Bandyopadhyay, S., et al., *Molecular dynamics studies of the hexagonal mesophase of sodium dodecylsulphate in aqueous solution*. *Molecular physics*, 1998. **95**(2): p. 377-384.
126. Kolev, V., et al., *Molecular dynamics approach to water structure of HII mesophase of monoolein*. *Journal of Chemical Physics*, 2012. **136**(7): p. 74509-74509.
127. Teoh T Chong, et al., *Computer Simulation of a Hexagonal Assembly for a Branched Chain Glycolipid*. *Malaysian Journal of Science*, 2008. **27**: p. 75-82.
128. Case, D.A., et al., *AMBER 12*, 2012, University of California: San Francisco.
129. Thurmond, R.L., G. Lindblom, and M.F. Brown, *Curvature, order, and dynamics of lipid hexagonal phases studied by deuterium NMR spectroscopy*. *Biochemistry*, 1993. **32**(20): p. 5394-5410.
130. Cristinziano, P.L. and F. Lelj, *Atomistic simulation of discotic liquid crystals: Transition from isotropic to columnar phase example*. *The Journal of chemical physics*, 2007. **127**: p. 134506-134506.
131. Alexandridis, P., U. Olsson, and B. Lindman, *A record nine different phases (four cubic, two hexagonal, and one lamellar lyotropic liquid crystalline and two micellar solutions) in a ternary isothermal system of an amphiphilic block copolymer and selective solvents (water and oil)*. *Langmuir*, 1998. **14**(10): p. 2627-2638.
132. Black, C.F., et al., *Linear dsDNA Partitions Spontaneously into the Inverse Hexagonal Lyotropic Liquid Crystalline Phases of Phospholipids*. *Journal of American Chemical Society*, 2010. **132**(28): p. 9728-9732.
133. J. Corsi, et al., *Langmuir*, 2010. **26**(14): p. 12119-12125.
134. Marrink, S.J. and A.E. Mark, *Molecular view of hexagonal phase formation in phospholipid membranes*. *Biophys J*, 2004. **87**(6): p. 3894-900.
135. Avogadro, *an open-source molecular builder and visualization tool. Version 1.0.3* <http://avogadro.openmolecules.net/>.
136. Frisch, M.J., et al., *GAUSSIAN 09 (Revision A. 1)*, Gaussian, Inc., Wallingford CT, 2009 *Search PubMed*; (b) S. Grimme. *J. Comput. Chem*, 2006. **27**.
137. Becke, A.D., *Density - functional thermochemistry. III. The role of exact exchange*. *The Journal of chemical physics*, 1993. **98**.
138. Lee, C., W. Yang, and R.G. Parr, *Development of the Colle-Salvetti correlation-energy formula into a functional of the electron density*. *Physical Review B*, 1988. **37**(2).
139. Rassolov, V.A., et al., *6-31G* basis set for atoms K through Zn*. *The Journal of chemical physics*, 1998. **109**(4): p. 1223-1229.
140. Francl, M.M., et al., *Self - consistent molecular orbital methods. XXIII. A polarization - type basis set for second - row elements*. *The Journal of chemical physics*, 1982. **77**(7): p. 3654-3665.

141. Simon, S., M. Duran, and J.J. Dannenberg, *How does basis set superposition error change the potential surfaces for hydrogen - bonded dimers?* The Journal of chemical physics, 1996. **105**.
142. Boys, S.F. and F. Bernardi, *The calculation of small molecular interactions by the differences of separate total energies. Some procedures with reduced errors.* Molecular physics, 1970. **19**(4): p. 553-566.
143. Parr, R.G. and W. Yang, *Density functional approach to the frontier-electron theory of chemical reactivity.* Journal of the American Chemical Society, 1984. **106**(14): p. 4049-4050.
144. Yang, W. and W.J. Mortier, *The use of global and local molecular parameters for the analysis of the gas-phase basicity of amines.* Journal of the American Chemical Society, 1986. **108**(19): p. 5708-5711.
145. Iczkowski, R.P. and J.L. Margrave, *Electronegativity.* Journal of the American Chemical Society, 1961. **83**(17): p. 3547-3551.
146. Geerlings, P., F. De Proft, and W. Langenaeker, *Conceptual density functional theory.* Chemical Reviews-Columbus, 2003. **103**(5): p. 1793-1874.
147. Mulliken, R.S., *A new electroaffinity scale; together with data on valence states and on valence ionization potentials and electron affinities.* The Journal of chemical physics, 1934. **2**.
148. Pearson, R.G., *Absolute electronegativity and hardness: application to inorganic chemistry.* Inorganic Chemistry, 1988. **27**(4): p. 734-740.
149. Atkins, P., *Physical chemistry.* Oxford Univ. Press, Oxford, 1982.
150. Masel, R.I., *Chemical kinetics and catalysis.* 2001: Wiley-Interscience New York.
151. Ballhausen, C.A. and H.B. Gray, *Molecular orbital theory: an introductory lecture note and reprint volume.* 1965.
152. Koopmans, T., *Über die zuordnung von wellenfunktionen und eigenwerten zu den einzelnen elektronen eines atoms.* Physica, 1934. **1**(1-6): p. 104-113.
153. Ayers, P.W., W. Yang, and L.J. Bartolotti, *18 Fukui Function.*
154. Chattaraj, P.K., U. Sarkar, and D.R. Roy, *Electrophilicity index.* Chemical Reviews, 2006. **106**(6): p. 2065-2091.
155. Hanwell, M.D., et al., *Avogadro: an advanced semantic chemical editor, visualization, and analysis platform.* Journal of cheminformatics, 2012. **4**(1): p. 1-17.
156. Halgren, T.A., *Merck molecular force field. I. Basis, form, scope, parameterization, and performance of MMFF94.* Journal of Computational Chemistry, 1996. **17**(5-6): p. 490-519.
157. Oostenbrink, C., et al., *A biomolecular force field based on the free enthalpy of hydration and solvation: The GROMOS force-field parameter sets 53A5 and 53A6.* Journal of Computational Chemistry, 2004. **25**(13): p. 1656-1676.
158. Van Der Spoel, D., et al., *GROMACS: Fast, flexible, and free.* Journal of Computational Chemistry, 2005. **26**(16): p. 1701-1718.
159. Hess, B., et al., *GROMACS 4: Algorithms for Highly Efficient, Load-Balanced, and Scalable Molecular Simulation.* Journal of Chemical Theory and Computation, 2008. **4**(3): p. 435-447.
160. Bandyopadhyay, S., et al., *Molecular dynamics studies of the hexagonal mesophase of sodium dodecylsulphate in aqueous solution.* Molecular Physics, 1998. **95**(2): p. 377-384.
161. Berendsen, H.J.C., et al., *Interaction models for water in relation to protein hydration,* in *Intermolecular Forces*, B. Pullman, Editor. 1981, Reidel: Dordrecht. p. 331.

162. Petrache, H.I., K. Tu, and J.F. Nagle, *Analysis of simulated NMR order parameters for lipid bilayer structure determination*. Biophysical journal, 1999. **76**(5): p. 2479-2487.
163. Shinoda, W., N. Namiki, and S. Okazaki, *Molecular dynamics study of a lipid bilayer: convergence, structure, and long-time dynamics*. Journal of chemical physics, 1997. **106**.
164. Shinoda, W., et al., *Molecular dynamics study on the effect of chain branching on the physical properties of lipid bilayers: structural stability*. the Journal of Physical Chemistry B, 2003. **107**(50): p. 14030-14035.
165. Saupe, A., ZEITSCHRIFT FUR NATURFORSCHUNG SECTION A-A JOURNAL OF PHYSICAL SCIENCES, 1964. **19**: p. 161-71.
166. P. van der Ploeg and H. J. C. Berendsen, J. Chem. Phys., 1982. **76**(3271).
167. Tieleman, D.P. and H.J.C. Berendsen, *Molecular dynamics simulations of a fully hydrated dipalmitoylphosphatidylcholine bilayer with different macroscopic boundary conditions and parameters*. The Journal of chemical physics, 1996. **105**: p. 4871-4871.
168. Turnbull, R.J., E. Neumann, and K. Rosenheck, *An alternate explanation for the permeability changes induced by electrical impulses in vesicular membranes*. Journal of Membrane Biology, 1973. **14**(1): p. 193-196.
169. Speakman, J.C., *The hydrogen bond and other intermolecular forces*. 1975: Chemical Society.
170. Speakman, J.C., *The hydrogen bond and other intermolecular forces*. 1975: Chemical Society.
171. van Buuren, A.R. and H.J.C. Berendsen, *Molecular dynamics simulations of carbohydrate-based surfactants in surfactant/water/oil systems*. Langmuir, 1994. **10**(6): p. 1703-1713.
172. Hill, S.E. and D. Feller, *Theoretical study of cation/ether complexes: 15-crown-5 and its alkali metal complexes*. International Journal of Mass Spectrometry, 2000. **201**(1): p. 41-58.
173. More, M.B., D. Ray, and P. Armentrout, *Intrinsic affinities of alkali cations for 15-crown-5 and 18-crown-6: bond dissociation energies of gas-phase M+-crown ether complexes*. Journal of the American Chemical Society, 1999. **121**(2): p. 417-423.
174. Wang, X., H. Wang, and Y. Tan, *DFT study of the cryptand and benzocryptand and their complexes with alkali metal cations: Li+, Na+, K+*. Journal of Computational Chemistry, 2008. **29**(9): p. 1423-1428.
175. Maleknia, S. and J. Brodbelt, *Gas-phase selectivities of crown ethers for alkali metal ion complexation*. Journal of the American Chemical Society, 1992. **114**(11): p. 4295-4298.
176. Izatt, R., et al., *Calorimetric titration study of the interaction of several uni- and bivalent cations with 15-crown-5, 18-crown-6, and two isomers of dicyclohexo-18-crown-6 in aqueous solution at 25. degree. C and. mu. = 0.1*. Journal of the American Chemical Society, 1976. **98**(24): p. 7620-7626.
177. Izatt, R.M., et al., *Thermodynamic and kinetic data for cation-macrocyclic interaction*. Chemical Reviews, 1985. **85**(4): p. 271-339.
178. Feller, D., *Ab initio study of M+: 18-crown-6 microsolvation*. The Journal of Physical Chemistry A, 1997. **101**(14): p. 2723-2731.
179. Bakó, P., L. Fenichel, and L. Tóke, *The complexing ability of crown ethers incorporating glucose*. Journal of inclusion phenomena and molecular recognition in chemistry, 1993. **16**(1): p. 17-23.
180. Nagle, J.F. and S. Tristram-Nagle, *Lipid bilayer structure*. Current opinion in structural biology, 2000. **10**(4): p. 474-480.

181. Martínez, L., et al., *Packmol: A package for building initial configurations for molecular dynamics simulations*. Journal of computational chemistry, 2009. **30**(13): p. 2157-2164.
182. Sakya, P. and J. Seddon, *Thermotropic and lyotropic phase behaviour of monoalkyl glycosides*. Liquid crystals, 1997. **23**(3): p. 409-424.
183. Nguan, H.S., et al., *Quantitative analysis of the packing of alkyl glycosides: a comparison of linear and branched alkyl chains*. Liquid Crystals, 2010. **37**(9): p. 1205-1213.
184. Nilsson, F., O. Söderman, and I. Johansson, *Physical-chemical properties of the n-octyl β -D-glucoside/water system. A phase diagram, self-diffusion NMR, and SAXS study*. Langmuir, 1996. **12**(4): p. 902-908.
185. Kocherbitov, V., O. Söderman, and L. Wadsö, *Phase diagram and thermodynamics of the n-octyl β -D-glucoside/water system*. The Journal of Physical Chemistry B, 2002. **106**(11): p. 2910-2917.
186. Dorset, D.L., *Anomeric exchange and the structure of n -alkyl d-glucopyranosides. A study of binary phase behavior*. Carbohydrate research, 1990. **206**(2): p. 193-205.
187. Kocherbitov, V. and O. Söderman, *Phase diagram and physicochemical properties of the n-octyl α -D-glucoside/water system*. Physical Chemistry Chemical Physics, 2003. **5**(23): p. 5262-5270.
188. Seddon, J.M. and G. Cevc, *Lipid polymorphism: Structure and stability of lyotropic mesophases of phospholipids*. 1993: Marcel Dekker, Inc: New York, NY, USA.
189. Ericsson, C.A., L.C. Ericsson, and S. Ulvenlund, *Solid-state phase behaviour of dodecylglycosides*. Carbohydrate research, 2005. **340**(8): p. 1529-1537.
190. Jimenez-Barbero, J., et al., *Molecular recognition of carbohydrates using a synthetic receptor. A model system to understand the stereoselectivity of a carbohydrate-carbohydrate interaction in water*. Journal of the American Chemical Society, 1995. **117**(45): p. 11198-11204.
191. Löfgren, H. and I. Pascher, *Molecular arrangements of sphingolipids. The monolayer behaviour of ceramides*. Chemistry and physics of lipids, 1977. **20**(4): p. 273-284.
192. Hashim, R., et al., *A reevaluation of the epimeric and anomeric relationship of glucosides and galactosides in thermotropic liquid crystal self-assemblies*. Carbohydrate research, 2011. **346**(18): p. 2948-2956.
193. Kotena, Z.M., et al., *Hydrogen bonds in galactopyranoside and glucopyranoside: a density functional theory study*. Journal of molecular modeling, 2013. **19**(2): p. 589-599.
194. Mouritsen, O.G. and K. Jørgensen, *Dynamical order and disorder in lipid bilayers*. Chemistry and physics of lipids, 1994. **73**(1): p. 3-25.
195. Marčelja, S., *Chain ordering in liquid crystals: II. Structure of bilayer membranes*. Biochimica et Biophysica Acta (BBA)-Biomembranes, 1974. **367**(2): p. 165-176.
196. Damodaran, K. and K.M. Merz Jr, *A comparison of DMPC-and DLPE-based lipid bilayers*. Biophysical journal, 1994. **66**(4): p. 1076-1087.
197. Seelig, J., *Deuterium magnetic resonance: theory and application to lipid membranes*. Quarterly reviews of biophysics, 1977. **10**(03): p. 353-418.
198. van Buuren, A.R. and H.J. Berendsen, *Molecular dynamics simulations of carbohydrate-based surfactants in surfactant/water/oil systems*. Langmuir, 1994. **10**(6): p. 1703-1713.

199. Muddana, H.S., et al., *Atomistic simulation of lipid and DiI dynamics in membrane bilayers under tension*. Physical Chemistry Chemical Physics, 2011. **13**(4): p. 1368-1378.
200. Jeon, J.-H., et al., *Anomalous diffusion of phospholipids and cholesterol in a lipid bilayer and its origins*. Physical review letters, 2012. **109**(18): p. 188103.
201. Guigas, G. and M. Weiss, *Sampling the cell with anomalous diffusion—the discovery of slowness*. Biophysical journal, 2008. **94**(1): p. 90-94.
202. Lomholt, M.A., I.M. Zaid, and R. Metzler, *Subdiffusion and weak ergodicity breaking in the presence of a reactive boundary*. Physical review letters, 2007. **98**(20): p. 200603.
203. Nicholas J. Brooks, et al., *Thermotropic and lyotropic liquid crystalline phases of Guerbet branched-chain -D-glucosides*. 2011. **38**: p. 1725-1734.
204. Marsh, D., *Pivotal surfaces in inverse hexagonal and cubic phases of phospholipids and glycolipids*. Chemistry and Physics of Lipids, 2011. **164**(3): p. 177-183.
205. Hashim, R., et al., *Nature-like synthetic alkyl branched-chain glycolipids: a review on chemical structure and self-assembly properties*. 2011.
206. GRANICK, S., *Motions and Relaxations of Confined Liquids*. Science, 1991. **253**(5026): p. 1374-1379.
207. Heuberger, M., M. Zäch, and N.D. Spencer, *Density Fluctuations Under Confinement: When Is a Fluid Not a Fluid?* Science, 2001. **292**(5518): p. 905-908.
208. Jensen, M.O., O.G. Mouritsen, and G.H. Peters, *The hydrophobic effect: Molecular dynamics simulations of water confined between extended hydrophobic and hydrophilic surfaces*. The Journal of Chemical Physics, 2004. **120**(20): p. 9729-9744.
209. Pérez-Hernández, N., et al., *The Mobility of Water Molecules through Hydrated Pores*. The Journal of Physical Chemistry C, 2012. **116**(17): p. 9616-9630.
210. Tian, J. and A.E. Garcia, *Simulations of the confinement of ubiquitin in self-assembled reverse micelles*. The Journal of Chemical Physics, 2011. **134**(22): p. 225101-11.
211. Tian, J. and A.E. Garcia, *Simulation Studies of Protein Folding/Unfolding Equilibrium under Polar and Nonpolar Confinement*. Journal of the American Chemical Society, 2011. **133**(38): p. 15157-15164.
212. Hummer, G., J.C. Rasaiah, and J.P. Noworyta, *Water conduction through the hydrophobic channel of a carbon nanotube*. Nature, 2001. **414**(6860): p. 188-190.
213. Zhu, F. and K. Schulten, *Water and Proton Conduction through Carbon Nanotubes as Models for Biological Channels*. Biophysical journal, 2003. **85**(1): p. 236-244.
214. Preston, G.M., et al., *Appearance of Water Channels in Xenopus Oocytes Expressing Red Cell CHIP28 Protein*. Science, 1992. **256**(5055): p. 385-387.
215. Murata, K., et al., *Structural determinants of water permeation through aquaporin-1*. Nature, 2000. **407**(6804): p. 599-605.
216. Tajkhorshid, E., et al., *Control of the Selectivity of the Aquaporin Water Channel Family by Global Orientational Tuning*. Science, 2002. **296**(5567): p. 525-530.
217. Penaloza, D.P., et al., *Spatial heterogeneity in a lyotropic liquid crystal with hexagonal phase*. Physical Chemistry Chemical Physics, 2012. **14**(15): p. 5247-5250.

218. Mark, P. and L. Nilsson, *Structure and dynamics of the TIP3P, SPC, and SPC/E water models at 298 K*. The Journal of Physical Chemistry A, 2001. **105**(43): p. 9954-9960.
219. Chandrasekhar, S., et al., *Columnar, discotic nematic and lamellar liquid crystals: their structures and physical properties*. Handbook of Liquid Crystals Set, 1998: p. 749-780.
220. van der Spoel, D., et al., *Thermodynamics of hydrogen bonding in hydrophilic and hydrophobic media*. The Journal of Physical Chemistry B, 2006. **110**(9): p. 4393-4398.
221. Luzar, A. and D. Chandler, *Hydrogen-bond kinetics in liquid water*. Nature, 1996. **379**(6560): p. 55-57.
222. Jana, B., et al., *Dynamic coupling between the LID and NMP domain motions in the catalytic conversion of ATP and AMP to ADP by adenylate kinase*. The Journal of Chemical Physics, 2011. **134**: p. 035101.
223. Soper, A. and M. Phillips, *A new determination of the structure of water at 25 C*. Chemical physics, 1986. **107**(1): p. 47-60.
224. Turner, D.C. and S.M. Gruner, *X-ray diffraction reconstruction of the inverted hexagonal (HII) phase in lipid-water systems*. Biochemistry, 1992. **31**(5): p. 1340-1355.
225. Perutkova, S., et al., *Elastic deformations in hexagonal phases studied by small-angle X-ray diffraction and simulations*. Physical Chemistry Chemical Physics, 2011. **13**(8): p. 3100-3107.
226. Hamm, M. and M.M. Kozlov, *Tilt model of inverted amphiphilic mesophases*. The European Physical Journal B - Condensed Matter and Complex Systems, 1998. **6**(4): p. 519-528.

APPENDICES

Appendix A.1

Prepin file for n-octyl- α -D-galactoside

This is a remark line

molecule.res

Gal INT 0

CORRECT OMIT DU BEG

0.0000

1	DUMM	DU	M	0	-1	-2	0.000	.0	.0	.00000
2	DUMM	DU	M	1	0	-1	1.449	.0	.0	.00000
3	DUMM	DU	M	2	1	0	1.522	111.1	.0	.00000
4	C31	CG	M	3	2	1	1.540	111.208	180.000	0.00000
5	H46	HC	E	4	3	2	1.089	35.485	1.903	0.00000
6	H47	HC	E	4	3	2	1.090	145.001	1.650	0.00000
7	H48	HC	E	4	3	2	1.090	89.947	127.059	0.00000
8	C30	CG	M	4	3	2	1.559	89.816	-123.486	0.00000
9	H44	HC	E	8	4	3	1.090	102.499	-157.743	0.00000
10	H45	HC	E	8	4	3	1.091	109.493	-36.865	0.00000
11	C29	CG	M	8	4	3	1.458	119.158	90.103	0.00000
12	H42	HC	E	11	8	4	1.090	105.354	-64.264	0.00000
13	H43	HC	E	11	8	4	1.090	109.432	56.092	0.00000
14	C28	CG	M	11	8	4	1.258	115.364	-179.958	0.00000
15	H40	HC	E	14	11	8	1.090	111.112	-58.572	0.00000
16	H41	HC	E	14	11	8	1.090	109.474	61.468	0.00000
17	C27	CG	M	14	11	8	1.431	106.963	-179.997	0.00000
18	H38	HC	E	17	14	11	1.090	112.882	-57.154	0.00000
19	H39	HC	E	17	14	11	1.090	109.462	63.012	0.00000
20	C26	CG	M	17	14	11	1.439	104.147	179.965	0.00000
21	H36	HC	E	20	17	14	1.090	115.521	-55.421	0.00000
22	H37	HC	E	20	17	14	1.090	109.421	65.199	0.00000
23	C25	CG	M	20	17	14	1.559	99.872	-179.982	0.00000
24	H34	HC	E	23	20	17	1.090	112.890	-57.144	0.00000
25	H35	HC	E	23	20	17	1.089	109.454	63.081	0.00000
26	C24	CG	M	23	20	17	1.524	104.046	-179.964	0.00000
27	H32	H1	E	26	23	20	1.090	112.808	-59.437	0.00000
28	H33	H1	E	26	23	20	1.090	109.474	60.747	0.00000
29	O7	OS	M	26	23	20	1.213	104.229	177.781	-0.19400
30	C2	CG	M	29	26	23	1.398	115.772	-168.336	0.46500
31	H10	H2	E	30	29	26	1.117	115.448	44.992	0.00000
32	O1	OS	M	30	29	26	1.392	105.704	158.586	-0.52700
33	C3	CG	M	32	30	29	1.404	116.165	62.187	0.21600
34	C14	CG	3	33	32	30	1.535	104.188	178.248	0.30800
35	H20	H1	E	34	33	32	1.108	111.719	-50.234	0.00000
36	O21	OH	S	34	33	32	1.387	110.896	75.550	-0.68400
37	H23	HO	E	36	34	33	0.966	108.280	-62.744	0.41800
38	H22	H1	E	34	33	32	1.104	110.764	-168.835	0.00000
39	H19	H1	E	33	32	30	1.117	111.107	-64.033	0.00000
40	C4	CG	M	33	32	30	1.531	111.355	57.467	0.20400
41	O13	OH	S	40	33	32	1.393	112.027	60.573	-0.67300
42	H15	HO	E	41	40	33	0.963	108.032	76.051	0.43600
43	H16	H1	E	40	33	32	1.118	109.393	-175.335	0.00000
44	C6	CG	M	40	33	32	1.536	108.901	-55.752	0.25300
45	O12	OH	S	44	40	33	1.386	112.075	179.767	-0.70100
46	H17	HO	E	45	44	40	0.967	109.623	-57.996	0.43300
47	H18	H1	E	44	40	33	1.117	110.115	-65.845	0.00000
48	C5	CG	M	44	40	33	1.533	109.147	56.037	0.33900
49	H8	H1	E	48	44	40	1.117	110.597	65.122	0.00000
50	O9	OH	M	48	44	40	1.390	112.228	-171.196	-0.72400
51	H11	HO	E	50	48	44	0.966	108.230	-48.504	0.43100

Appendix A.2

Prepin file for n-octyl- α -D-glycoside

This is a remark line

molecule.res

Glc INT 0

CORRECT OMIT DU BEG

0.0000

1	DUMM	DU	M	0	-1	-2	0.000	.0	.0	.00000
2	DUMM	DU	M	1	0	-1	1.449	.0	.0	.00000
3	DUMM	DU	M	2	1	0	1.522	111.1	.0	.00000
4	C30	CG	M	3	2	1	1.540	111.208	180.000	0.00000
5	H46	HC	E	4	3	2	1.090	39.755	-3.207	0.00000
6	H47	HC	E	4	3	2	1.089	126.912	69.213	0.00000
7	H48	HC	E	4	3	2	1.081	69.867	168.690	0.00000
8	C29	CG	M	4	3	2	1.536	120.094	-88.232	0.00000
9	H44	HC	E	8	4	3	1.086	110.300	-137.143	0.00000
10	H45	HC	E	8	4	3	1.087	110.385	-19.092	0.00000
11	C28	CG	M	8	4	3	1.528	110.956	101.911	0.00000
12	H42	HC	E	11	8	4	1.088	110.472	-59.056	0.00000
13	H43	HC	E	11	8	4	1.087	110.356	58.908	0.00000
14	C27	CG	M	11	8	4	1.525	110.723	179.879	0.00000
15	H40	HC	E	14	11	8	1.088	110.193	-57.562	0.00000
16	H41	HC	E	14	11	8	1.089	110.217	60.091	0.00000
17	C26	CG	M	14	11	8	1.524	110.919	-178.697	0.00000
18	H38	HC	E	17	14	11	1.088	110.263	-58.587	0.00000
19	H39	HC	E	17	14	11	1.090	109.955	59.036	0.00000
20	C25	CG	M	17	14	11	1.522	110.358	-179.914	0.00000
21	H36	HC	E	20	17	14	1.088	109.917	-56.094	0.00000
22	H37	HC	E	20	17	14	1.088	109.923	61.546	0.00000
23	C24	CG	M	20	17	14	1.522	110.814	-177.054	0.00000
24	H34	HC	E	23	20	17	1.087	110.528	-58.365	0.00000
25	H35	HC	E	23	20	17	1.087	110.238	59.758	0.00000
26	C23	CG	M	23	20	17	1.533	110.164	-179.663	0.00000
27	H32	H1	E	26	23	20	1.099	110.180	-52.977	0.00000
28	H33	H1	E	26	23	20	1.098	109.572	64.547	0.00000
29	O7	OS	M	26	23	20	1.421	104.698	-173.819	-0.19400
30	C2	CG	M	29	26	23	1.420	113.999	-154.614	0.50900
31	H22	H2	E	30	29	26	1.098	113.486	30.342	0.00000
32	O1	OS	M	30	29	26	1.427	106.730	146.462	-0.57400
33	C3	CG	M	32	30	29	1.438	111.887	59.124	0.28300
34	H8	H1	E	33	32	30	1.098	113.184	-62.358	0.00000
35	C9	CG	3	33	32	30	1.557	102.500	178.694	0.27600
36	O16	OH	S	35	33	32	1.427	112.332	-53.737	-0.68200
37	H19	HO	E	36	35	33	0.991	105.270	-42.870	0.41800
38	H20	H1	E	35	33	32	1.095	108.640	-179.565	0.00000
39	H21	H1	E	35	33	32	1.092	107.435	63.386	0.00000
40	C4	CG	M	33	32	30	1.567	111.527	58.385	0.25400
41	O10	OH	S	40	33	32	1.437	112.505	-174.104	-0.71000
42	H18	HO	E	41	40	33	0.985	105.281	-70.031	0.43600
43	H11	H1	E	40	33	32	1.089	108.450	62.603	0.00000
44	C6	CG	M	40	33	32	1.548	110.958	-55.037	0.28600
45	O14	OH	S	44	40	33	1.430	111.833	171.095	-0.69900
46	H17	HO	E	45	44	40	0.985	104.006	64.969	0.42700
47	H15	H1	E	44	40	33	1.089	107.081	-65.731	0.00000
48	C5	CG	M	44	40	33	1.545	109.173	52.842	0.24600
49	H12	H1	E	48	44	40	1.094	107.492	64.574	0.00000
50	O13	OH	M	48	44	40	1.435	111.904	-172.249	-0.71300
51	H31	HO	E	50	48	44	0.988	103.430	-58.120	0.43700

0 0 2

Appendix A.3

Prepin file for n-octyl- β -D-glycoside

This is a remark line

molecule.res

Gal INT 0

CORRECT OMIT DU BEG

0.0000

1	DUMM	DU	M	0	-1	-2	0.000	.0	.0	.00000
2	DUMM	DU	M	1	0	-1	1.449	.0	.0	.00000
3	DUMM	DU	M	2	1	0	1.522	111.1	.0	.00000
4	O13	OH	M	3	2	1	1.540	111.208	180.000	-0.72600
5	H23	HO	E	4	3	2	0.943	128.989	93.757	0.43200
6	C5	CG	M	4	3	2	1.404	58.575	-179.570	0.35700
7	H14	H1	E	6	4	3	1.115	107.200	-178.640	0.00000
8	C4	CG	M	6	4	3	1.530	109.138	60.547	0.25900
9	H11	H1	E	8	6	4	1.117	110.901	-52.091	0.00000
10	O12	OH	S	8	6	4	1.405	110.054	65.739	-0.69400
11	H19	HO	E	10	8	6	0.942	106.371	-63.428	0.43300
12	C3	CG	M	8	6	4	1.533	109.401	-173.799	0.20300
13	H9	H1	E	12	8	6	1.116	111.148	176.351	0.00000
14	O10	OH	S	12	8	6	1.404	108.589	-66.690	-0.66400
15	H18	HO	E	14	12	8	0.943	106.951	-59.849	0.43700
16	C2	CG	M	12	8	6	1.537	110.159	53.127	0.14000
17	H7	H1	E	16	12	8	1.117	109.449	62.622	0.00000
18	C8	CG	3	16	12	8	1.534	114.052	-177.643	0.31900
19	H16	H1	E	18	16	12	1.114	111.575	-179.125	0.00000
20	H17	H1	E	18	16	12	1.114	111.266	-56.604	0.00000
21	O20	OH	S	18	16	12	1.402	110.446	62.372	-0.69300
22	H21	HO	E	21	18	16	0.942	107.634	-172.573	0.41900
23	O1	OS	M	16	12	8	1.414	110.178	-55.189	-0.40200
24	C6	CG	M	23	16	12	1.409	112.541	61.602	0.37400
25	H15	H2	E	24	23	16	1.117	111.020	60.502	0.00000
26	O22	OS	M	24	23	16	1.410	103.034	178.304	-0.19400
27	C24	CG	M	26	24	23	1.413	113.044	-67.771	0.00000
28	H32	H1	E	27	26	24	1.115	109.397	-53.419	0.00000
29	H33	H1	E	27	26	24	1.115	108.405	66.952	0.00000
30	C25	CG	M	27	26	24	1.534	109.146	-173.373	0.00000
31	H34	HC	E	30	27	26	1.116	109.868	-55.326	0.00000
32	H35	HC	E	30	27	26	1.116	109.653	62.725	0.00000
33	C26	CG	M	30	27	26	1.538	110.020	-176.257	0.00000
34	H36	HC	E	33	30	27	1.117	109.275	-58.299	0.00000
35	H37	HC	E	33	30	27	1.116	109.166	58.812	0.00000
36	C27	CG	M	33	30	27	1.535	112.601	-179.831	0.00000
37	H38	HC	E	36	33	30	1.116	109.387	-58.186	0.00000
38	H39	HC	E	36	33	30	1.116	109.468	59.412	0.00000
39	C28	CG	M	36	33	30	1.537	111.239	-179.275	0.00000
40	H40	HC	E	39	36	33	1.116	109.414	-58.793	0.00000
41	H41	HC	E	39	36	33	1.116	109.479	58.508	0.00000
42	C29	CG	M	39	36	33	1.536	111.752	179.816	0.00000
43	H42	HC	E	42	39	36	1.115	109.327	-58.656	0.00000
44	H43	HC	E	42	39	36	1.116	109.301	58.726	0.00000
45	C30	CG	M	42	39	36	1.537	111.917	-179.995	0.00000
46	H44	HC	E	45	42	39	1.116	109.640	-58.743	0.00000
47	H45	HC	E	45	42	39	1.116	109.649	58.833	0.00000
48	C31	CG	M	45	42	39	1.534	111.470	-179.974	0.00000
49	H46	HC	E	48	45	42	1.115	111.068	179.968	0.00000
50	H47	HC	E	48	45	42	1.114	111.066	-60.052	0.00000
51	H48	HC	E	48	45	42	1.114	111.066	60.110	0.00000

Appendix A.4

Prepin file for n-octyl- β -D-galactoside

0 0 2

This is a remark line

molecule.res

Gal INT 0

CORRECT OMIT DU BEG

0.0000

1	DUMM	DU	M	0	-1	-2	0.000	.0	.0	.00000
2	DUMM	DU	M	1	0	-1	1.449	.0	.0	.00000
3	DUMM	DU	M	2	1	0	1.522	111.1	.0	.00000
4	O6	OH	M	3	2	1	1.540	111.208	180.000	-0.68800
5	H16	HO	E	4	3	2	0.980	70.570	155.654	0.42400
6	C6	CG	M	4	3	2	1.432	81.728	-95.670	0.28200
7	H6	H1	E	6	4	3	1.090	109.287	-126.380	0.00000
8	H7	H1	E	6	4	3	1.091	108.904	-7.665	0.00000
9	C5	CG	M	6	4	3	1.535	111.055	112.409	0.22500
10	H5	H1	E	9	6	4	1.092	107.901	179.790	0.00000
11	O5	OS	E	9	6	4	1.442	108.280	-61.942	-0.47100
12	C4	CG	M	9	6	4	1.541	111.780	59.774	0.27600
13	H4	H1	E	12	9	6	1.091	109.398	-58.297	0.00000
14	O4	OH	S	12	9	6	1.434	109.378	61.214	-0.71400
15	H14	HO	E	14	12	9	0.980	105.444	-174.215	0.44000
16	C3	CG	M	12	9	6	1.538	109.640	-177.826	0.28400
17	H3	H1	E	16	12	9	1.091	108.932	-67.420	0.00000
18	O3	OH	S	16	12	9	1.435	109.427	173.654	-0.70900
19	H13	HO	E	18	16	12	0.981	105.371	172.804	0.43200
20	C2	CG	M	16	12	9	1.539	110.503	52.429	0.31000
21	H2	H1	E	20	16	12	1.091	109.219	66.605	0.00000
22	O2	OH	S	20	16	12	1.435	109.451	-173.904	-0.71800
23	H12	HO	E	22	20	16	0.980	105.480	-172.964	0.43700
24	C1	CG	M	20	16	12	1.538	109.510	-52.985	0.38400
25	H1	H2	E	24	20	16	1.092	108.787	-62.371	0.00000
26	O1	OS	M	24	20	16	1.439	109.544	177.925	-0.19400
27	C21	CG	M	26	24	20	1.437	108.871	167.268	0.00000
28	H29	H1	E	27	26	24	1.091	110.393	61.516	0.00000
29	H30	H1	E	27	26	24	1.090	109.780	-59.213	0.00000
30	C22	CG	M	27	26	24	1.542	109.326	-178.702	0.00000
31	H31	HC	E	30	27	26	1.091	109.411	57.296	0.00000
32	H32	HC	E	30	27	26	1.091	109.399	-62.542	0.00000
33	C23	CG	M	30	27	26	1.543	109.595	177.259	0.00000
34	H33	HC	E	33	30	27	1.090	109.291	58.827	0.00000
35	H34	HC	E	33	30	27	1.090	109.320	-60.724	0.00000
36	C24	CG	M	33	30	27	1.542	110.344	179.001	0.00000
37	H35	HC	E	36	33	30	1.090	109.589	59.840	0.00000
38	H36	HC	E	36	33	30	1.091	109.308	-60.046	0.00000
39	C25	CG	M	36	33	30	1.544	109.719	179.977	0.00000
40	H37	HC	E	39	36	33	1.090	109.296	57.559	0.00000
41	H38	HC	E	39	36	33	1.090	109.282	-61.986	0.00000
42	C26	CG	M	39	36	33	1.543	110.234	177.684	0.00000
43	H39	HC	E	42	39	36	1.091	109.413	61.049	0.00000
44	H40	HC	E	42	39	36	1.090	109.389	-58.783	0.00000
45	C27	CG	M	42	39	36	1.543	109.746	-178.803	0.00000
46	H41	HC	E	45	42	39	1.090	109.486	60.056	0.00000
47	H42	HC	E	45	42	39	1.090	109.497	-59.720	0.00000
48	C28	CG	M	45	42	39	1.542	110.216	-179.881	0.00000
49	H43	HC	E	48	45	42	1.090	109.712	60.711	0.00000
50	H44	HC	E	48	45	42	1.090	109.631	-59.489	0.00000
51	H45	HC	E	48	45	42	1.091	109.361	-179.317	0.00000

Appendix B

Sample coordinate file for Prepin file for n-octyl- β -D-galactoside

```
REMARK
ATOM 1 O1 Gal 1 42.718 31.826 -22.071
ATOM 2 C2 Gal 1 43.267 30.868 -21.183
ATOM 3 C3 Gal 1 43.550 32.900 -22.324
ATOM 4 C4 Gal 1 44.921 32.455 -22.898
ATOM 5 C5 Gal 1 44.572 30.282 -21.769
ATOM 6 C6 Gal 1 45.510 31.429 -21.946
ATOM 7 O7 Gal 1 43.419 31.568 -19.929
ATOM 8 H8 Gal 1 44.366 29.834 -22.746
ATOM 9 O9 Gal 1 45.147 29.323 -20.869
ATOM 10 H10 Gal 1 42.562 30.026 -21.076
ATOM 11 H11 Gal 1 45.817 28.770 -21.334
ATOM 12 O12 Gal 1 46.732 30.940 -22.397
ATOM 13 O13 Gal 1 44.814 31.908 -24.248
ATOM 14 C14 Gal 1 42.860 33.812 -23.355
ATOM 15 H15 Gal 1 44.304 32.484 -24.764
ATOM 16 H16 Gal 1 45.595 33.307 -22.932
ATOM 17 H17 Gal 1 46.612 30.689 -23.288
ATOM 18 H18 Gal 1 45.729 31.914 -21.014
ATOM 19 H19 Gal 1 43.732 33.482 -21.402
ATOM 20 H20 Gal 1 42.531 33.179 -24.167
ATOM 21 O21 Gal 1 41.736 34.490 -22.786
ATOM 22 H22 Gal 1 43.569 34.501 -23.812
ATOM 23 H23 Gal 1 41.029 33.903 -22.792
ATOM 24 C24 Gal 1 43.277 30.704 -18.853
ATOM 25 C25 Gal 1 43.526 31.540 -17.587
ATOM 26 C26 Gal 1 43.449 30.583 -16.324
ATOM 27 C27 Gal 1 43.675 31.415 -15.037
ATOM 28 C28 Gal 1 43.383 30.519 -13.773
ATOM 29 C29 Gal 1 43.518 31.377 -12.441
ATOM 30 C30 Gal 1 43.013 30.557 -11.241
ATOM 31 C31 Gal 1 43.017 31.417 -9.967
ATOM 32 H32 Gal 1 44.083 29.984 -18.995
ATOM 33 H33 Gal 1 42.334 30.224 -18.936
ATOM 34 H34 Gal 1 42.843 32.380 -17.516
ATOM 35 H35 Gal 1 44.555 31.923 -17.674
ATOM 36 H36 Gal 1 44.247 29.842 -16.340
ATOM 37 H37 Gal 1 42.462 30.101 -16.266
ATOM 38 H38 Gal 1 43.014 32.280 -15.125
ATOM 39 H39 Gal 1 44.685 31.829 -15.007
ATOM 40 H40 Gal 1 44.005 29.626 -13.785
ATOM 41 H41 Gal 1 42.336 30.150 -13.817
ATOM 42 H42 Gal 1 42.915 32.274 -12.505
ATOM 43 H43 Gal 1 44.564 31.664 -12.258
ATOM 44 H44 Gal 1 43.611 29.679 -11.129
ATOM 45 H45 Gal 1 41.965 30.292 -11.513
ATOM 46 H46 Gal 1 42.287 32.148 -9.982
ATOM 47 H47 Gal 1 43.940 31.961 -9.863
ATOM 48 H48 Gal 1 42.771 30.806 -9.169
TER
```



```

%FORMAT (5E16.8)
  1.80000000E-01  1.70000000E-01  5.00000000E-02 -1.00000000E-01  9.50000000E-01
  5.50000000E-01  1.50000000E-01  1.00000000E-01  4.50000000E-01  1.60000000E-01
 -2.70000000E-01 -1.10000000E+00  2.50000000E-01  6.00000000E-01  2.70000000E-01
  1.08000000E+00  1.38000000E+00  9.60000000E-01  1.30000000E-01
%FLAG DIHEDRAL_PERIODICITY
%FORMAT (5E16.8)
  3.00000000E+00  3.00000000E+00  3.00000000E+00  1.00000000E+00  2.00000000E+00
  3.00000000E+00  3.00000000E+00  3.00000000E+00  1.00000000E+00  3.00000000E+00
  1.00000000E+00  1.00000000E+00  2.00000000E+00  2.00000000E+00  3.00000000E+00
  1.00000000E+00  2.00000000E+00  3.00000000E+00  3.00000000E+00
%FLAG DIHEDRAL_PHASE
%FORMAT (5E16.8)
  0.00000000E+00  0.00000000E+00  0.00000000E+00  0.00000000E+00  0.00000000E+00
  0.00000000E+00  0.00000000E+00  0.00000000E+00  0.00000000E+00  0.00000000E+00
  0.00000000E+00  0.00000000E+00  0.00000000E+00  0.00000000E+00  0.00000000E+00
  0.00000000E+00  0.00000000E+00  0.00000000E+00  0.00000000E+00
%FLAG SOLTY
%FORMAT (5E16.8)
  0.00000000E+00  0.00000000E+00  0.00000000E+00  0.00000000E+00  0.00000000E+00
  0.00000000E+00  0.00000000E+00
%FLAG LENNARD_JONES_ACOEF
%FORMAT (5E16.8)
  1.04308023E+06  9.71708117E+04  7.51607703E+03  6.78771368E+04  4.98586848E+03
  3.25969625E+03  6.28541240E+05  5.33379252E+04  3.63097246E+04  3.61397723E+05
  4.68930885E+04  3.25969625E+03  2.09814978E+04  2.44050579E+04  1.32801250E+03
  7.91544157E+05  6.82786631E+04  4.66922514E+04  4.58874091E+05  3.15360051E+04
  5.81803229E+05  0.00000000E+00  0.00000000E+00  0.00000000E+00  0.00000000E+00
  0.00000000E+00  0.00000000E+00  0.00000000E+00
%FLAG LENNARD_JONES_BCOEF
%FORMAT (5E16.8)
  6.75612247E+02  1.26919150E+02  2.17257828E+01  1.06076943E+02  1.76949863E+01
  1.43076527E+01  5.85549272E+02  1.04986921E+02  8.66220817E+01  4.95732238E+02
  8.81685417E+01  1.43076527E+01  1.14788417E+01  7.10161395E+01  9.13231543E+00
  6.93079947E+02  1.25287818E+02  1.03606917E+02  5.89183300E+02  8.51470647E+01
  6.99746810E+02  0.00000000E+00  0.00000000E+00  0.00000000E+00  0.00000000E+00
  0.00000000E+00  0.00000000E+00  0.00000000E+00
%FLAG BONDS_INC_HYDROGEN
%FORMAT (10I8)
  138 141 1 132 135 2 123 126 1 120
  129 2 111 114 1 108 117 2 96 99
  1 90 93 2 90 102 2 87 105 2
  78 81 6 66 69 2 66 72 2 57
  60 7 57 63 7 48 51 7 48 54
  7 39 42 7 39 45 7 30 33 7
  30 36 7 21 24 7 21 27 7 12
  15 7 12 18 7 0 3 7 0 6
  7 0 9 7 282 285 1 276 279 2
  267 270 1 264 273 2 255 258 1 252
  261 2 240 243 1 234 237 2 234 246
  2 231 249 2 222 225 6 210 213 2
  210 216 2 201 204 7 201 207 7 192
  195 7 192 198 7 183 186 7 183 189
  2055 2061 7 2046 2049 7 2046 2052 7 2037
  2040 7 2037 2043 7 2028 2031 7 2028 2034
  7 2016 2019 7 2016 2022 7 2016 2025 7
  2298 2301 1 2292 2295 2 2283 2286 1 2280
  2289 2 2271 2274 1 2268 2277 2 2256 2259
  1 2250 2253 2 2250 2262 2 2247 2265 2
  2238 2241 6 2226 2229 2 2226 2232 2 2217
  2220 7 2217 2223 7 2208 2211 7 2208 2214
.
.
.
%FLAG DIHEDRAL_FORCE_CONSTANT
%FORMAT (5E16.8)
  1.80000000E-01  1.70000000E-01  5.00000000E-02 -1.00000000E-01  9.50000000E-01
  5.50000000E-01  1.50000000E-01  1.00000000E-01  4.50000000E-01  1.60000000E-01
 -2.70000000E-01 -1.10000000E+00  2.50000000E-01  6.00000000E-01  2.70000000E-01
  1.08000000E+00  1.38000000E+00  9.60000000E-01  1.30000000E-01
%FLAG DIHEDRAL_PERIODICITY
%FORMAT (5E16.8)
  3.00000000E+00  3.00000000E+00  3.00000000E+00  1.00000000E+00  2.00000000E+00
  3.00000000E+00  3.00000000E+00  3.00000000E+00  1.00000000E+00  3.00000000E+00
  1.00000000E+00  1.00000000E+00  2.00000000E+00  2.00000000E+00  3.00000000E+00
  1.00000000E+00  2.00000000E+00  3.00000000E+00  3.00000000E+00
%FLAG DIHEDRAL_PHASE
%FORMAT (5E16.8)
  0.00000000E+00  0.00000000E+00  0.00000000E+00  0.00000000E+00  0.00000000E+00

```

```

0.00000000E+00 0.00000000E+00 0.00000000E+00 0.00000000E+00 0.00000000E+00
0.00000000E+00 0.00000000E+00 0.00000000E+00 0.00000000E+00 0.00000000E+00
0.00000000E+00 0.00000000E+00 0.00000000E+00 0.00000000E+00
%FLAG SOLTY
%FORMAT(5E16.8)
0.00000000E+00 0.00000000E+00 0.00000000E+00 0.00000000E+00 0.00000000E+00
0.00000000E+00 0.00000000E+00
%FLAG LENNARD_JONES_ACOEF
%FORMAT(5E16.8)
1.04308023E+06 9.71708117E+04 7.51607703E+03 6.78771368E+04 4.98586848E+03
3.25969625E+03 6.28541240E+05 5.33379252E+04 3.63097246E+04 3.61397723E+05
4.68930885E+04 3.25969625E+03 2.09814978E+03 2.44050579E+04 1.32801250E+03
7.91544157E+05 6.82786631E+04 4.66922514E+04 4.58874091E+05 3.15360051E+04
5.81803229E+05 0.00000000E+00 0.00000000E+00 0.00000000E+00 0.00000000E+00
0.00000000E+00 0.00000000E+00 0.00000000E+00
%FLAG LENNARD_JONES_BCOEF
%FORMAT(5E16.8)
6.75612247E+02 1.26919150E+02 2.17257828E+01 1.06076943E+02 1.76949863E+01
1.43076527E+01 5.85549272E+02 1.04986921E+02 8.66220817E+01 4.95732238E+02
8.81685417E+01 1.43076527E+01 1.14788417E+01 7.10161395E+01 9.13231543E+00
6.93079947E+02 1.25287818E+02 1.03606917E+02 5.89183300E+02 8.51470647E+01
6.99746810E+02 0.00000000E+00 0.00000000E+00 0.00000000E+00 0.00000000E+00
0.00000000E+00 0.00000000E+00 0.00000000E+00
%FLAG BONDS_INC_HYDROGEN
%FORMAT(10I8)
138 141 1 132 135 2 123 126 1 120
129 2 111 114 1 108 117 2 96 99
1 90 93 2 90 102 2 87 105 2
78 81 6 66 69 2 66 72 2 57
60 7 57 63 7 48 51 7 48 54
7 39 42 7 39 45 7 30 33 7
30 36 7 21 24 7 21 27 7 12
15 7 12 18 7 0 3 7 0 6
7 0 9 7 282 285 1 276 279 2
267 270 1 264 273 2 255 258 1 252
261 2 240 243 1 234 237 2 234 246
2 231 249 2 222 225 6 210 213 2
210 216 2 201 204 7 201 207 7 192
195 7 192 198 7 183 186 7 183 189
7 174 177 7 174 180 7 165 168 7
165 171 7 156 159 7 156 162 7 144
.
.
%FLAG HBOND_ACOEF
%FORMAT(5E16.8)
%FLAG HBOND_BCOEF
%FORMAT(5E16.8)
%FLAG HBCUT
%FORMAT(5E16.8)
%FLAG AMBER_ATOM_TYPE
%FORMAT(20a4)
CG HC HC HC CG HC HC CG
HC HC CG H1 H1 OS CG H2 OS CG CG H1 OH HO H1 H1 CG OH HO H1
CG OH HO H1 CG H1 OH HO CG HC HC HC CG HC HC CG HC HC CG HC
HC CG HC HC CG HC HC CG HC HC CG H1 H1 OS CG H2 OS CG CG H1
OH HO H1 H1 CG OH HO H1 CG OH HO H1 CG H1 OH HO CG HC HC HC
CG HC HC CG HC HC CG HC HC CG HC HC CG HC HC CG HC HC CG H1
H1 OS CG H2 OS CG CG H1 OH HO H1 H1 CG OH HO H1 CG H1 OH HO
CG HC HC CG H1
H1 OS CG H2 OS CG CG H1 OH HO H1 H1 CG OH HO H1 CG OH HO H1
CG HC HC CG HC HC CG H1 H1 OS CG H2 OS CG CG H1 OH HO H1 H1
.
.
%FLAG TREE_CHAIN_CLASSIFICATION
%FORMAT(20a4)
M E E E M E E M E E M E E M E E M E E M
E E M E E M M E S 3 3 E S E E E 3 S E E
B S E E M E M E M E E M E E M E E M E
E M E E M E E M E E M E E M M E S 3 3 E
S E E E 3 S E E B S E E M E M E E E

```


LIST OF SCIENTIFIC CONTRIBUTIONS

Publications

Academic Journal

1. Sara Ahmadi, Vijayan Manickam Achari, Hock Seng Nguan and Rauzah Hashim, Atomistic Simulation Studies of the α/β -Glucoside and Galactoside in Anhydrous Bilayers: Effect of the Anomeric and Epimeric Configurations, Journal of molecular modeling, 2014 (in press.).
2. Nguan, H., S. Ahmadi, and Hashim DFT study of glucose based glycolipid crown ethers and their complexes with alkali metal cations Na⁺ and K⁺. Journal of molecular modeling, 2012. 18(12): p. 5041-5050.
3. Nguan, H., S. Ahmadi, and Hashim Molecular Dynamics Simulation of the Lyotropic Reverse Hexagonal (H_{II}) of Guerbet Branched-Chain β -D-Glucoside, Journal of Physical Chemistry Chemical Physics, Phys. Chem. Chem. Phys., 2014, 16, 324-.334

Extended Abstract

1. Sara Ahmadi, Nguan Hock Seng, Thorsten Heidelberg and Rauzah Hashim. Modelling and Molecular Dynamics on a Hexagonal Glycolipid Assembly. 6th Mathematics and Physical Sciences Graduate Congress 2010, 13th- 15th December 2010, Faculty of science, University of Malaya, Malaysia.

Presentations

Oral

1. Sara Ahmadi, Hock Seng Nguan and Rauzah Hashim, Computer Simulation of Glycolipids in Hexagonal Phase. Fundamental Science Congress (FSC2012), 17th-18th July 2012, University Putra Malaya, Kuala Lumpur, Malaysia.

